IPP-Report

Max-Planck-Institut für Plasmaphysik

Hauke Hölbe

Control of the magnetic topology and plasma exhaust in the edge region of Wendelstein 7-X: A numerical study

IPP 18/4
Februar, 2016

Control of the magnetic topology and plasma exhaust in the edge region of Wendelstein 7-X: A numerical study

Inauguraldissertation

zur

Erlangung des akademischen Grades eines

Doktors der Naturwissenschaften (Dr. rer. nat.)

der

Mathematisch-Naturwissenschaftlichen Fakultät

der

Ernst-Moritz-Arndt-Universität Greifswald

vorgelegt von
Hauke Hölbe
geboren am 16.04.1982
in Bremen

Greifswald, den 28.08.2015

Dekan:	Prof. Dr. Klaus Fesser
1. Gutachter:	Prof. Dr. Thomas Sunn Pedersen
2. Gutachter:	Prof. Dr. Volker Naulin
Datum der Promotion:	07.12.2015

Kurzfassung

Nukleare Fusion ist die Energiequelle der Sterne. Sie hat das Potential die Energiequelle der Zukunft für die Menschheit zu werden. Die Erforschung der Fusionsenergie richtet sich in erster Linie auf die Erforschung des magnetischen Einschlusses des Plasmas. Dabei wird heißes Plasma, das Temperaturen um 100 Millionen Grad Celsius erreicht, in einem speziell dafür entworfenen ringförmigen magnetischen Käfig eingeschlossen.

Führend im Bereich des magnetischen Einschlusses sind dabei das Tokamak- und das Stellaratorkonzept. Die Entwicklung des Tokamaks ist bereits weiter fortgeschritten, jedoch bietet das Stellaratorkonzept einige inhärente und sehr wichtige Vorteile, weshalb es ebenfalls aktiv erforscht wird.

Der Wendelstein 7-X (W7-X) Stellarator entwickelt sich zum weltweit führenden Stellaratorexperiment. Er wird demnächst in Greifswald, Deutschland in Betrieb genommen. Die vorliegende Dissertation befasst sich mit einigen wissenschaftlich wichtigen Herausforderungen, des Stellaratorkonzeptes insgesamt und mit Herausforderungen die W7-X im Besonderen bereithält. Um genauer zu sein, wie die Plasma-Wand-Interaktion abläuft, besonders auch, wie Wärme- und Teilchenströme kontrolliert werden können.

Um Wärme und Teilchen abzuführen, bedient sich W7-X des Konzepts des „Insel-Divertors“. Obwohl dieses Konzept bereits in den 1950ern von Lyman Spitzer erfunden wurde [1], muss der Stellarator-Insel-Divertor noch experimentell erforscht werden für die Eignung für fusionsrelevanten Wärmelasten und Temperaturen, die im Dauerbetrieb erreicht werden. W7-X ist das erste Experiment, das dies ermöglicht. Um das erforderliche Aussehen der Divertorkomponenten festzulegen, wurden einige theoretische und numerische Studien durchgeführt. Die tatsächlichen Divertorkomponenten befinden sich bereits in Serienproduktion und sind sehr gut kompatibel mit den erwarteten Wärmelasten. Mit Hilfe der sehr ausgereiften Codes, welche mittlerweile verfügbar sind, hat sich herausgestellt, dass einige Betriebsszenarien, die ansonsten durchaus interessant wären, zu einer Überladung der Divertoren von W7-X führen würden. Bisher wurde mindestens eine Strategie zur Abschwächung der Wärmelasten vorgeschlagen, aber diese wurde noch nicht in ausreichendem Maße analysiert. In dieser Dissertation werden aktuelle Computer-Codes verwendet um diese Strategie zu analysieren und um weitere Lösungsmöglichkeiten zu entwickeln, welche vorteilhaft sein könnten.

Die vorliegende Arbeit zeigt diese Analyse und zwar auf neue und bedeutend bessere Weise. Des Weiteren wird gezeigt, dass der W7-X Spulensatz genügend Freiheitsgrade besitzt, das viele wichtige Langzeitplasmaeffekte effektiv während kurzer Betriebszeiten ge-

testet werden können. Das eröffnet die Perspektive zahlreicher Forschungsmöglichkeiten während der frühen Betriebsphasen, was wiederum zu einer signifikanten Beschleunigung des wissenschaftlichen Programms und zu einer Optimierung des Divertorbetriebs bei W7-X führt. Die größte wissenschaftliche Herausforderung in Bezug auf den Betrieb der Insel-Divertoren von W7-X ist,da die Divertor geometrie fest ist, dass die Struktur des magnetischen Feldes der Divertorgeometrie angepasst werden muss bzw. dass zusätzliche dem Plasma zugewandte Komponenten hergestellt und installiert werden müssen. Noch bevor diese Arbeit geschrieben wurde, gab es einen Vorschlag für ein zusätzliches Plasma zugewandte Komponente, die sogenannten Scraper Elemente (SEs). Als Teil dieser Arbeit wurden Computersimulationen durchgeführt, um die Wissensbasis über die SEs zu vergrößern. Zur Analyse der Effecte des SE wurde der Plasma Randschicht Physik Simulationscode EMC3-Eirene benutzt in Kombination mit den aktuellesten Magnetohydrodynamik Gleichgewichts Rechnungen. Diese Kombination ist rechnerisch schwierig und hat zu wichtigen Erkenntnissen geführt. Ein Ergebnis dieser Studie ist, dass SEs die Abführmöglichkeiten der Partikel während des Dauerbetriebs signifikant reduzieren. Dies ist für den Dauerbetrieb von großer Relevanz.

Um diese negativen Effekte weiter zu analysieren und zu quantifizieren sollten physikalische Experimente mit einem SE Prototyp so bald wie möglich durchgeführt werden. Vorteilhaft wäre dies in der ersten Betriebsphase vor der ungefähr zweijährigen Pause, die notwendig sein wird, um W7-X für den dauerhaften Betrieb fertigzustellen. Während dieser ersten Betriebsphase ist jedoch die notwendige Kombination von Plasmaparametern, Heizleistung und erreichbarer Impulslänge nicht gegeben. Auf der einen Seite bedeutet dies, dass das beschriebene Problem für die erste Betriebsphase nicht eintreten wird, andererseits bedeutet es aber auch, dass in dieser Phase die physikalischen Folgen einer SE-Installation nicht experimentell getestet werden können. Eine wichtige Erkenntnis aus dieser Arbeit ist, dass das Spulensystem von W7-X genug flexibel ist, um solch einen frühen experimentellen Test zu ermöglichen. Verschiedene Stadien der Hochleistungsentladung können tatsächlich durch eine zielgerichtete Verwendung der verfügbaren Spulensätze nachgeahmt werden. Auf diese Weise wird hier gezeigt, dass in diesen frühen Betriebsphasen des W7-X -Programms sowohl die Schutzfunktion der SEs beurteilt werden kann, als auch die Effekte der Teilchenabfuhr und die Plasmaperformanz im Allgemeinen.

Diese Simulationsszenarien ermöglichen außerdem andere Wege des Divertorschutzes neben den SEs zu testen. Die verschiedenen Strategien werden in der vorliegenden Dissertation beschrieben. Am vielversprechendsten erscheinen dabei die hier erforschten und

sogenannten „dynamische Plasma-Achsenverschiebung“und die „Rand-Iota-Kontrolle“. Beide verändern das Magnetfeld am Rand so, dass es sich der Divertorgeometrie besser anpasst. Dies passiert langsam, aber dynamisch, das heißt während einer langen Plasmaentladung. Hier eine kurze Zusammenfassung der Unterschiede zwischen Iota-Kontrolle und Plasma-Achsenverschiebung:

Bei der Iota-kontrolle wird die Struktur des Randmagnetfelds konstant gehalten, indem die Effekte der sich entwickelnden Plasmaströme durch Ströme in externen Spulen kompensiert werden. Die benötigte Stromänderung in den externen Magnetspulen ist hierbei erheblich. Der Ansatz der Plasma-Achsenverschiebung lässt eine Entwicklung des Randmagnetfeldes gleichzeitig mit der Entwicklung der Plasmaströme zu, ermöglicht aber dadurch, dass der Ort des Plasmas geändert wird, dennoch einen sicheren Divertorbetrieb.

Abstract

Nuclear fusion is the energy source of the stars and has the potential of being the main energy source for mankind in the future. The research on fusion energy focuses primarily on magnetic confinement, where hot plasma — with temperatures on the order of 100 million degrees Celsius — are confined by specially designed toroidal magnetic topology. The main candidates for magnetic confinement are the tokamak and the stellarator. The tokamak concept is further developed than the stellarator concept, but the stellarator concept has some intrinsic and potentially very important advantages and is therefore also actively pursued. The Wendelstein 7-X (W7-X) stellarator will be the world's leading stellarator experiment. It is about to go into operation in Greifswald, Germany. This thesis delves into some very important scientific challenges for the stellarator concept as a whole and W7-X in particular, namely, how one effectively interfaces the hot plasma with the material walls of the experiment, in special how the plasma heat and particle fluxes are controlled. The fundamental concept that will be used in W7-X for particle and heat exhaust is the *island divertor*. Although the divertor concept at a stellarator was invented by Lyman Spitzer back in the 1950s [1], the stellarator island divertor still needs to be experimentally tested at fusion-relevant heat loads and temperatures in steady-state. W7-X is the first experiment that will be able to do so.

A number of theoretical and numerical studies have been performed to guide the design of the divertor components. The actual divertor components are in series production at this time, and are largely compatible with the expected heat loads. However, with the sophisticated codes now available, it has become clear that there are some, otherwise very attractive, operational scenarios that could lead to overloading of the W7-X divertors. At least one mitigation strategy was proposed but was until now not analyzed in sufficient detail. In this thesis, state-of-the-art codes are used to analyze this previously proposed mitigation strategy; they are also used to develop several alternative mitigation schemes, which may in the end be advantageous.

The work performed here shows not only that it is conceivable to solve this already identified problem in new and arguably better ways but also that the W7-X coil set has enough degrees of freedom that many important long-pulse plasma effects can be effectively mimicked in short-pulse operation. This opens up a rich research program in the early phases of operation and may therefore lead to a significant acceleration of the scientific program to control and optimize the divertor operation in W7-X.

The main scientific challenge for the island divertor operation in W7-X is that, since

the divertor geometry is now fixed, the magnetic field structure must be adjusted to the divertor geometry, or additional plasma-facing components must be manufactured and installed.

Well before this thesis work was done, such additional plasma-facing components were proposed. These are called scraper elements (SEs). As a part of this work, computer simulations were performed in order to obtain a better knowledge base regarding the SEs.

To analyze the effect of the SE, edge plasma physics simulation code EMC3-Eirene, was used, in combination with state-of-the-art magneto hydrodynamic (MHD) equilibrium codes. This combination was computationally non-trivial and new, and it has led to important insights. One main result of this study is that the SEs significantly reduce the particle exhaust capabilities in steady state operation; this is a concern for W7-X.

To test and further quantify this deleterious effect, physics experiments with a prototype SE should be performed as soon as possible, ideally in the first operation campaigns before the approximately two-year break needed to complete W7-X for steady-state operation. In this first operation phase, however, the necessary combination of plasma parameters, heating power, and achievable pulse length is not accessible. This means, on the one hand, that the problem described will not be present in the first operation phase; on the other hand, the physics implications of installing an SE would appear not to be experimentally testable in that phase. One major finding of this thesis is that the coil system of W7-X is flexible enough to allow such an early experimental test. Different stages of high performance long-pulse discharge can be effectively mimicked in the experiment by a targeted use of the available coil sets. Thus, even in the early phases of the W7-X program one can assess both the protection capabilities of the SEs and their effects on particle exhaust and plasma performance in general.

These *mimic scenarios* also have the potential to test other possibilities for divertor protection besides the SE. Such strategies are addressed in this thesis. The two most promising strategies identified here can be classified as *plasma shift* and *iota control*. Both adjust the edge magnetic field to better fit the divertor geometry. This is done slowly but dynamically — i.e. during a long plasma discharge. The differences between iota control and plasma shift can be quickly summarized as follows:

In iota control, the edge magnetic field topology is kept constant by negating the effects of evolving plasma currents through changes in external coil currents. The external field changes needed for this strategy are substantial.

The plasma shift approach lets the plasma edge topology evolve as the plasma currents

evolve but nonetheless allows a safe divertor operation by shifting the location of the plasma.

Contents

1 Introduction

In this thesis, various questions concerning the upcoming experiment Wendelstein W7-X are addressed and investigated using computer simulations. Numerical simulations are used to interpret, predict or prepare real experiments. They provide basic understanding and allow to to be identify trends.

Due to faster computers and more advanced codes the importance of computer simulations has grown and will continue to grow over time. In some areas of physics research, experiments already heavily depend on simulations. The results of experiments are checked with simulations, and the simulations are rechecked with new experiments. This iteration loop helps us to understand physics. In high-energy physics, for example, measurement data is always verified by comparison with the simulation data. Thus, deviations between measurement and simulation deliver new findings such as the Higgs boson at CERN.

In the case of Wendelstein 7-X, there is no experimental data yet, so computer simulations are the only possible way to understand the machine and to make predictions of how the plasma will behave.

Simulations are also of special importance to make last-minute adjustments to the device and to define possible experiments that can be realized when W7-X is running.

In this work, the calculations were performed with EMC3-Eirene, field line diffusion, field line tracing and ray tracing, in order to access questions of interest for the operation of W7-X. EMC3-Eirene is used because of its leading position as the most advanced simulation for edge modeling. The field line diffusion approach, on the other hand, is one of the fastest methods and is well suited for testing different configurations. For the magnetic field, both vacuum fields as well as equilibrium fields were used.

After the introduction, where W7-X, its operation phases and potential challenges are introduced, this work has four main topics. As a first topic, the analysis of the side effects of an additional divertor component (Scraper Element [2]) will be described. This will be followed by the outline of test configurations that are able to reproduce several aspects of the later foreseen high performance scenarios. Thirdly, an evaluation

of solutions for divertor protection other than the Scraper Element will follow. And last, some supporting research for a simplified geometry concerning an early first plasma operation completes this thesis.

2 Wendelstein 7-X

2.1 General

Wendelstein 7-X (W7-X) is a nuclear fusion experiment located in Greifswald, Germany [3]. It is a pure research project; no deuterium/tritium operation is planned and therefore no energy production will take place. The first plasma operation is planned for 2015. The main objectives are to demonstrate the relevance of the stellarator type as a reactor i.e. high performance operation, the magnetic confinement and the unique island divertor concept. High performance operation means a plasma with a large triple product, i.e. $n \cdot T \cdot \tau$, with n the density, T the temperature (ideally of ions) and τ the energy confinement time. The large triple product should be achieved at high field strength, i.e. 2.5 T for W7-X.

In contrast to the tokamak type the stellarator is able to create the confining magnetic field solely by its external coils. In a tokamak a toroidal current generated by a magnetic transformer is used to twist the field lines. In a stellarator a more complex magnetic coil geometry is necessary, but no transformer is required. This fact allows steady-state operation, which is of great relevance for commercial use.

In the stellarator line, W7-X is one of the largest and the most sophisticated device ever built. Some of its parameters are shown in table 2.1.

W7-X is five-fold periodic [4]. This means that each of the five modules is identical (except for small details). In addition, W7-X is stellarator symmetric, which means that each module is upside-down mirror symmetric ($\psi(R, \phi, Z) = \psi(R, -\phi, -Z)$) [5].

2.2 Coil System

W7-X is a fully optimized stellarator and uses 70 superconducting and 15 normal conducting coils for creating the magnetic field [7]. These magnetic coils are able to create a 2.5 T magnetic field at the axis and provide a wide range of possible options to adjust it. These coils can be classified into five different groups. The modular coils are used

Table 2.1: *Technical data W7-X [3], [6].*

Plasma major radius	5.5 m
Plasma minor radius	0.53 m
Plasma vessel volume	ca. 30 m^3
Magnetic field (at axis)	3 T
Periodicity	5

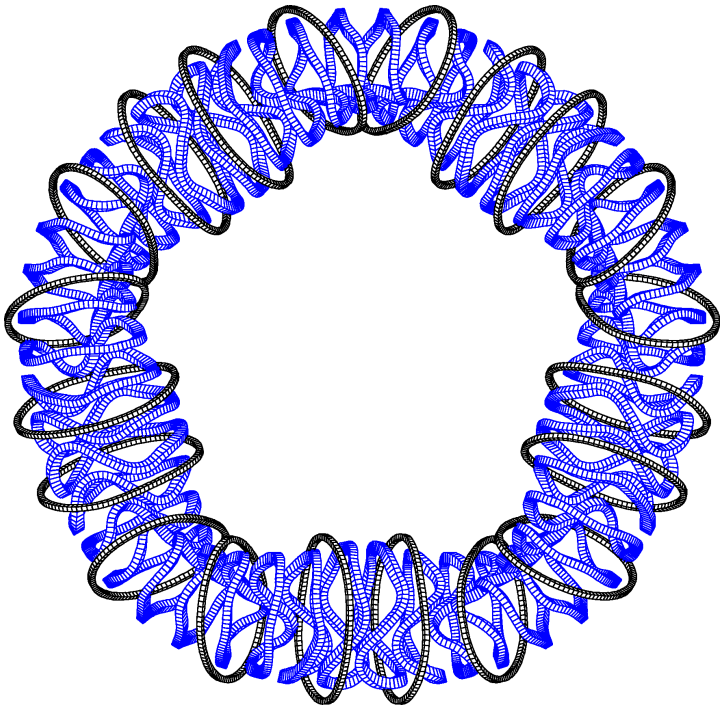

Figure 2.1: *Modular coils (50) and planar coils (20). Not shown coils for modification: Trim coils (outside of the machine) and control coils (inside). Picture from [8].*

for the plasma confinement, the planar coils to control the major adjustment of the magnetic field, the sweep coils (also called control coils) to vary the position and size of the boundary islands and the trim coils to add or suppress periodic error fields.

2.2.1 Modular coils

To confine the plasma, W7-X uses 50 modular, superconducting coils. Figure 2.1 shows the arrangement. These modular coils alone create a twisted magnetic field that is able to confine a plasma. Because of the periodicity and the stellarator symmetry of W7-X, there exist only five different shapes for these 50 coils. Figure 2.2 shows the coils in one module. The coils are symmetric in the middle of the module. Each of these coils has 108

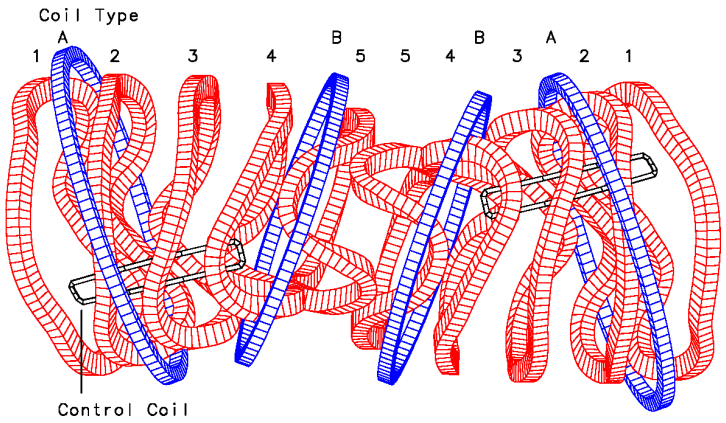

Figure 2.2: *Coils of one module. Red: Modular coils. Blue: Planar coils. Grey: Control (sweep) coils. There are five different types of modular coils. The coil sequence is mirrored at the middle of the module. The planar coils are also stellarator symmetric. The sweep coils are not symmetric and break the stellarator symmetry. Picture from [8].*

windings. As it is only possible to adjust the current for all members of the group, there are five parameters for selecting the currents of the modular coils, here named I_1 to I_5. All currents in this work are given as normalized total current, which means the current per winding multiplied by the number of windings and a scaling factor. The scaling factor is the same for all coil types (modular, planar, sweep, trim). The scaling factor determines the magnetic field strength but does not change the topology of the magnetic configuration. Table 2.5 shows the scaling I_n for all vacuum reference configurations to reach 2.5 T on the magnetic axis.

Magnetic mirror

Different magnetic mirror ratios are possible in W7-X. The mirror ratio is controlled by the modular coil system. When the currents decrease, going from coil 1 to coil 5, the configuration has a high mirror ratio. When the currents increase, the magnetic field has a low mirror. This mirror ratio affects how particles with banana orbits are reflected, which in turn has a big impact on other properties like toroidal currents.

2.2.2 Planar coils

W7-X has 20 additional superconducting coils that are not mandatory for plasma confinement but enable major adjustments to the magnetic field. There are two groups of these coils, named “planar coil A” and “planar coil B”. Both types have 36 windings.

Again, total currents which are normalized to the scaling factor (see 2.2.1) are used. Figure 2.1 and 2.2 show the position of these coils.

For the purposes described in this thesis, the planar coils serve two functions: first, to change the twist of the magnetic field (i.e. to change the iota value) and, second, to move the plasma axis radially. It is possible to do both at the same time.

Iota

The twist of the magnetic field, ι, is also known as the rotational transform or field line pitch and describes the number of poloidal turns per toroidal turn.

$$\iota = \text{poloidal transits per single toroidal transit} \tag{2.1}$$

$$\iota = \iota \cdot 2 \cdot \pi \tag{2.2}$$

To change ι, the A and B coil current together must differ from zero. When $I_A + I_B > 0$, the iota value is decreased. When $I_A + I_B < 0$, the iota is increased.

Natural islands need a rational value of ι. The lowest orders accessible in W7-X are 5/4, 5/5 and 5/6, which results in 4, 5 and 6 islands respectively.

Plasma shift

When the A and B coils are used in opposite directions, a net vertical field is generated that shifts the plasma axis radially. The shift direction is outwards for $I_A - I_B < 0$ and inwards for $I_A - I_B > 0$.

2.2.3 Control coils

To make subtle adjustments to the magnetic field, there are 10 normal conducting coils. These coils are designed to allow fast changes and are located inside the vacuum vessel. For the purposes in this thesis, these coils have two functions: moving the islands poloidally and changing the island size. They have eight windings and come in two groups, named as $s1$ and $s2$. See figure 2.2 for their location. Of note is, that if these coils are used for moving (sweeping) the islands then the magnetic field is not stellarator symmetric anymore.

Island size

To change the size of the islands, the currents of the sweep coils must be in opposite directions. The island size is increased for $I_{S1} - I_{S2} < 0$ and decreased for $I_{S1} - I_{S2} > 0$. The main effect is a modification of the island width.

Sweeping

The sweep coils can be used with the same current sign to change the island position poloidally. Doing this at a high frequency allows the heat load to be spread out on the divertor components (the divertor is described in section 2.3.1). This increases the wetted area on the divertor and therefore decreases the power per area.

2.2.4 Trim coils

The five trim coils are normal conducting coils and located at the outside of W7-X. The main purpose of this coil system is to compensate a large scale error fields (or to create them). An error field would lead to asymmetric heat loads on the divertor units and therefore to a higher peak load at some units. This could cause damage at these units.

2.3 Heat exhaust

For timescales longer than the energy confinement time ($\sim 0.6\,\mathrm{s}$ [9]) the heat exhaust is the same as the heating power. Therefore, while heating with 10 MW in steady state operation, the same amount of energy must be exhausted at another point. This diversion of energy must take place at a predetermined location under controlled conditions to protect weak components and enable density control.

To enable a controlled heat exhaust, different solutions were developed previously. Two of these are the divertor and the limiter, shown in figure 2.3.

The first plasma operation (fall 2015) will use a limiter configuration. In this configuration, the closed flux surfaces are intercepted by the wall, no special magnetic edge topology is used. Therefore, the plasma size in this case is directly restricted by the limiter. Figure 2.3a shows this limiter concept in general and figure 2.3b sketches the situation in W7-X. Some basic work for the limiter phase was done as a part of this thesis; for details see chapter 8.

For the later operation, the island divertor concept will be used [10]. One of the possible configurations uses five x-points and therefore five island chains, schematically

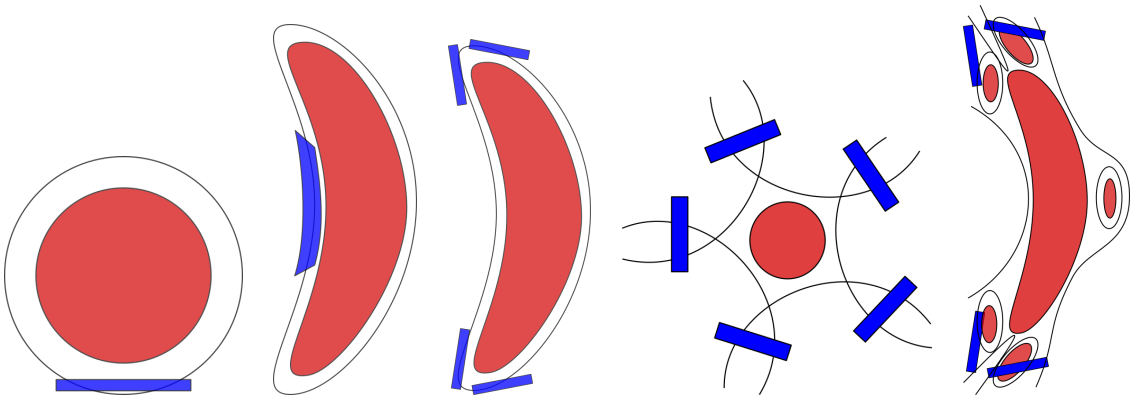

(a) limiter (b) limiter (c) limiter (d) divertor (e) divertor

Figure 2.3: *Sketches of divertor configurations. Each configuration consists of a hardware configuration (divertor or limiter) and a magnetic field configuration. The magnetic field configuration determines the kind of operation (limiter or island divertor operation). (a) Typical limiter configuration. (b) W7-X test plasma limiter (OP1.1) with limiter configuration (c) W7-X limiter configuration with island divertor (OP1.2+) (d) Sketch of island divertor concept (e) W7-X island divertor (OP1.2+) with island divertor configuration (standard configuration)*

shown in figure 2.3d. In W7-X, the cross section of the flux surface in the divertor region is squeezed and therefore, the actual configuration looks more like 2.3e.

With the divertor installed, it is also possible to run a limiter configuration by choosing a special magnetic configuration, shown in figure 2.3c.

2.3.1 Wendelstein 7-X divertor

The divertor concept used in Wendelstein 7-X is a modular island divertor, the plasma-wall interactions are designed to be concentrated at the ten independent divertor units. For optimum performance, only the divertor target plates should connect to the magnetic islands. The divertor geometry is suitable for a large range of different configurations. Configurations with 4, 5, 6 or zero islands are appropriate, as well as different magnetic mirror ratios and different magnetic axis positions.

Figure 2.4a shows an image of one divertor unit. The only parts of the divertor units that are designed to be in direct contact with the plasma are the target plates (blue area). This part can be divided again into four areas: horizontal divertor target plate, vertical divertor target plate, high iota tail target plate and the low loaded area. The target plates are designed as a high loaded area that can resist the highest heat load. At the target plates, the plasma recombines into neutral gases that then can be removed

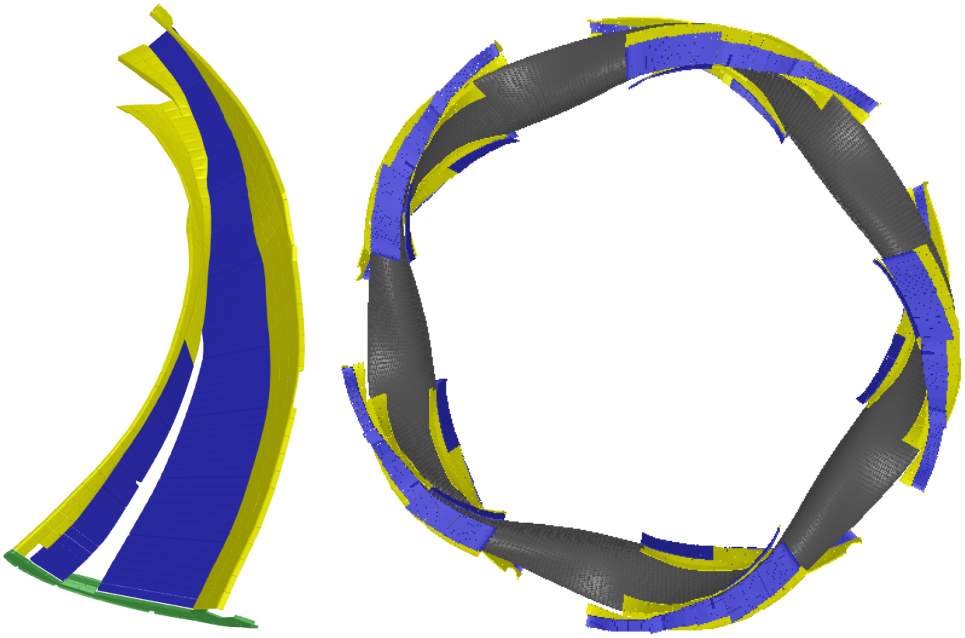

(a) W7-X divertor (b) Top view W7-X divertor system

Figure 2.4: *W7-X divertor units. (a) CAD image of a one W7-X divertor unit. (b) CAD of a top view at W7-X. Blue: divertor target plates, yellow: baffle plates. gray: flux surface (separatrix).*

from the vessel. The other part of the neutral gas stream back into the plasma and get ionized. This is necessary for controlling the plasma density.

To do so, there are two pumping gaps where the neutral gas can propagate into the divertor chamber where the pumps are located. The small pumping gap is located at the high iota tail, and the main gap is between the horizontal and the vertical target plates. The target plates right beside the pumping gaps have a leading edge where the maximum allowed heat load is reduced. This area is of special interest later in this work. The area right beside the pumping gap is called “end top tile” and the area inside the pumping gap the “gap tile”.

The neutrals are guided by the baffle plates towards the divertor. These plates increase the pumping efficiency and protect the vessel wall. But they are not designed to withstand continuous converted power.

The heat shield covers other regions of the vessel which need additional protection. The heat shield surrounds the torus in a stripe and covers the whole area in the triangular plane.

The technical limits of the various components are shown in table 2.2.

Table 2.2: *Technical limits of maximal heat load for the main components in W7-X [11], [12].*

Component	**Max peak**	**Max average**
High loaded area ($19\,m^2$)	$10\,MW/m^2$	$3\,MW/m^2$
- End top tile	$5\,MW/m^2$	X
- Gap tile	$2\,MW/m^2$	X
Low loaded area ($6\,m^2$)	$1\,MW/m^2$	$500\,kW/m^2$
Baffle ($33\,m^2$)	$500\,kW/m^2$	$250\,kW/m^2$
Toroidal closure ($3\,m^2$)	$500\,kW/m^2$	$250\,kW/m^2$
Poloidal closure ($9\,m^2$)	$200\,kW/m^2$	$100\,kW/m^2$
Heat shield - higher loaded area ($17\,m^2$)	$500\,kW/m^2$	$250\,kW/m^2$
Heat shield - lower loaded area ($30\,m^2$)	$300\,kW/m^2$	$150\,kW/m^2$
Stainless steel wall panel ($60\,m^2$)	$200\,kW/m^2$	$100\,kW/m^2$
Plasma vessel wall ($\sim 220\,m^2$)	$1.9\,kW/m^2$	$1.4\,kW/m^2$

Table 2.3: *Operational phases*

Name	Date	Description
OP1.1	2015	Limiter configuration
OP1.2a	2016/17	Uncooled divertor configuration
OP1.2b	2017	Uncooled divertor configuration with SE
OP2	$>$ 2019	Steady-state operation with cooled divertor

2.4 Operation phases

It is planned that W7-X will run in steady state, but first, expertise about the operation of the experiment must be developed. Therefore, other operation phases are planned before the steady state operation. In these early phases, W7-X will be equipped with more robust installations. This has the advantage of risk mitigation, especially at plasma start-up. There are two phases planned, these are subdivided into four phases in total: OP1.1, OP1.2a, OP1.2b and OP2.

The first plasma operation will be in a limiter configuration with an uncooled graphite limiter. This phase is called OP1.1. The next operation phase is called OP1.2 and will use an uncooled divertor (Test Divertor Unit (TDU)). The second operation phase (OP2) uses the water cooled divertor (High Heat Flux Divertor Unit (HHF-DU)). Both divertors have the same surface geometry. Table 2.3 shows the expected dates and some configuration details.

In OP1.1 and OP1.2 the plasma parameters are limited due to the uncooled components. Therefore, the energy applied by the heating system for one discharge is limited.

Table 2.4: *Limits of the different operation phases [13].*

	OP1.1	**OP1.2**	**OP2**
Heating	$< 5\,\mathrm{MW}$	$\leq 10\,\mathrm{MW}$	$\sim 10\,\mathrm{MW}$
Limit	$\int Pdt \leq 2\,\mathrm{MJ}$	$\int Pdt \leq 2\,\mathrm{MJ}$	$P/A \leq 10\,\mathrm{MW/m^2}$
Pulse length	$\sim 1\,\mathrm{s}$	$\sim 10\,\mathrm{s}$ or $60\,\mathrm{s}$ at reduced power	$30\,\mathrm{min}$ at $10\,\mathrm{MW}$
Density limit	$0.2 \cdot 10^{20}\, m^{-3}$	$1.6 \cdot 10^{20}\, m^{-3}$	$2.4 \cdot 10^{20}\, m^{-3}$
β limit	$1.6\,\%$	$3\,\%$	$5\,\%$

Between the plasma discharges, there will be a pause for cool-down.

In the second operation phase, all components are actively cooled. Therefore, the limiting factor is the heat flux to the components and, of course, the maximum cooling capability.

Table 2.4 shows the probable parameters for the operation phases.

2.5 Vacuum reference configurations

The modular coils alone are able to create a magnetic field which can be used for plasma operation. This magnetic field configuration is named the "standard configuration". Figure 2.6 shows its Poincaré plot. As described in section 3.1, a Poincaré describes the structure of a magnetic field configuration.

Eight additional configurations were used for the previous divertor optimization, giving a total of nine so-called Vacuum Reference Configuration (VRC). These VRC are relevant to treat different physical questions. Some of these topics are fast particles confinement, bootstrap current, Shafranov shift, the island divertor in general, and particle and heat exhaust.

Table 2.5 shows the coil currents of these VRC.

In the limiter case the last closed flux surface connects directly to the island target plate. The other eight cases use the island chains to connect to the divertor target plates. High iota is the only configuration with four islands and low iota the only one with six islands. The other six cases have five island chains. Different magnetic mirror ratios – low mirror/standard/high mirror – affect the neoclassical confinement and the stability of the configurations to small field changes. The most optimized configuration is the high mirror configuration (low Shafranov shift, low Bootstrap current, small β-effect, robust against small perturbation) [3]. But on the other hand the highest confinement times are predicted for the configurations with a mirror ratio close to the standard mirror

Table 2.5: *Vacuum reference configurations [8]. Scaling factor I_n for 2.5 T on magnetic axis.*

Name	I_A	I_B	I_1	I_2	I_3	I_4	I_5	I_n [MA]
Standard	0.00	0.00	1.00	1.00	1.00	1.00	1.00	1.45
Low iota	0.25	0.25	1.00	1.00	1.00	1.00	1.00	1.32
High iota	-0.23	-0.23	1.00	1.00	1.00	1.00	1.00	1.60
Low mirror	0.00	0.00	0.94	0.98	0.98	1.06	1.06	1.49
High mirror	0.00	0.00	1.08	1.05	1.00	0.95	0.92	1.44
Low shear	-0.20	0.20	1.13	1.12	1.05	0.85	0.84	1.47
Inward shifted	0.10	-0.20	0.96	0.95	0.97	1.07	1.08	1.47
Outward shifted	-0.14	0.14	1.04	1.04	1.01	0.96	0.96	1.46
Limiter	-0.10	0.20	1.07	1.10	1.02	0.92	0.89	1.43

ratio.

The plasma axis position – inward shifted, standard, outward shifted – determines where the islands connect to the divertor target plates. Finally, the "low shear configuration" uses a different shear value which means the dependency of ι to the radial position is smaller. The shear impacts the plasma stability and the size of the magnetic islands.

2.5.1 Configurations with five islands

The configurations with five islands, have a special symmetry and are of high interest. For a configuration with five islands the ι at the island chain is $5/5 = 1$. This means that a field line starts at the center of one island and reconnects itself after one toroidal turn. Therefore, in these five-island configurations all islands are separated from each other and there is no direct connection between the islands, in contrast to the four or six island configurations where all islands are in fact the same flux bundle.

Depending on the configuration details, an island connects to two or four divertor modules (for configurations with five islands).

For clarification, table 2.6 illustrates how the islands move poloidally during a toroidal turn. In general, each island is in contact with the divertor plates at four different locations. For example, the island colored in blue, connects first with the upper vertical divertor in module one, then with the lower vertical divertor in module 2, next at the lower horizontal divertor in module 3 and last at the upper horizontal divertor in module 5.

It is also possible, if the island position is shifted by a small amount, that there is

only a connection to the vertical or the horizontal divertor. In this case, the blue colored island would connect to module 1 and 2 or 3 and 5. This is of interest because this could cause higher heat loads at the intersected target plates.

The island behavior described is of particular importance when breaking the symmetry by installing different numbers of components (for example only two elements) in the ten different divertor modules. This is the case for early tests, as described in chapter 6.4.

	bean plane:0°	12°	24°
Module 1 (0-72°)	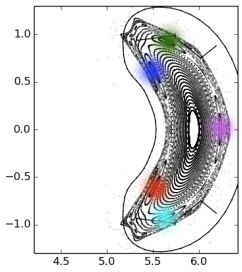	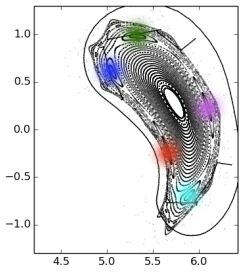	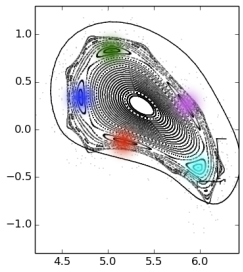
Module 2 (72-144°)	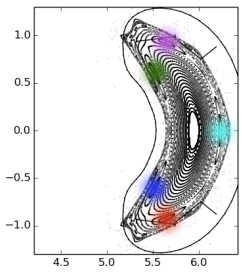	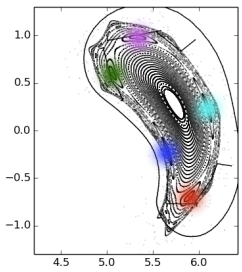	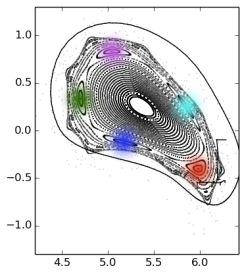
Module 3 (144-216°)	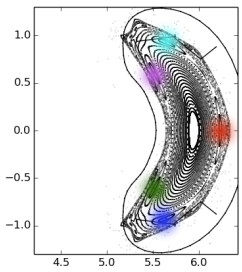	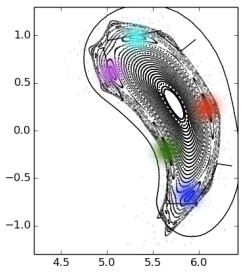	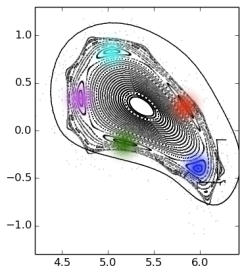
Module 4 (216-288°)	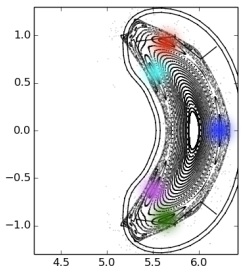	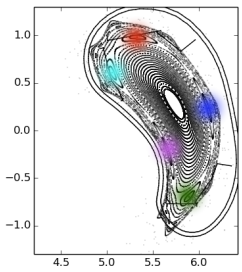	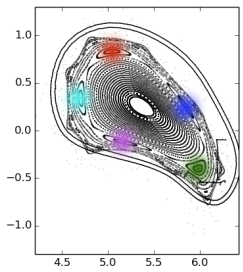
Module 5 (288-360°)	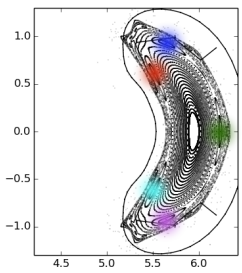	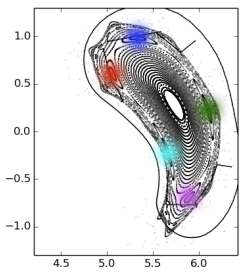	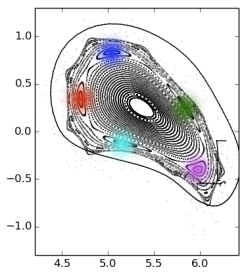

Table 2.6: *Cross sections of W7-X with magnetic field. One cross section every* 12°*. Magnetic*

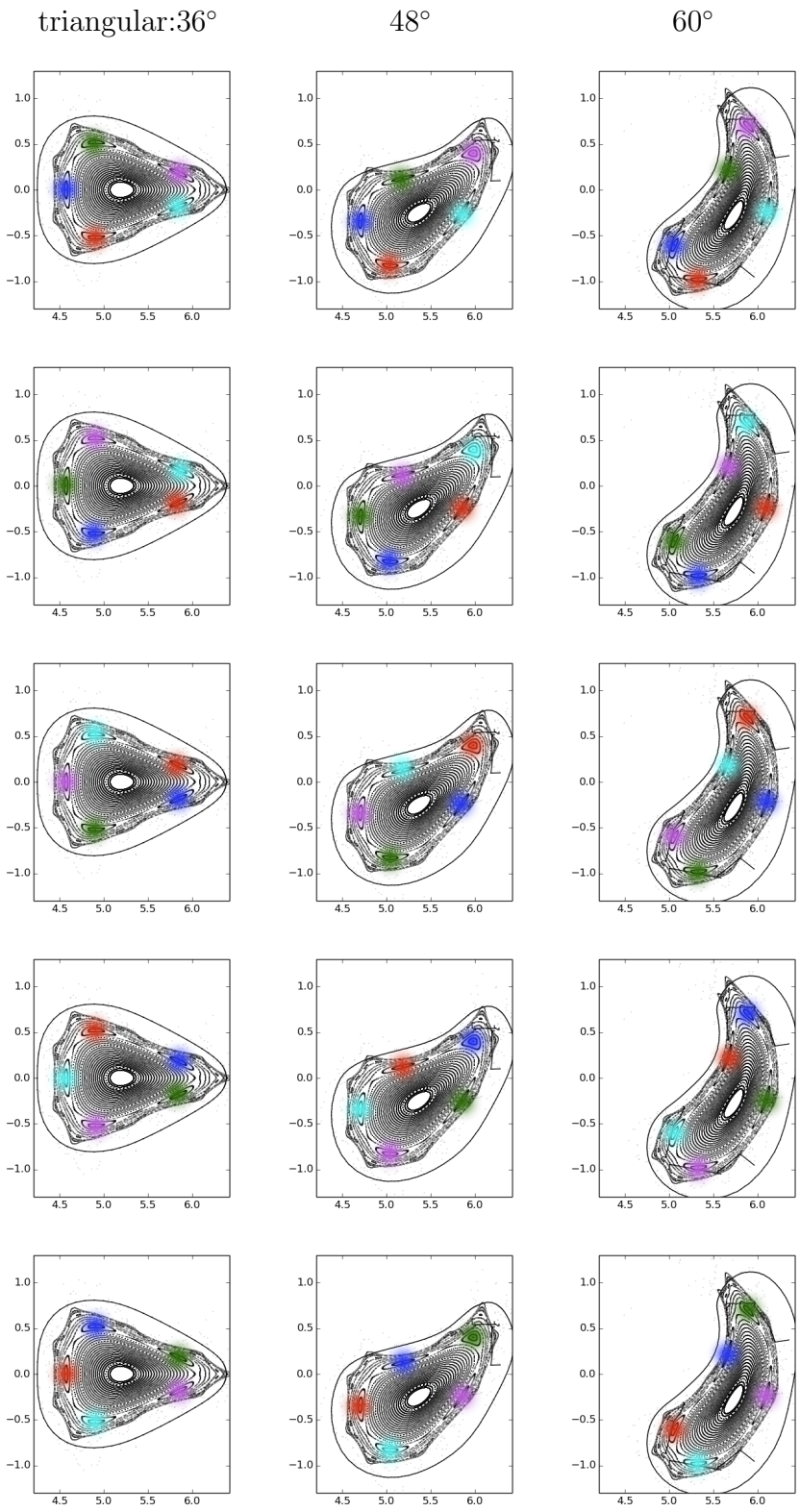

field: standard configuration. The five islands are colored for better distinction.

3 Methods

In this work several different approaches are used to make predictions concerning the edge physics of W7-X. A rough overview of their characteristics is given here.

3.1 Poincaré

A Poincaré plot is one method to illustrate the magnetic field structure. It shows the "puncture points" of field lines through a plane at fixed ϕ (ϕ is the toroidal coordinate). To display the flux surface structure, it is necessary to trace one field line multiple times around the torus. The computing time of this method is very fast (seconds to minutes), and it is easy to do for all magnetic field configurations.

The IPP Web services [14] were used for field composition, tracing and to interact with the geometry files. The process is as follows: The first step is to prepare the W7-X geometry: baffles, divertor, heat shield, etc. Subsequently, the magnetic field is created. For the magnetic field, either a vacuum field (created with the Biot-Savart law) is used or a converted equilibrium field is loaded. Next, the starting points for the tracing are created. By default, 40 points from r = 6.0 m to 6.4 m along the ϕ,z = 0 line are used. These points are then traced for multiple toroidal turns, following the field lines; in this work, 300 toroidal turns is the default value. If possible, the five-fold symmetry of the device is employed. This is not possible for asymmetrical configurations that use the sweep coils for sweeping the islands or the trim coils for creating a field error. The last step is to plot the puncture points together with the cross section of the compoments.

3.2 Ray tracing

In addition to convective heat transfer (described in section 3.1), heat deposition on the vessel and in vessel components is also caused by radiation of the main plasma species, as well as of impurities. To estimate the level of heat load resulting from radiation, a ray tracing method is used. The radiation is expected to be spread out in straight lines.

The x-points between the islands are assumed to be the source location of this radiation This is a fast method (hours to days).

Again, the Web services were used for field composition, field line tracing and to interact with the geometry files. To recapitulation the process: Firstly the geometry files are loaded. Next, the Biot-Savart law is used for a vacuum field or a converted equilibrium field is loaded. The starting points for the tracing are created, followed by the tracing of the x-point for one toroidal turn. Afterwards, this data is duplicated and shifted one period. This is repeated until all five x-point lines are created. Next, the photons are simulated as lines that radiate from the x-point-lines in random directions. An intersection of these paths with a geometry is treated as an energy transfer.

Now, the heat load (MW/m^2) per area is calculated and the data is stored.

3.3 Field line diffusion

Usually, the main heat transfer to the divertor target plates is via convective heat transfer. This means, in a simple picture, that the plasma connects directly to the divertor surface. In this simple picture, only the area in contact gets heat load. This "wetted area" is called the strike line (the shape of the wetted area is usually a line). One method to determine where the strike lines are located is field line tracing. It is possible to calculate a heat load prediction or, for a faster computation, to only calculate the location and shape of the strike lines.

The general approach is to trace start points following the magnetic field lines and meanwhile displace those points perpendicularly to the magnetic field to simulate particle and energy transport. An intersection with a geometry component is treated as an impact of an ion causing an energy transfer. This method is fast (hours to days), easy to use for all magnetic fields and well tested.

With this approach as well, the Web services were used for field composition, field line tracing and to interact with the geometry files. The procedure is approximately as follows: At the beginning, the geometry of the components such as divertor, baffles, heat shield, etc is loaded. Second, the magnetic field is created; the Biot-Savart law is used for the vacuum field or a converted equilibrium field is loaded. Next, the starting points are created by finding the separatrix and placing points on its surface. Each starting point is traced by following the field lines for a certain distance, then a random displacement of the points perpendicular to the magnetic field is performed. This random step represents the perpendicular diffusion caused by effects like collisions and turbulence.

This procedure is repeated until a geometry element is hit. The number of intersections at this geometry element is summed up to calculate the energy per area.

The procedure is repeated by tracing each starting point in the other direction. If possible, the five-fold symmetry of the device is used. This is not possible for asymmetrical configurations which use the sweep coils for sweeping or the trim coils for an error field. Lastly, the energy per area is calculated.

The strike line width (and therefore also the peak heat fluxes) in this approach depends on the ratio of the transport parallel to the magnetic field to the transport perpendicular to the field. The parameters used in this work are: perpendicular diffusion (D): $1\,\mathrm{m}^2/\mathrm{s}$. Velocity ($v$): $1.4\cdot10^5\,\mathrm{m/s}$ for engineering relevant questions and velocity (v) of $2\cdot10^6\,\mathrm{m/s}$ for comparison of magnetic field configurations.

For W7-X both values (D and v) are unknown. In the previous experiment W7-AS, D was around $1\,\mathrm{m}^2/\mathrm{s}$. The particle velocity can be estimated by [15]

$$v = \sqrt{k_B(T_e + T_i)/(m_i + m_e)}. \tag{3.1}$$

The value of the velocity of $1.4 \cdot 10^5\,\mathrm{m/s}$ correspond with the temperature of the edge region in the EMC3 calculations of 200 eV (see electron temperature in figure 5.7). The higher values of $2 \cdot 10^6\,\mathrm{m/s}$ result in smaller and clearer strike lines and are used for having a better comparison between real and mimic configurations (see chapter 6).

For the collisional mean free path a value of 0.1 m is used. In other experiments, this value ranges from 0.01 m (JET) to 2.5 m (CMOD) [15].

3.4 EMC3-Eirene

EMC3 is an advanced computer code to simulate the plasma edge transport. EMC3 has a similar application area as the field line diffusion but is much more complex and is able to answer additional questions by better representing physical effects. This means that the solutions calculated by EMC3 are better predictors.

The general approach is to treat the ions and the electrons as two fluids. The neutral effects are calculated with the Eirene code and iteratively combined with EMC3. This method is rather slow (days to weeks) and can have technical problems for certain magnetic field structures. Therefore, it is not possible to run this simulation automatically for a number of magnetic configurations.

EMC3-Eirene is a full physics simulation of the edge plasma but uses the simplifica-

tions of a stationary plasma. This means no time-dependent dynamics, all parameters are frozen, and in particular, there are no plasma currents. In addition, quasi-neutrality of the plasma is assumed. In a real scenario, the plasma parameters will always undergo changes, and the magnetic configurations will therefore evolve in time. Thus, EMC3-Eirene only allows the simulation of quasi-stationary solutions by performing calculations at successive points in time.

The plasma transport is calculated by using the Braginskii equation (See [15], page 399) with the previously mentioned simplifications (stationary, no currents, quasi-neutrality). For the derivation of the simplified equations see [16].

On the technical side, the calculation grid creation can be very complex. A strategy for creation is shown in [16]. In this work, VMEC/EXTENDER solutions are used as the magnetic field; these require even more effort than vacuum magnetic field configurations because of the more stochastic field structure at the edge.

In this work EMC3 is used with equilibrium configurations calculated with VMEC and Extender, this was extremely new at the time of writing. In the past, a problem with $DivB! = 0$ at the edge between VMEC and Extender prevented it. The alternative combination of these two fields described in [17] overcomes this problem. The study presented here, is one of the first calculations using such an approach.

3.5 VMEC and EXTENDER

VMEC and EXTENDER are used for the generation of the MHD-equilibrium field [18], [19], [20]. They are used to calculate the magnetic field in the presence of a plasma. VMEC calculates a solution to the MHD force balance [18]:

$$\vec{F} = -\vec{j} \times \vec{B} + \vec{\nabla} p = 0 \tag{3.2}$$

$$\vec{\nabla} \times \vec{B} = \mu_0 \vec{j} \tag{3.3}$$

$$\vec{\nabla} \cdot \vec{B} = 0 \tag{3.4}$$

Because it assumes nested flux surfaces, VMEC cannot treat islands or stochastic regions.

To describe the edge region of the magnetic field, an additional code is applied, called EXTENDER. EXTENDER uses a virtual casing principle [20] for this job. In this thesis, both codes are consistently used together by applying the alternative method for combining the fields, see [17] for details.

These methods are fast (minutes to hours).

The equilibrium configuration used in this work was calculated by Joachim Geiger.

4 Challenges of high performance operation

To successfully produce energy in a future fusion facility, the "triple product" of plasma density, energy confinement time and plasma temperature must be above a certain threshold [21]. To demonstrate the reactor relevance of W7-X, a high triple product is the aim of OP2. In addition, long discharge times of up to 30 minutes are desired to demonstrate the steady state capability of the stellarator concept. These four requirements together shall be named "high performances scenarios" in this work.

High performance plasma scenarios are challenging to operate because of two effects which take place. These effects are the β-effect and the bootstrap current.

This chapter will describe the impact of these effects on the VRC.

To deal with these effects one possible solution was already invented in the past. This solution is called Scraper Element (SE), and is further described in this chapter.

These topics are of special interest to motivate the following chapters which analyze the effects of the SE, describes SE test scenarios and suggest alternatives to an SE.

4.1 Effects of plasma beta

In OP2, high plasma temperatures and high plasma pressures are planned. These values are in relation the the magnetic field strength. A value which takes this into account is the ratio of plasma pressure divided by magnetic pressure. This parameter is called the plasma β-value and defined as:

$$\beta = \frac{p}{p_{mag}} = \sum_i \frac{n_i \cdot k_B \cdot T_i}{B^2/2\mu_0}. \tag{4.1}$$

In this work, only the volume-averaged β-value ($\langle\beta\rangle$) is used. The β-value can be used to characterize a plasma scenario, in addition, many plasma behaviors are affected by

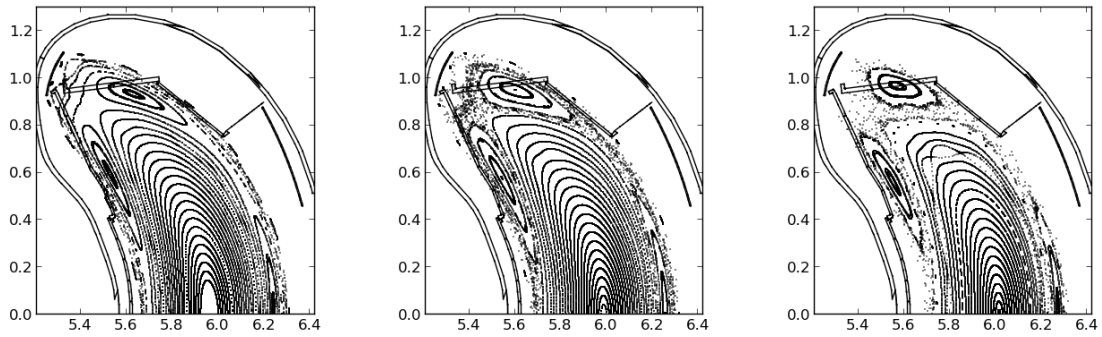

(a) 0.65 % (b) 2.0 % (c) 3.39 %

Figure 4.1: *Plasma beta scan: standard configuration. volume-averaged $\langle\beta\rangle$-values of: (a) 0.65 %. (b) 2.0 % and (c) 3.39 %.*

this value.

During plasma operation, different effects inside the plasma change the magnetic field. One effect is the Shafranov shift, which moves the plasma axis outwards radially [22]. This shift depends on the plasma β, higher β-values result in a larger shift. The Shafranov shift is caused by the Pfirsch-Schlüter current. Another current inside the plasma is the diamagnetic current. The shape of the island structure is affected by these plasma currents, mainly by the Pfirsch-Schlüter current [23]. These effects act on the timescale of the plasma confinement time ($\sim$ 100-300 ms). Therefore, they can be treated as constant when looking at much slower processes like the heat load distribution. All these effects dependent strongly on the plasma beta. The combination of all these effects will be referred to as "beta-effect".

Later in section 4.2 an additional current, the bootstrap current (I_BC) is described; this current evolves on a much longer timescale (on the order of minutes).

4.1.1 Beta effects on reference configurations

As mentioned in section 2.5, the divertor units have been designed based on several vacuum configurations. Due to plasma beta, however the resulting configurations differ, and that leads to different heat load distributions on the components inside the vessel.

Poincaré plots for different beta values for the standard configuration (as described in section 2.5) are shown in figure 4.1. The equilibrium calculation is described in section 3.5 and was performed by J. Geiger [24]. The plot for $\langle\beta\rangle$-value=0.65 % is very similar to the vacuum case, but for higher values the differences larger. The island shape evolves

(a) 0.65 % (b) 2.0 % (c) 3.39 %

Figure 4.2: *Strike line positions. Standard configuration. Plasma beta scan, volume average beta values: (a) 0.65 %, (b) 2.0 %, (c) 3.39 %.*

towards a more circular island form, the island width (dimension in radial direction) increases and the last closed flux surface is smaller.

With a field line diffusion approach (described in 3.3), it is possible to estimate where the heat flux is deposited to. The intersection points are shown in figure 4.2. For low $\langle\beta\rangle$, the standard configuration has one strike line at the horizontal and one strike line at the vertical target plate, and both are close to the pumping gap. For moderate $\langle\beta\rangle$ of about 2 %, an additional strike line appears on the horizontal divertor plate away from the pumping gap. For further increased $\langle\beta\rangle$ of about 3 %, this strike line hits the baffle plate at the high iota tail.

The appearance of this line is caused by an increased island structure together with a shift of the magnetic axis. This would cause an overload of the baffle structure, because this structure is not designed to be continuously loaded (see section 2.3.1).

Similar problems occur also for other configurations. For example, the strike line patterns of the low iota configuration are shown in figure 4.3 for two $\langle\beta\rangle$-values. The

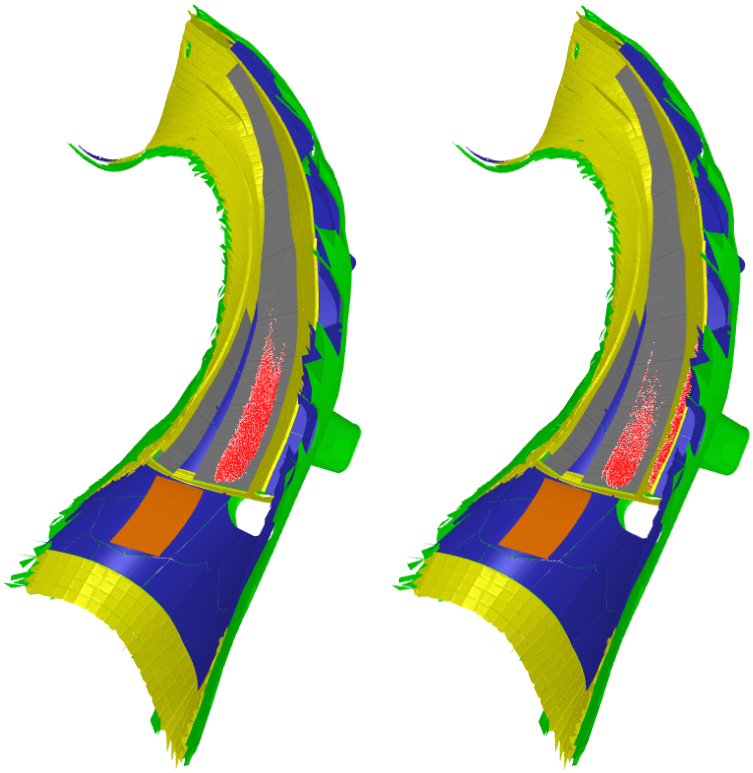

(a) 2.1 % (b) 3.2 %

Figure 4.3: *Plasma beta scan for the "low iota" configuration. $\langle\beta\rangle$-values: (a) 2.1 %. (b) 3.2 %.*

baffle plates again receive convective load for higher beta values.

The $\langle\beta\rangle$-value at which the baffle structure sees convective heat loads depends on the specific configuration and varies between 1.5 % and 4.5% . An overview is shown in figure 4.4. Critical configurations in this respect are the low shear and the outward shifted configurations. For the standard configuration, the maximum is around 2.5 % beta. An exception is the high mirror configuration, where the simulations show no overload below 4.5 % beta.

Possible solutions to increase this beta limit include the use of adjusted magnetic configurations (one scenario is described in section 4.2.1) or the modification of the divertor geometry (described in section 7.2.1).

4.2 Bootstrap current

The bootstrap current (Bootstrap current (I_{BC})) is an additional effect that is much stronger than the effects mentioned before. This current is caused by collisions between

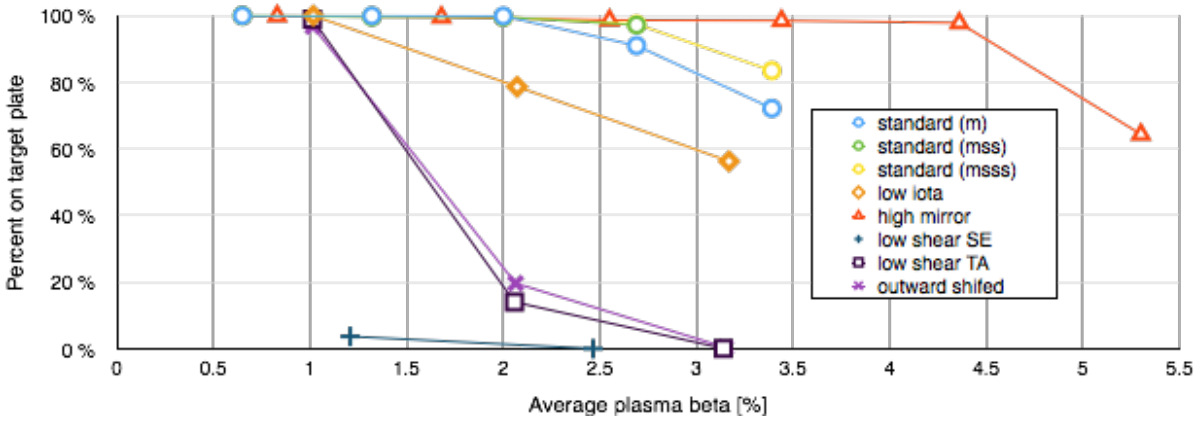

Figure 4.4: *Heat load fraction on divertor target plate for different configurations. Different VMEC domain size for standard configuration, m/mss/msss – normal/small/extra small. Proper divertor operation require that 100 % of the load is distributed to the divertor target plates.*

trapped particles and the passing particles. The resulting effect is a slowly growing toroidal current (I_{tor}). This current grows until it reaches the I_{BC}. The rate of growth is limited by the resistance of the plasma and the resulting L/R-time is on the order of tens of seconds. The value of the I_{BC} depends strongly on the magnetic configuration: I_{BC} can be low ($\sim 0\,\mathrm{kA}$) for configurations with a high mirror ratio. Configurations with a lower mirror, like the standard configuration, have a high I_{BC} ($\sim 40\,\mathrm{kA}$). Furthermore much higher I_{BC} on the order of 100 kA is possible for particular configurations under certain circumstances (heating, density, etc).

Because of the low shear of W7-X, even a small toroidal current has a large effect on the edge iota. The edge iota is in turn of extreme importance for the island divertor operation, because the divertor concept needs the island right in front of the divertor plates.

To overcome this problem, one possibility is to start with a vacuum configuration with an offset iota value $\iota_{new} = \iota + \delta\iota$, where $\delta\iota$ must be equal to the opposite value expected from I_{BC}. This approach results in the same final divertor configuration when the toroidal current is fully evolved; however, the configurations will change continuously, during the evolution of I_{tor}, potentially taking several minutes for completion [25].

4.2.1 The Scraper Element reference scenario

The Scraper Element reference scenario (SE-RS) has been developed in the past to enable the high-beta operation of a standard-like configuration [25]. The configuration

Table 4.1: *Coil currents of SE-RS.*

I_A	I_B	I_{S1}	I_{S2}	I_1	I_2	I_3	I_4	I_5
0.2473	-0.0797	0.0	0.0	1.0	0.989	1.010	1.114	1.124

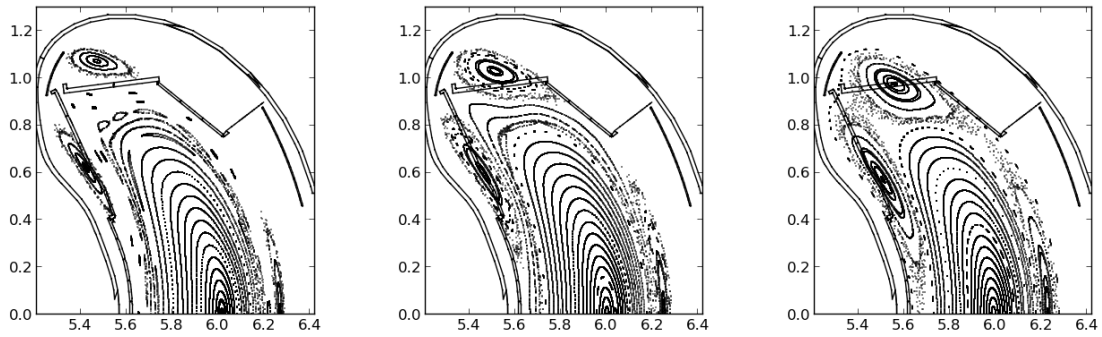

(a) 0 kA (b) 22 kA (c) 43 kA

Figure 4.5: *Poincaré plots of different stages of the SE-RS [25]. Plot at $\phi = 0°$. (a) Configuration at start of this scenario. Toroidal current is 0 kA. (b) Transitional configuration with I_{tor} = 22 kA. This configuration is the reason for the Scraper Element. (c) Final configuration with I_{tor} = 43 kA. This configuration is similar to the VRC standard.*

uses very similar coil currents settings to the VRC inward shifted (see section 2.5) (axis shift and mirror ratio). The plasma axis shift was done to compensate the Shafranov shift. The Scraper Element Reference Scenario (SE-RS) has a $\langle\beta\rangle$ of 2.7 % for 7 MW ECRH heating. The current relaxation time $\tau_{L/R}$ is 40 s, and the I_{BC} is 43 kA. To compensate for the resulting I_{tor}, the iota has been reduced by the planar coils. All coil currents are shown in table 4.1.

Figure 4.5 shows Poincaré plots of three different evolution stages of the SE-RS. At 0 kA, the scenario starts in a limiter configuration. This means that no islands are in contact with the divertor; instead, the last closed flux surface is defined by the divertor target plate. This configuration is comparable with the VRC limiter. The transitional configuration 22 kA is highly significant: the island structure is slightly cut by the divertor. The particle and heat transport follows the the island structure and passes trough the x-point, which this configuration is located directly inside the pumping gap. An overload of the divertor edge is the consequence (described in detail in chapter 5). Finally, the end configuration with I_{tor} of 43 kA is comparable with the standard configuration.

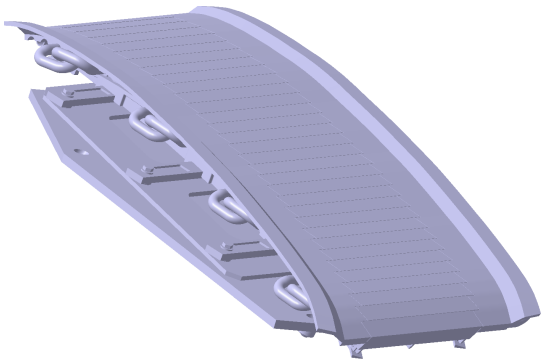

Figure 4.6: *Geometry of one HHF-SE.*

4.3 Scraper Element

The transit configuration ($I_{tor} = 22\,\mathrm{kA}$) of the SE-RS overloads the divertor target plate edge. This area (Stirnziegel/Dachziegel see section 2.3.1) can withstand only 2-5 MW of heat load.

To protect this area, an additional target element called the Scraper Element (SE) was invented. The SE is designed to protect the horizontal divertor target plate during the SE-RS. Therefore, the SE intersects the field lines that are pointing at the region of the pumping gap during the transit phase of the SE-RS [26]. The SE has the geometry of a plate that is curved in two directions; in one direction, the SE is straight. A CAD picture of the SE is shown in figure 4.6. In this picture the straight direction is the horizontal plane.

As the SE is not curved in three directions, it is not completely adjusted to the field lines of that specific configuration. This leads to a higher flexibility four using other magnet field configurations but, on the other hand, also to higher loads on the SE. The SE is located in front of each divertor unit. Therefore, there are 10 SEs in total. All SEs have the same size and geometry. The installation locations are indicated in figure 4.7.

Details of the design and the technology which allow a steady-state heat flux of $20\,MW/m^2$ can be found in the literature [27]. This is twice the heat load the divertor target plates can withstand. This SE design is named HHF-SE. The design of the SE was done using the field line diffusion approach to calculate the heat load distributions.

4.4 Conclusion on high performance operation

At time of writing two scenarios for high performance operations are known. The first is the high mirror configuration which is the optimized configuration of W7-X. The

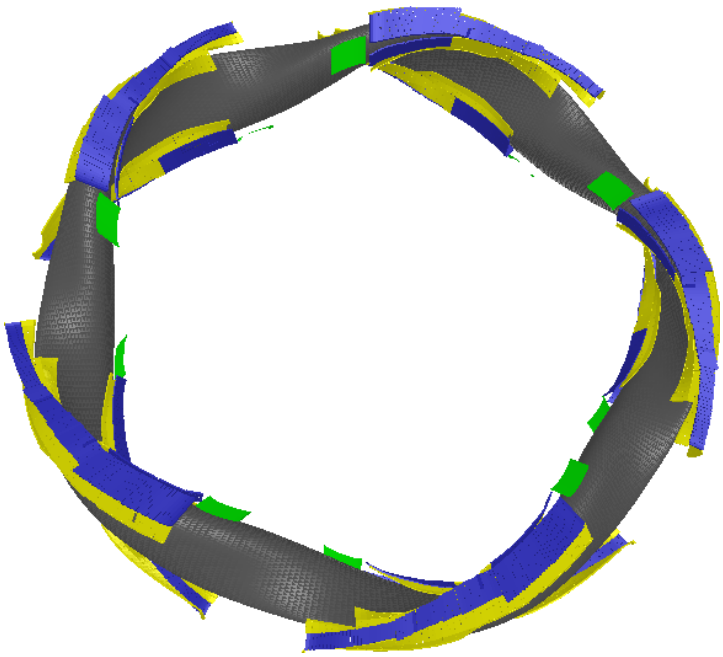

Figure 4.7: *Top view of W7-X divertor with installed HHF-SE. One Scraper Element (colored in green) is installed in front of each divertor unit.*

edge magnetic field of the high mirror configuration fit well into the divertor also for high $\langle\beta\rangle$-values, also the configuration can be operated with a low I_{BC}. The second option is the SE-RS with a magnetic configuration similar to the standard (or inward shifted) configuration. This scenario promise a higher energy confinement time but has the downside that this scenario require the SE; an additional divertor component. In the next chapter the consequences of these SEs will be analyzed in more detail.

5 Analysis of the Scraper Element

In this chapter the impact of the SE on the plasma properties is analyzed. This is the first time that detailed studies are made of how the SE effects the plasma in operation. This includes two main topics: First, the impact of the SE on the heat load distribution on the divertor and other in vessel components in order to answer the question how effective the protection effect of the SE is and at which point the SE protections fails. The second main topic is the effects of the SE on the scrape-of-layer (SOL), in particular, the effect on the neutral particles which are of importance for the pump efficiency which is again important for the density control.

The analysis is using EMC3-Eirene — a rather sophisticated fluid model [28] [29]. The is the first analyze using these code package for the SE. In addition it is one of the first calculation using EMC3-Eirene together with an W7-X equilibrium magnetic field.

The results of these EMC3-Eirene simulations confirm the protection capability of the SE but on the other hand they predict a strong reduction of the pumping capability. These reduction is caused by the fact that which a SE the neutral particle production takes place at other locations.

Furthermore, two detailed question are discussed in this chapter. The first is concerns the amount of heat load onto the baffle plates of the SE caused by radiation which is calculated in 5.5. The second is if the SE interact with the vacuum reference configurations and therefore could interfere with other experiments — discussed in section 5.6.

5.1 Simulation parameters

To understand the effect of the SE, several calculations using different parameters and geometries were performed. Three different values were used for the density at the separatrix (low: $1.0 \cdot 10^{13} cm^{-3}$, middle: $2.0 \cdot 10^{13} cm^{-3}$, high: $3.0 \cdot 10^{13} cm^{-3}$) and three values for the anomalous transport coefficient (low: $0.25\,\mathrm{m}^2/\mathrm{s}$, middle: $0.5\,\mathrm{cm}^2/\mathrm{s}$, high: $1.0\,\mathrm{m}^2/\mathrm{s}$). The anomalous heat diffusivity χ is coupled to the particle transport as $\chi_e = \chi_i = 3 \cdot D$. The heating power of 10 MW is constant for all calculations.

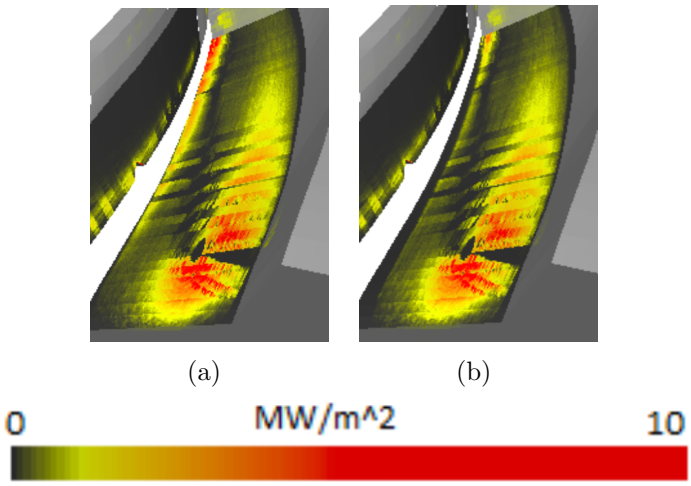

Figure 5.1: *Heat flux at divertor target plates during transitional phase (22 kA. (a) Without SE. (b) With SE. Calculated with EMC3, for 10 MW heating power.*

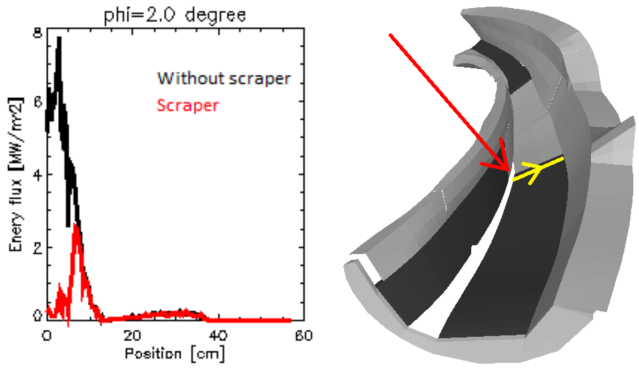

Figure 5.2: *(a) 2D plot of critical region (EMC3 Result). Transitional configuration (22 kA). Heating power 10 MW. (b) Sketch of measurement location of plot (a).*

5.2 Heat load distribution

Without the SE, the divertor edge is heavily loaded during the $I_{tor} = 22\,\mathrm{kA}$ transitional phase. The SE reduces the heat load to an acceptable amount. The heat load distributions with and without the SE are shown in figure 5.1.

Figure 5.2 shows the comparison of the heat load at the horizontal divertor plate at cylindrical angle $\phi = 2°$ with and without an SE. The heat load at the critical region is reduced by a factor of six (used range: within 5 cm of the target plate edge). From $6\,\mathrm{MW/m^2}$ to $1\,\mathrm{MW/m^2}$. Thus, EMC3 simulations confirm (compare with [30]) that the SE protects the target plate edge during the transitional phase.

For the start-up phase (0 kA) and for the final configuration (43 kA), the heat load distribution is different. Figure 5.3a shows the heat load for the 0 kA start-up phase; in this configuration, only a very small amount of flux is going to the divertor edge. Therefore, the SE is almost unloaded. Figure 5.3c shows the heat load for the 43 kA final phase. In this phase, no SE is needed for protection; nevertheless, it reduces the flux near the pumping gap. This could change the pumping capability because of the different location for neutral creation.

5.2.1 Limits of protective properties of the Scraper Element

Despite the good protection of the pumping gap, the SE does not protect other divertor parts. In figure 5.4, potentially exposed regions of the baffle plates are highlighted. These results unfortunately show that it might be impossible to run this scenario at full power, even with the SE.

5.2.2 Effect of anomalous transport

EMC3 uses an anomalous transport coefficient that describes transport effects, such as turbulence that are not explicitly simulated. For W7-X, the value of this coefficient is unknown. The often used value is $1\,m^2/s$ which has been inferred from W7-AS experiments.

Because of an absence of experimental data from W7-X, this value is only a very rough estimate. Figure 5.5 shows the effect of the strength of the anomalous transport on the strike line patterns. A larger transport coefficient leads to wider strike lines patterns. This means that the risk of overloading a divertor component will rise for a low anomalous transport. A low anomalous transport, on the other hand, means better confinement and ensures that no components far away from the plasma will be loaded.

5.2.3 Effect of plasma density

At the present time, the predicted plasma density at the separatrix has a high uncertainty. Therefore, the effects of different densities are tested. Figure 5.6 shows the strike line patterns on the divertor for different plasma densities. The plasma density has a large impact on the strike line width and, therefore, on the peak heat load. A higher density implies more collisions and, therefore, an increased diffusion; a higher diffusion leads to wider strike lines. Comparing this figure with 5.5 shows that the strike line

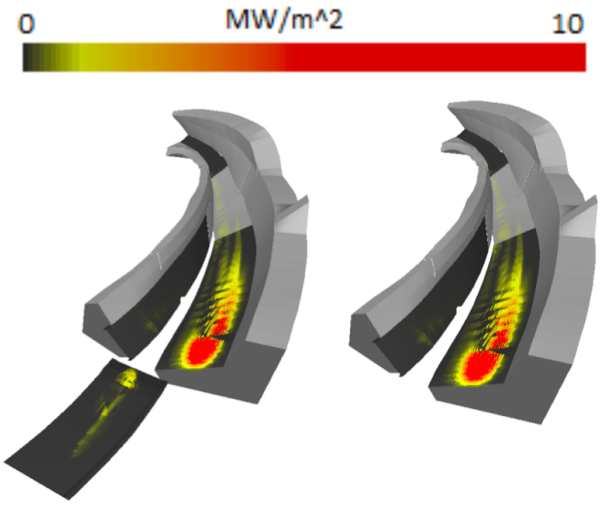

(a) 0 kA

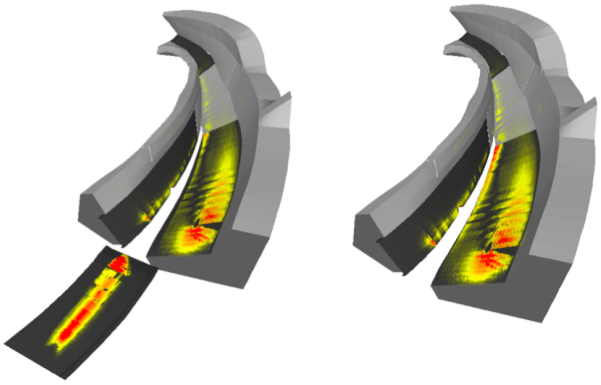

(b) 22 kA

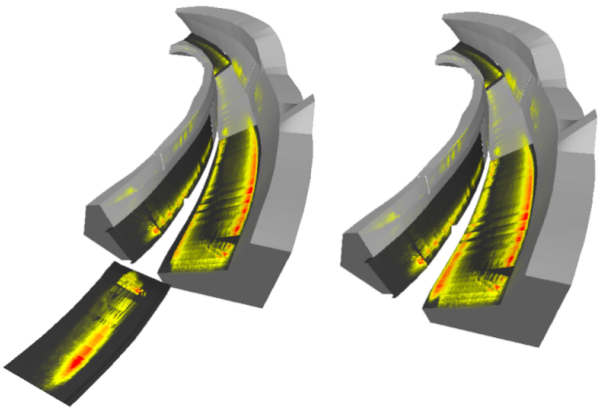

(c) 43 kA

Figure 5.3: *Evolution of toroidal current. (a) Start-up phase (0 kA). (b) Transitional phase (22 kA). (c) Final configuration (43 kA).*

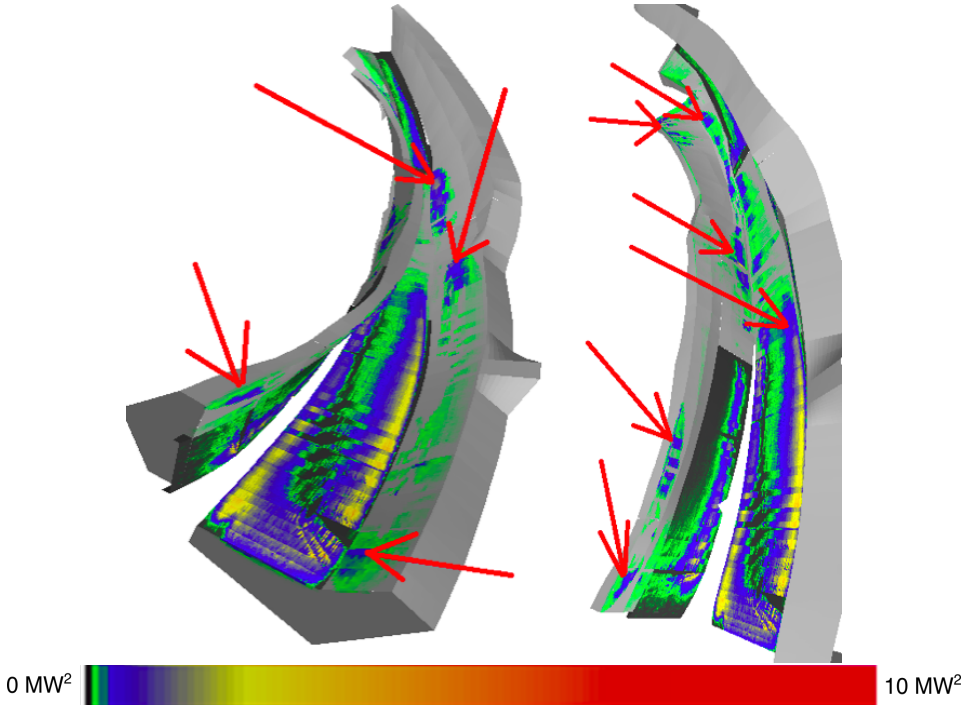

Figure 5.4: *Areas where the baffle plates will get possibly overloaded in the final configuration (43 kA). For the limits see table 2.2.*

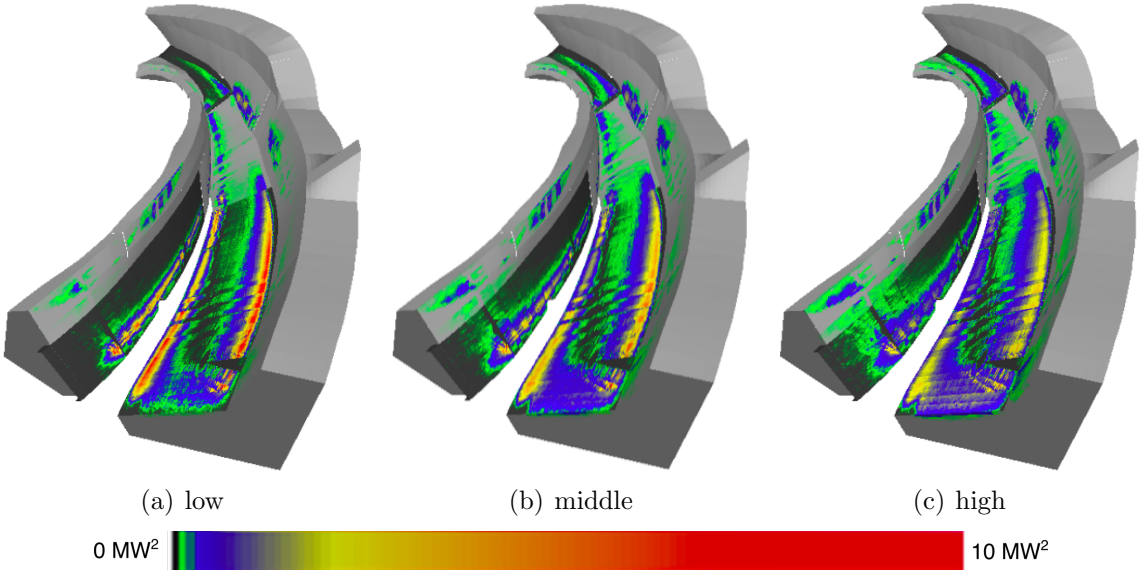

(a) low (b) middle (c) high

Figure 5.5: *Effect of anomalous transport on strike lines. Final configuration (43 kA). (a) Low anomalous transport. (b) middle anomalous transport. (c) high anomalous transport.*

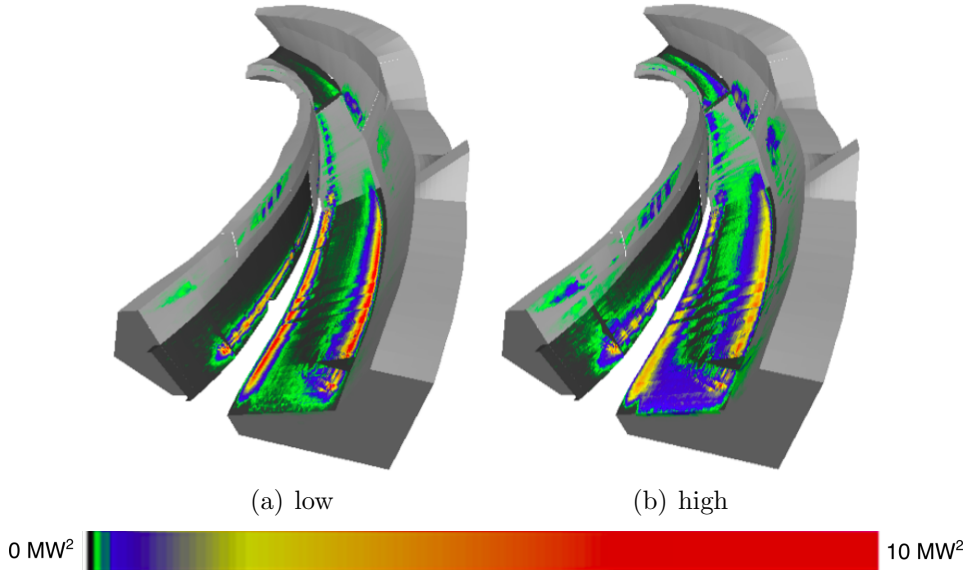

Figure 5.6: *Effect of plasma density on the strike line patterns. For the final configuration (43 kA). (a) Low density. (b) high density.*

pattern width is affected by changes in plasma density and by changes in the anomalous transport coefficient in a very similar way.

5.3 Plasma parameter

The effect of the SE on the plasma parameter (like density, electron temperature, ion temperature) are negligible. Figure 5.7 shows the electron temperature (EMC3 result), no changes caused by the SE are visible.

5.4 Neutrals

The next question to address is whether the SE affects other parameters. One concern is that the SE could negatively affect the pumping speed (pumping see section 2.3.1).

5.4.1 Total recycling flux

To address the changes in the distribution of neutrals in the divertor region caused by the SE, first the neutral creation is discussed. Ions which hit a plasma facing component recombine and form a neutral particle. The total rate of neutral particle creation per time in the whole device is called the total recycling flux. In figure 5.8a the ion flux

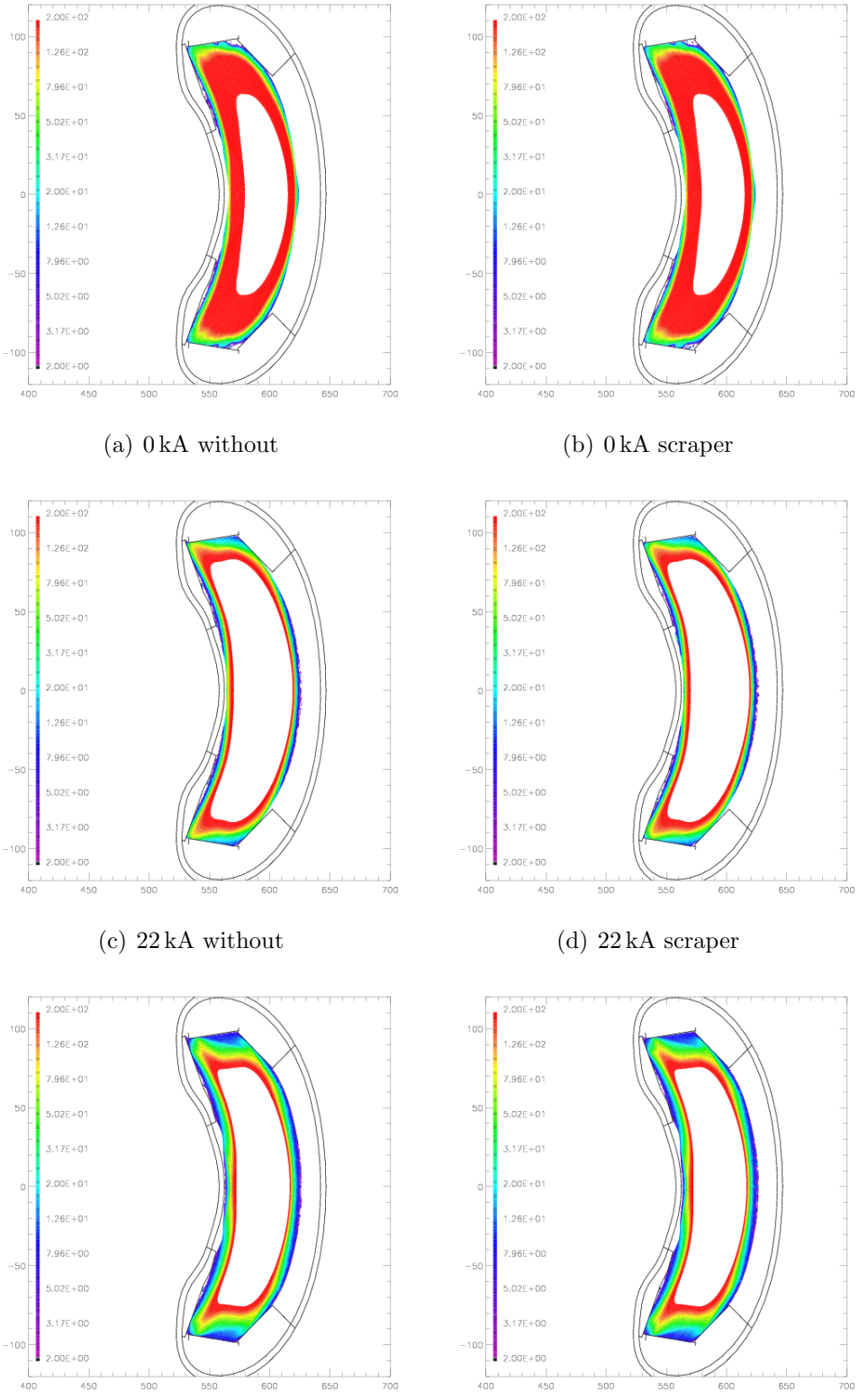

(a) 0 kA without

(b) 0 kA scraper

(c) 22 kA without

(d) 22 kA scraper

(e) 43 kA without

(f) 43 kA scraper

Figure 5.7: *Electron temperature in eV. Results of EMC3-Eirene calculation. (a) 0 kA without a SE (a) 0 kA with a SE (a) 22 kA without a SE (a) 22 kA with a SE (a) 43 kA without a SE (a) 43 kA with a SE*

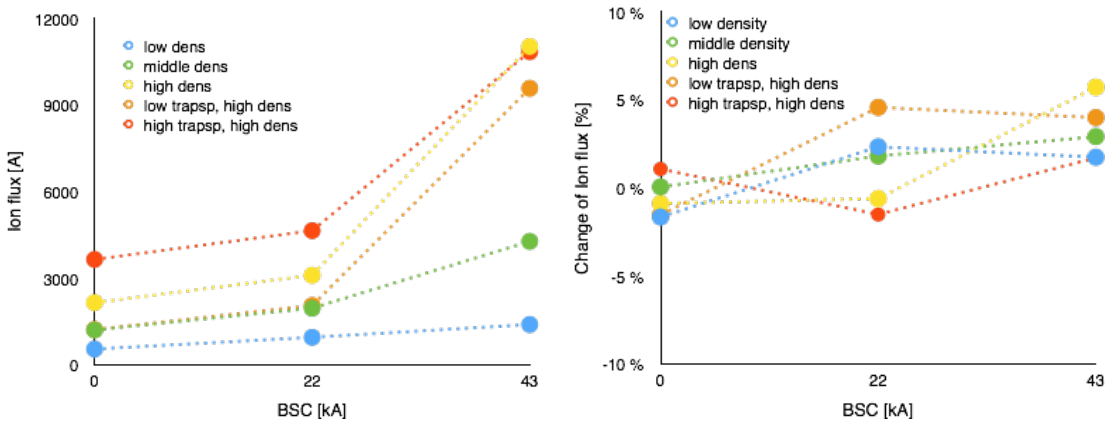

(a) (b)

Figure 5.8: *a: Total recycling flux. b: Changes of the total recycling flux due to the SE.*

calculated by EMC3-Eirene is shown with units in amperes. Therefore, to calculate the number of hydrogen atoms per second, this number has to be divided by $1.602 \cdot 10^{-19}$.

The EMC3-Eirene-calculations depend on quite a few free parameters that are usually inferred from comparisons with experimental data, which is not yet available for W7-X. To compensate for this lack of data, scans in the relevant parameters are performed and compared to each other to identify trends. The comparison between different configurations are complicated, because different configurations need a different grid for the calculation and therefore have a different computation domain. The different computation domain width is problematic because same plasma parameters for the core region are assumed (edge of the computation domain). Therefore, this uncertainty is not easy to solve while using EMC3-Eirene. Nevertheless, relative numbers can be used and comparisons between different parameters for transport and density can be made.

The total recycling flux (figure 5.8a) is higher for higher plasma densities. It is apparent that more ions lead directly to a higher rate of ions hitting the first wall. A higher anomalous transport coefficient also increases the total recycling flux which causes a higher transport perpendicular to the magnetic fields. The plasma density at the separatrix is kept constant. Therefore, it is logical that a higher transport leads to a higher flux.

Figure 5.8b shows the changes of the total recycling flux caused by the SE. Calculations with and without an SE are comparable because they use the same computing grid and the same parameters. In general, the total recycling flux will slightly increase, but the highest difference is less than 6%. This means in detail: The negative number in case

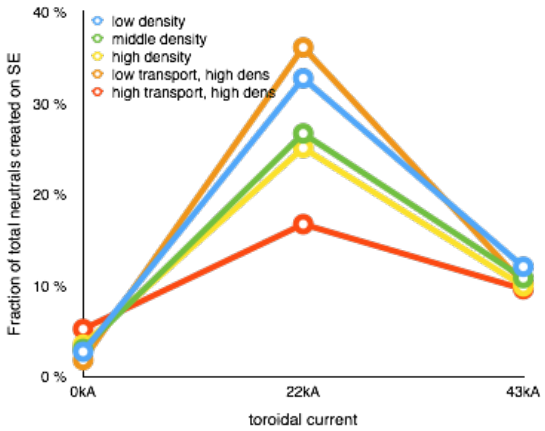

Figure 5.9: *Fraction of total neutral production which originates from the SE.*

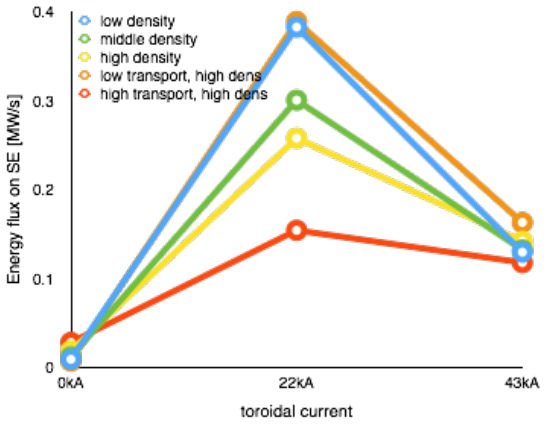

Figure 5.10: *Energy flux on SE.*

of the 0 kA (on the order of -0.5 %) are very small and caused by the finite numerical accuracy. As the SE is more or less unloaded in this configuration, the total recycling flux is not expected changed at all. For the 22 kA and 43 kA configurations, the recycling flux is slightly increased. This is probably caused by the fact that the SOL width is somewhat decreased by the SE.

As mentioned before, the recycling flux results are affected by parameters with are unknown in the real experiment and therefore will only be used here to normalize other values.

5.4.2 Scraper Element as a neutral source

In configurations where the SE is loaded, neutrals are produced on its surface. Thus, the SE is a source for neutral particles. Figure 5.9 shows the amount of neutrals created

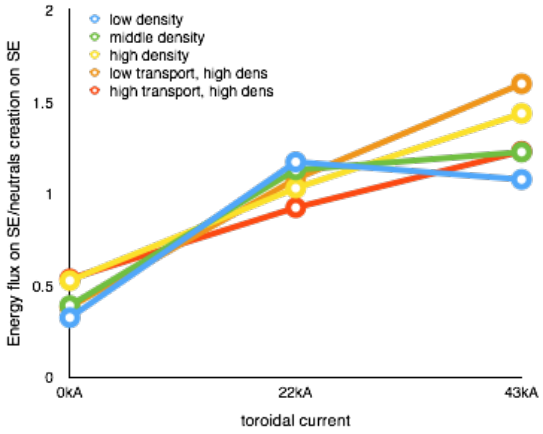

Figure 5.11: *Correlation of energy flux to the SE and neutral production at SE.*

in different configurations and for different simulation parameters.

There is a correlation between the heat load on the SE and the resulting neutral particle production. For comparison, the heat flux on the SE is shown in figure 5.10. The correlation between the heat flux on the SE and the number of neutrals created on its surface is shown in figure 5.11. The correlation of energy flux to neutral creation varies for different configurations; for a higher toroidal current, the ions hitting the SE have a higher relative energy. Especially in the 0 kA case, the ions are lower in energy. The 22 kA and 43 kA case shows a factor of around 1 for the calculation with middle and low density. For the high density calculation, in the 22 kA case this factor is about 1, and for the 43 kA it is about 1.3. This means that in the 22 kA case, the ions hitting the SE are of average speed. For the 43 kA case, they are around 30 % more energetic than the average impact speed of ions in this configuration.

5.4.3 Pumping

During OP2, two types of pumps are planned: the slower turbo pumps and the faster cryopumps. Because of their different pumping characteristics, in this simulation only the cryopumps are considered (see 2.3.1).

The pumps are simulated as a plate that has a certain probability that particles which hit it stick to it. This plate is located at the back of the horizontal divertor plate, as shown in figure 5.12.

The simulation results for the pumping speed for different parameters with and without the SE are shown in figure 5.13. Again, the absolute numbers from this calculation are meaningless because the input parameters have a high uncertainty. It can be seen

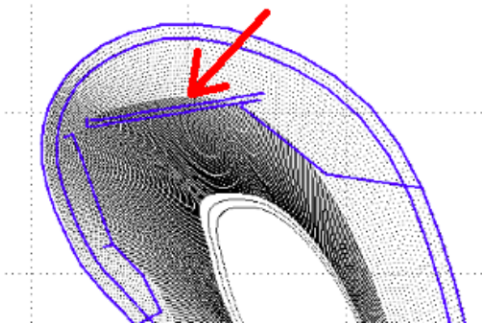

Figure 5.12: *Location of pumping plate in EMC3 pumping simulation. Blue dots: simulation grid resolution.*

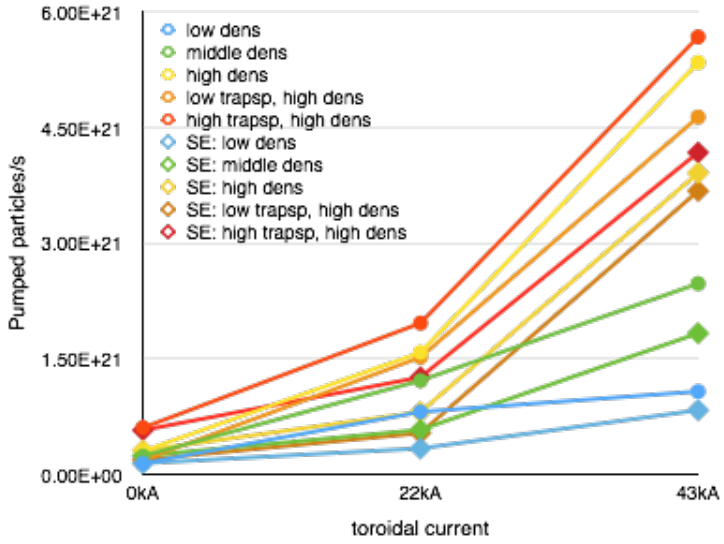

Figure 5.13: *Pumping speed for different plasma parameters and with and without the SE. Absolute numbers here have high uncertainties, but the relative trends should still hold.*

that the pumping speed increases with higher plasma densities and higher transport coefficients. This result is consistent with the one in 5.4.1 and is based on the same reasoning.

In all cases, the installation of an SE reduces the pumping speed. The reason is that a some the neutrals are created at the SE (see subsection 5.4.2) while the total recycling flux is more or less constant (see subsection 5.4.1).

The relative pumping speed reduction caused by the SE is shown in figure 5.14. On average, the pumping is reduced by 52 % in the 22 kA case and by 25 % for the 43 kA case. Especially for the 43 kA configuration this is a large value because the SE is not even necessary for this configuration.

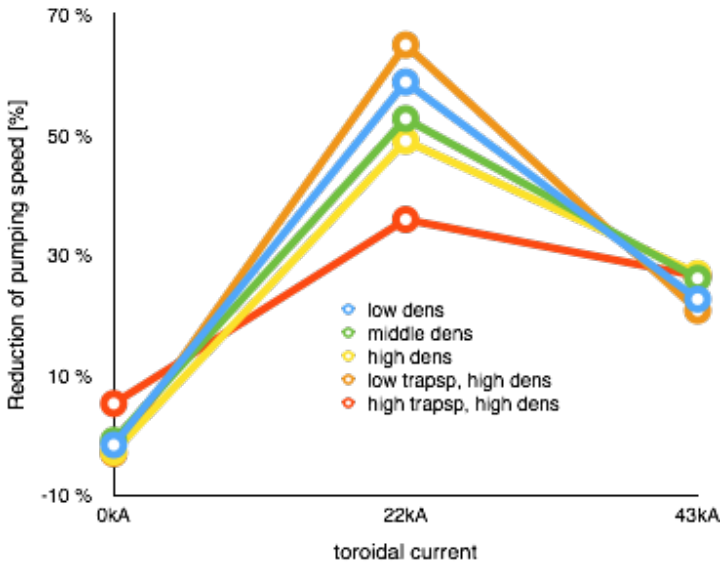

Figure 5.14: *Pumping speed reduction caused by installation of SE*

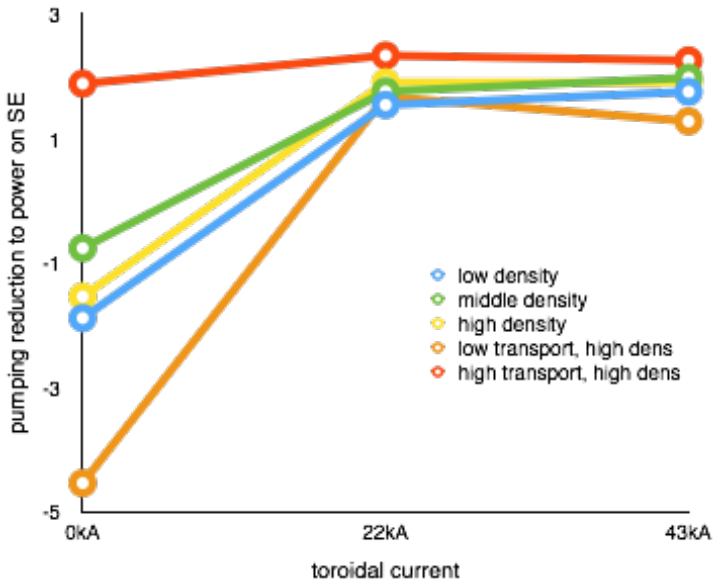

Figure 5.15: *Reduction of pumping speed in dependency to energy flux on SE.*

The correlation of the energy flux with the pumping speed reduction is shown in figure 5.15. There must be a strong correlation because the total recycling flux is constant (subsection 5.4.1), the neutral production is correlated with the energy flux (subsection 5.4.2) and the pumping efficiency will depend on the location of creation (next subsection 5.4.4). In the case of the starting configuration (0 kA) this value have low statistics (unloaded SE) and therefore a high fluctuation of factor -5 to factor 2. For the transitional (22 kA) and final (42 kA) configuration, the values are similar for all tested parameters. All values are above 1.5 and the average ratio (pumping reduction to power on SE) is 1.8. This means that when 1 % of the total load goes to the SE, the pumping speed is reduced by 1.8 %. Of course, this result is only valid in a certain range.

5.4.4 Details of pumping

The most important configuration is the final configuration (43 kA), because it will persist the entire time after the toroidal current has evolved. Therefore, only this configuration is analyzed with respect to the effects causing the pumping reduction.

The contribution of the different divertor parts to the neutral production for this configuration is shown in figure 5.16a; figure 5.16b shows only the changes caused by the SE. Most of the neutrals are produced at the horizontal divertor plate (hdiv). Only the neutral production at the lower part of this target plate (hdiv bottom) is reduced by the SE. The same amount of neutrals are instead created at the SE. The value is around 10 %, and these 10 % reduce the pumping speed by about 30%. Therefore, the SE seems to interact with a very sensitive area of the plasma.

A look into the details is needed to understand how these small changes can lead to such a big pumping reduction. Figure 5.17 shows the probability for a neutral particle created at different locations to reach the pump. When looking at the horizontal divertor target plate (hdiv), a neutral particle which is created on the half near the pumping gap has a six times higher probability as an neutral created at the upper part of the hdiv plate to reach the pump. Neutral particles which are created at the vertical divertor plate (vdiv) also have a high probability to reach the pump, but this area is not shielded by the SE.

Figure 5.18 distinguishes the pumped particles by their location of creation. With and without the SE, the most important region is the part of the horizontal divertor which is closer to the pumping gap. Without SE the main part of the particles reaching the pump originates from the horizontal target near the pumping gap, although only 18 % of the total neutrals are created there. The much higher probability to reach the pump

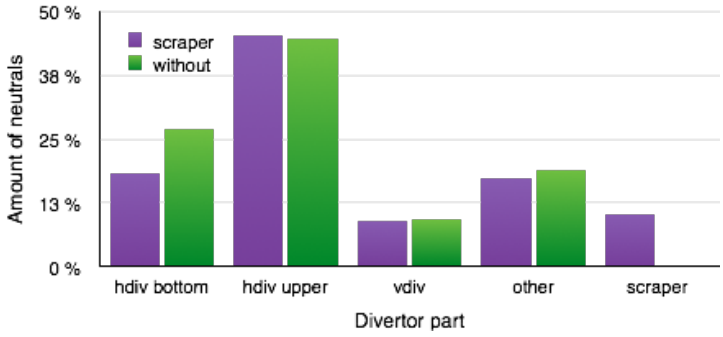

(a)

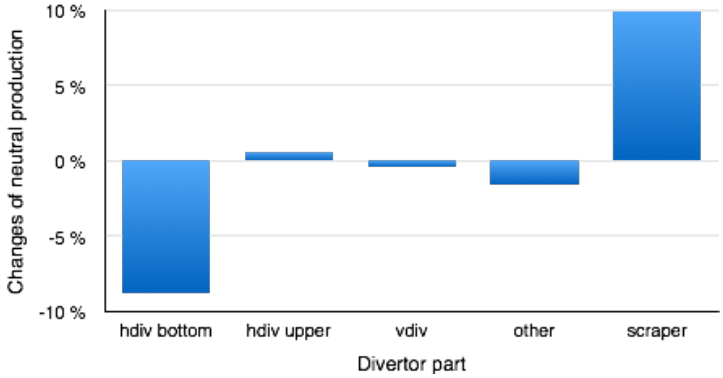

(b)

Figure 5.16: *(a) Contribution of different divertor parts to total neutral production. (b) Changes of neutral production caused by the SE. Both figures are for the 43 kA case, middle anomalous transport and middle density.*

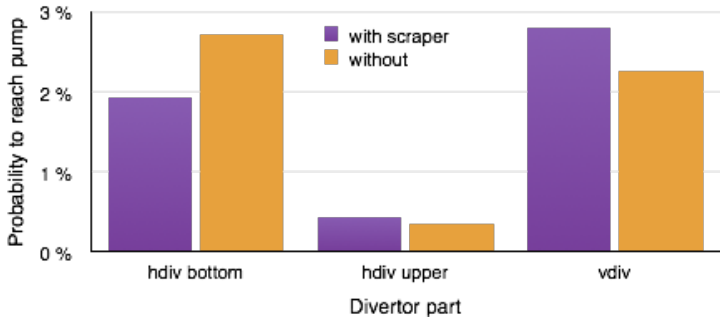

Figure 5.17: *Probability to reach the pump for neutral created at different location. For the 43 kA case, middle anomalous transport and middle density.*

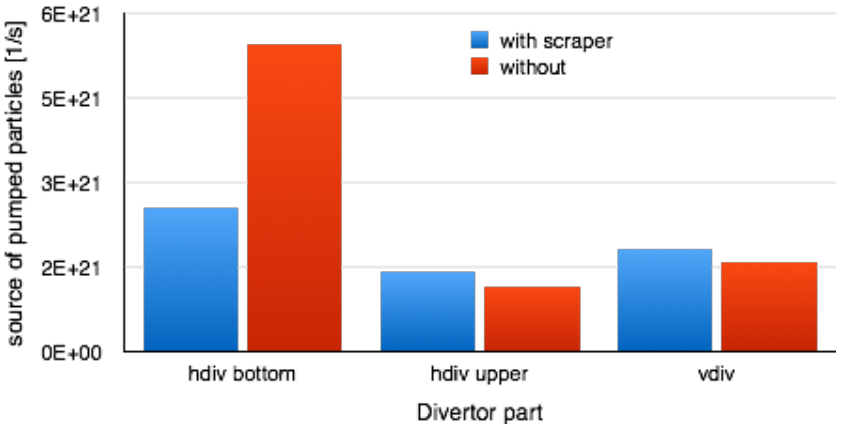

Figure 5.18: *Creation position of pumped particles. For the 43 kA case, middle anomalous transport and middle density.*

for particles generated close to the pumping gap can also be illustrated when looking at a 2D plot of the divertor and the angles which are necessary to reach the pumping gap.

5.5 Radiation load at Scraper Element baffles

One point of interest for the SE design was how the SE baffle structure must be designed so that the heat load caused by radiation can be transported away. A ray line tracing method was used in this work for the calculation. The SE baffle is maximally loaded when the plasma is detached and the full power is transferred by radiation.

In the simulation, the x-point location is used as the origin of radiation. No heat loss due to convective heat load is considered, in order to estimate an upper bound for the heat load caused by radiation.

The calculation was done as follows: First the x-point is traced. This creates a closed line after one toroidal turn. Then, random points at this line are created. The symmetry of the 5-islands configuration is used to create the other four x-point lines. The starting points are shown in figure 5.19. At each of these points rays are generated isotropically. These lines represent the emitted photons. The intersection of a ray with a plasma facing component represents the impact of one of these photons and the absorption of its energy. A radiation power of 10 MW is used.

The heat load distribution on the SE resulting from this radiation is shown in figure 5.20. A clear dependence with the distance of the radiation source to the SE can be identified. For the 0 and 22 kA case, the heat load peak at the SE baffles reaches about 100 kW. For the 43 kA case, the load is larger and reaches values on the order of 200 kW.

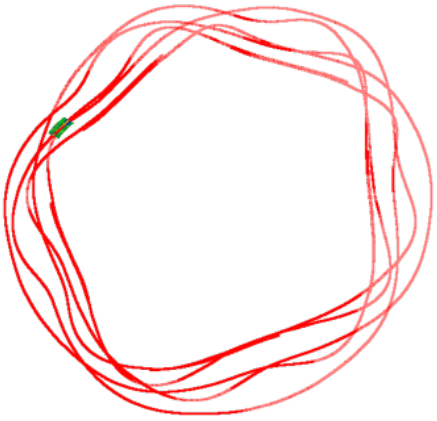

Figure 5.19: *Distribution of starting points.*

These values represent an upper bound for the radiation load.

5.6 Scraper Element with vacuum reference configurations

In order not to disturb other experiments, the SE should not interfere with the vacuum reference configurations. A field line diffusion model (described in section 3.2) was used, to test this. The results are shown in table 5.1. The maximum load is 0.045% for the high mirror case which is completely negligible.

Nevertheless, the SE will interact with configurations that load the divertor near the pumping gap. Depending on the experimental scenario this can be desirable or unwanted.

5.7 Conclusion of the Scraper Element analysis

In summary, the performed analysis with EMC3-Eirene was able to confirm the protection capability of the SE. But it turned out that the SE reduces the pumping capability more than intended even for the final stage of the SE-RS. Experiments with a real SE would favorable to test the effects on the neutral particle in the real machine. To do such tests OP1.2 is intended. Unfortunately the SE-RS is not accessible during this phase,

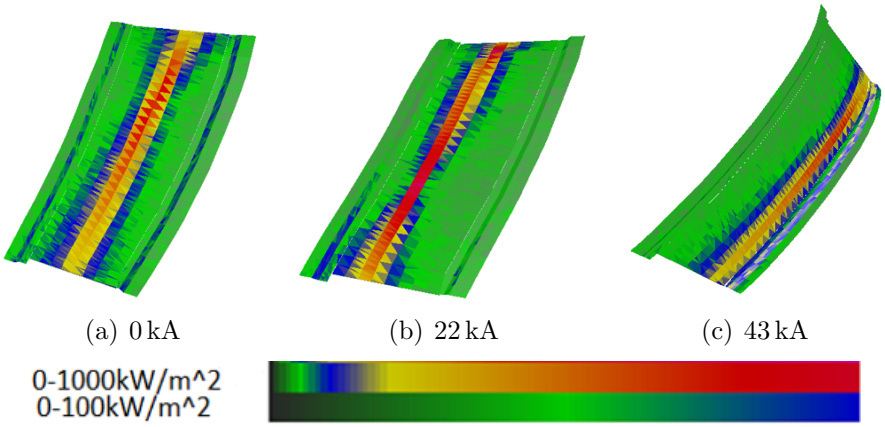

(a) 0 kA (b) 22 kA (c) 43 kA

Figure 5.20: *Load at the SE under the assumption the the full power of 10 MW are emitted uniformly at the x-points. (a) $I_{tor} = 0\,kA$. (b) $I_{tor} = 22\,kA$. (c) $I_{tor} = 43\,kA$.*

Table 5.1: *Percent of load at SE for vacuum reference configuration. Calculation with field line diffusion.*

Configuration	Fraction of total heat flux on SE [%]
Standard	0.015
Low iota	0.000
High iota	0.000
Low mirror	0.010
High mirror	0.045
Low shear	0.000
Inward shifted	0.000
Outward shifted	0.000
Limiter	0.000

because of low $\langle\beta\rangle$-value and low discharge length for evolving a toroidal current. In the next chapter strategies are suggested how to test the SE anyway while using vacuum configurations.

6 Early Scraper Element tests

Among the protection capability, the pumping reduction of the SE (described in 5) caused the need for an early SE test. Therefore, there are plans to install a Test Divertor Unit Scraper Element (TDU-SE) in the first divertor operation phase (OP1.2), when the divertor cannot be seriously damaged. The TDU-SE is planned as an uncooled component [31].

The challenge for doing these tests is that the experimental scenario for which the SE is intended is not accessible during OP1.2, i.e. the necessary beta value, the heating power and the discharge length are too long. Although the heating power used in the model scenario is available, and even if the densities (about $1.5 \cdot 10^{20} m^{-3}$) can be reached, the discharge length during OP1.2 will be too short to allow the evolution of the scenario.

Thus, producing appropriate heat loads at the SE in OP1.2 seems to be a problem at first sight. None of the VRC are loading the SE (see section 5.6). Also slight variations of the iota values of this configuration does not help.

In this chapter, a method is presented not only to produce heat loads at the SE but also to produce heat distribution and strike line patterns quite similar to those expected in the real scenarios.

These test configurations are created by using the flexibility of the magnetic coil system. The SE-RS was splitted into several time steps and for each time step the effective magnetic field was reproduced by the external magnetic field. To do this, the effect of the I_{BC} and the β-effect were treated separately and combined at the end.

These SE test configurations enable an additional operational phase for W7-X, called OP1.2b where one or two test SEs will be installed.

Additional subtopic of this chapter are the effect of reducing the number of SEs to one or two (described in section 6.4), the flexibility of the testing scenarios (described in section 6.3) and the assembly tolerances for installing a TDU-SE (see section 6.5).

Parts of this chapter were already submitted for publication [32] prior to submission of this thesis.

6.1 Approach

The approach taken here is to match the edge topology of the different stages of the evolution of the net plasma current by adjusting the coil currents. That is, the same edge magnetic topology is mimicked as closely as reasonably possible in a zero-β, zero-toroidal-current (i.e., vacuum) configuration as would exist in a high-β, finite-toroidal-current equilibrium using the flexibility provided by the main and auxiliary coil systems of W7-X [33]. Because the heat load distribution on the different divertor parts is the property of interest, the SE-RS will be assessed by a sequence of specially designed vacuum configurations which reproduce the important properties of the heat load distributions of the different stages of the SE-RS. Hence, a perfect match of the magnetic configuration in total is not the goal, but rather the reproducing of the effects of the boundary topology changes on the load distribution to the different divertor parts. Thus, a configuration with finite β and/or a net toroidal current is seen as equivalent to a vacuum configuration in this context if their relative heat load distributions on the different divertor parts are the same. A comparison of these heat load distributions will be used to calibrate the coil current changes to mimic the different plasma current effects.

There are two distinct plasma current effects on the configuration in W7-X, and they evolve on different time scales. One is due to the perpendicular diamagnetic current density $\vec{j}_\perp$ needed for the basic MHD force balance:

$$\nabla p = \vec{j}_\perp \times \vec{B} \tag{6.1}$$

Because in toroidal magnetic configurations this current is not divergence free, there is a parallel current density part connected with $\vec{j}_\perp$, the so-called Pfirsch-Schlüter (PS) current, which affects the equilibrium but does not contribute to the net toroidal current. In a tokamak, the sum of the diamagnetic and PS currents does produce a net toroidal current, but in a current-free stellarator it does not [34]. The other one, the net toroidal current, is due to the bootstrap current as well as to the induced shielding currents that appear in response to changes in the bootstrap current. The diamagnetic current and the PS current together evolve on the time scale of the changes in ∇p, i.e. on the time scale of the energy confinement time (of order 200 ms in W7-X) whereas the net toroidal current evolves on the much longer plasma self-screening time, also known as the L/R time, which will be on the order of 20–40 seconds for high-performance scenarios [35]. Currents may also be induced in conducting structures surrounding the plasma, e.g. the plasma vessel itself. These decay, however, on time scales of less than 50 ms in W7-X.

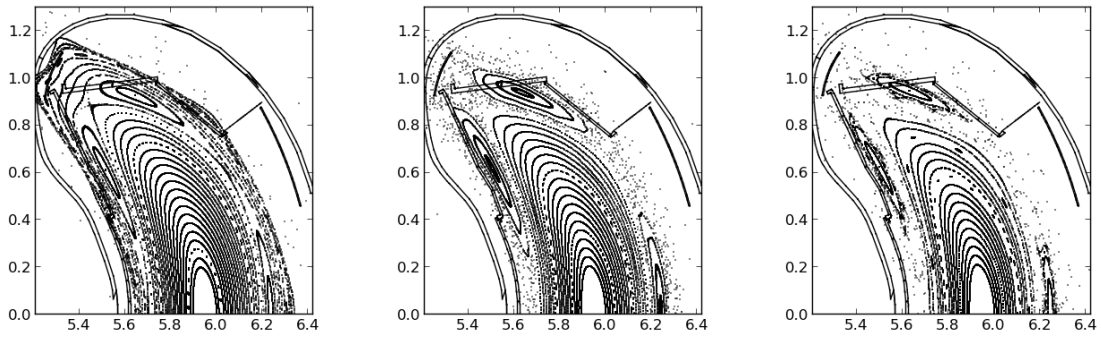

(a) $I_{s1} = 0$ (b) $I_{s1} = 0.02$ (c) $I_{s1} = -0.04$

Figure 6.1: *Sweep coil current scan (vacuum configuration). Poincaré plots at $\phi = 0°$. Vacuum magnetic fields: Modular coil currents $I_{1-5} = 1.0$, no planar coil current ($I_A = I_B = 0$) and sweep coil currents for island size variation: (a) I_{s1} = 0, I_{s1} = 0. (b) I_{s1} = -0.02, I_{s1} = 0.02. (c) I_{s1} = -0.04, I_{s1} = 0.04. Figures also used in [32].*

Thus, they will not play an important role for the slowly evolving equilibrium effects that are important for the divertor operation, and they will consequently be ignored in the following. In this work, the effects caused by the diamagnetic current and the PS current are referred to collectively as β effects. The BC and the self-shielding plasma response to it together entail the net toroidal current effects. Because of the very different time scales on which the β-effect currents and the net toroidal currents evolve, they will be assessed independently.

6.1.1 Effect of plasma beta

The diamagnetic part of the equilibrium currents is mostly poloidal and its effect on the equilibrium is therefore small since it "competes" with the mostly poloidal current of the main superconducting coils of W7-X. The PS currents generate mainly poloidal field components of the same magnitude as the vacuum field, hence with a stronger effect on the internal flux surfaces (producing axis shift and changes in the rotational transform) as well as on the structure of the magnetic field outside the plasma — i.e. the boundary islands. Figure 4.1 shows the latter effect in a sequence of Poincaré plots of magnetic fields derived from VMEC/Extender with increasing β values. Generally, the island width (radial width, not the poloidal extent given by the spacing of the x-points) increases with β; this can be best observed in the change in the upper island of the bean-shaped cross section. Furthermore, with increasing β the field around the

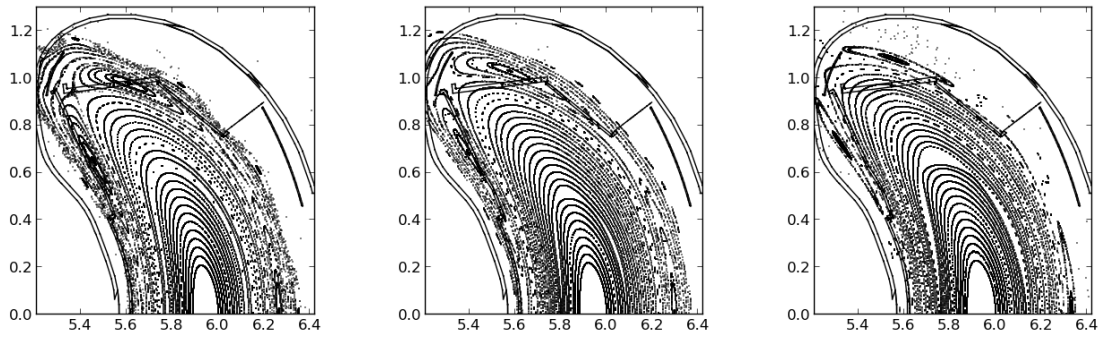

(a) $I_{A,B} = 0.12$ (b) $I_{A,B} = 0.08$ (c) $I_{A,B} = -0.04$

Figure 6.2: *Poincaré plot of iota scan (vacuum configurations) at $\phi = 0°$. Normalized modular coil currents ($I_{1-5} = 1.0$) and normalized planar coil currents (I_A, I_B) for controlling the rotational transform: (a) I_A = 0.12, I_B = 0.12. (b) I_A = 0.08, I_B = 0.08. (c) I_A = -0.04, I_B = -0.04. Figures also used in [32].*

x-points/separatrix tends to become stochastic [36],[37].

In order to mimic these β-effects, neither the 50 non-planar coils nor the 20 planar coils of the main coil system are suitable, since changing the currents in these coils tends to change many other important parameters simultaneously (rotational transform, toroidal mirror field component and/or horizontal plasma position) in addition to the island width.

However, the sweep coils, can be used in a stellarator symmetric operation mode to control the island size without substantially changing the rest of the topology. This method does not allow a perfect match to the island size at finite β, but it is sufficiently close to generate an interaction between the island chain and the plasma-facing components that is very similar to that at finite β. This suffices for many purposes, including the ability to mimic the SE-RS.

6.1.2 Net toroidal current

The optimization to a near-zero BC was done for one specific configuration in W7-X. A non-negligible BC exists for other interesting configurations and discharge scenarios. Nevertheless, the BC in W7-X is generally an order of magnitude smaller than in a tokamak or classical stellarator of similar size and rotational transform. Due to the low magnetic shear, even this rather small BC can have a significant impact on the edge islands and the island divertor operation. According to transport simulations for different

magnetic configurations achievable in W7-X, better confinement is usually accompanied by an larger bootstrap current. Thus, in order to take advantage of best-confinement configurations, a modest BC might have to be accepted with the result of a changed edge topology and in turn changed heat load patterns on the divertor (see Figure 4.2.1 and as discussed in Section 4.2.1), even if this requires the development of mitigation strategies to allow for safe divertor operation. The net toroidal current first and foremost affects the rotational transform. One of the main purposes of the 20 planar coils is to change the rotational transform ι, without strongly affecting the other properties of the equilibrium. These coils can therefore be used to mimic the effect of a net-toroidal current when none is present. The achievable match is not perfect; the changes in magnetic shear, $d\iota/d\psi$, cannot be matched while simultaneously matching the changes in ι at the plasma edge (ψ is the toroidal magnetic flux). Nevertheless, for the configurations studied here the effect due to the mismatch in shear is negligible.

Figure 6.2 shows the movement of the boundary islands with respect to the divertor when tuning the rotational transform up and down from its boundary value of 1.0 in the standard configuration (same currents in the modular coils, no other coils used), using the planar coils. Comparing this sequence with Figure 4.2.1 showing that the progression of the SE-RS as net toroidal current shows that the islands move inward in the same way.

Thus, it is possible to use vacuum configurations to mimic configurations with finite β and finite net toroidal current by adjusting the currents in the sweep coils and the planar coils.

6.1.3 Calibration

In order to be able to adjust the coil currents properly so that the vacuum or low-β configurations are equivalent in the previously mentioned definition, i.e. equivalence of heat load pattern distribution on the different divertor parts, a mapping is necessary. Thus we assess the relative heat loads on the different divertor parts (targets, baffles, SE) in a global way i.e., not the local distribution on these parts. For this, the field line diffusion approach simulating the transport perpendicular to the magnetic field [38] (as described in section 3.3) is used. In this case, though, only the heat load distribution onto the different components is considered not the shape or intensity of the strike lines. Later, in Section 6.2, a cross-check will be done by inspecting the local strike line patterns.

The coil current values given in the following have to be interpreted as relative total

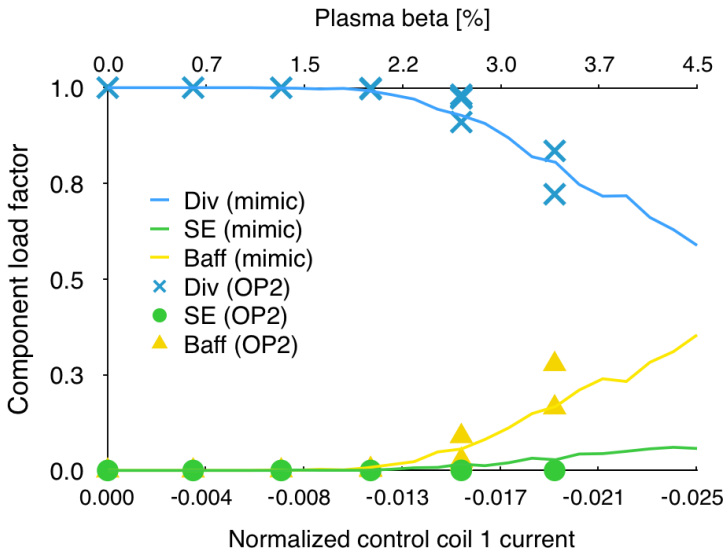

Figure 6.3: *Mimicking plasma beta effect with magnetic coils. Lines: Control coil current scan (vacuum configurations). Crosses/Circles/Triangles: MHD-equilibrium calculation for different beta values. Each equilibrium calculation was done for different values of plasma volume. Y-Axis shows relative heat load fraction of total heat load on specific component for the specific configuration. The current of control coil 2 is equal to the negative value of control coil 1. Currents modular coils = 1, planar coils current = 0. Figures also used in [32].*

currents of the respective coils, i.e., the current per winding times the number of windings of the coil with respect to a normalization current whose special value is not relevant in the current context. Thus, the so-called standard configuration has the same relative currents for the five modular coils and zero for all others. A configuration is described by the full set of relative coil current values, for all modular coils, planar coils and control coils.

Figure 6.3 compares the distribution of the heat loads on the different divertor components (including the SE) resulting from a β-sequence of MHD-equilibrium with the ones resulting from vacuum fields obtained by properly adjusting the currents in the sweep coils. As seen, the redistribution of the heat loads with β can be well reproduced by an appropriate adjustment of the sweep coil currents.

Note, that the SE-RS has a β-value of 2.7 %. The sweep coil current to imitate this β-value is used later for the OP1 mimic configurations (Coil currents in Table 6.1).

Iota calibration

Finite current in the planar coils is used in vacuum configurations to imitate the effect of the net-toroidal current. Figure 6.4 shows the change of the heat loads on the different

Table 6.1: *Coil currents to mimic the SE-RS in OP1.2. Planar coils are used to mimic the toroidal current evolution, the sweep coils for mimicking the effect of $\beta = 2.7\,\%$. The modular coil currents are the same as in the SE-RS. To achieve a main field strength of 2.5 T the normalized currents have to been multiplied by 1.47 MA.*

ID	BC	I_A	I_B	I_{s1}	I_{s2}	I_1	I_2	I_3	I_4	I_5
6	0 kA	0.220	-0.080	-0.015	0.015	0.96	0.95	0.97	1.07	1.08
11	11 kA	0.195	-0.105	-0.015	0.015	0.96	0.95	0.97	1.07	1.08
16	22 kA	0.170	-0.130	-0.015	0.015	0.96	0.95	0.97	1.07	1.08
21	32 kA	0.145	-0.155	-0.015	0.015	0.96	0.95	0.97	1.07	1.08
26	43 kA	0.120	-0.180	-0.015	0.015	0.96	0.95	0.97	1.07	1.08

components for the net-toroidal current sequence in the SE-RS as well as those for the vacuum configurations obtained by adjusting the currents of the planar coils. With an appropriate mapping of the values of the coil currents to the ones of the net-toroidal current a remarkably good match of the heat loads can be achieved (compare 6.4c). The Poincaré plots of the configurations which mimic the 0 kA, 22 kA and 43 kA cases are shown in Figure 6.5. Note that the upper island in the different cases is intersected by the horizontal divertor plates at similar positions as in the SE-RS (compare to Figure 4.5).

Both effects, β- and net-toroidal current, can be combined to simulate the expected heat load distribution of the SE-RS during the evolution in a long-pulse discharge. Table 6.1 gives the sequence of corresponding relative coil currents to reproduce the global heat load distribution on the different divertor parts with vacuum fields.

6.2 Results

Up to this point, the details of the strike-line patterns have been ignored, with the focus being on the integral power flux onto the components. However, for some locations, it is necessary that also the strike-line patterns are similar. This is especially important for the loads located near the pumping gap and the loads onto the SE, since the details of their distribution will have a strong influence on the pumping efficiency of the neutrals created on the targets by the outflow of plasma.

Figure 6.6 compares the strike line pattern of the configuration of the SE-RS with 22 kA (for which an overload at the pumping gap would be expected without the SE) with the pattern generated by the corresponding mimic vacuum configuration. Note that the shape of the pattern on the SE is very similar for the two cases, although for

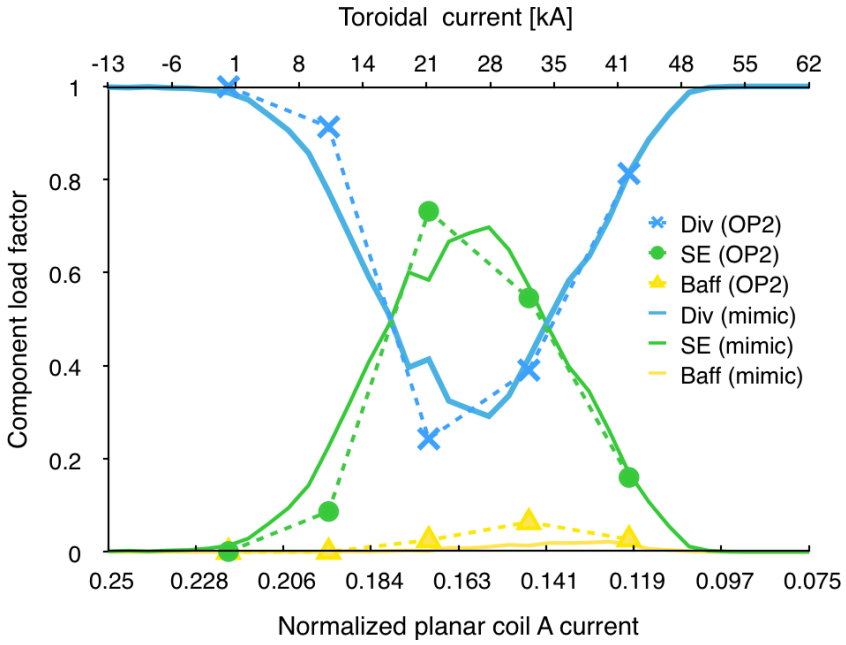

Figure 6.4: *Mimicking of the SE-RS evolution. Lines: planar coil current scan, vacuum configuration. Crosses/Circles/Triangles: MHD-equilibrium calculations with different toroidal currents for the SE-RS. Y-Axis shows relative heat load fraction of total heat load on different component on the specific configuration. Mimic configurations normalized planar coil currents:* $I_B = I_A - 0.3$. *Mimic configurations: Normalized control coil 1 = -0.015, Control coil 2 current = 0.015. Normalized modular coil currents:* $I_1 = 0.96$, $I_2 = 0.95$, $I_3 = 0.97$, $I_4 = 1.07$, $I_5 = 1.08$. *To achieve a main field of 2.5 T the normalized currents have to been multiplied by 1.47 MA. See table 6.1 for coil currents details of the mimic configuration. Image also used in [32].*

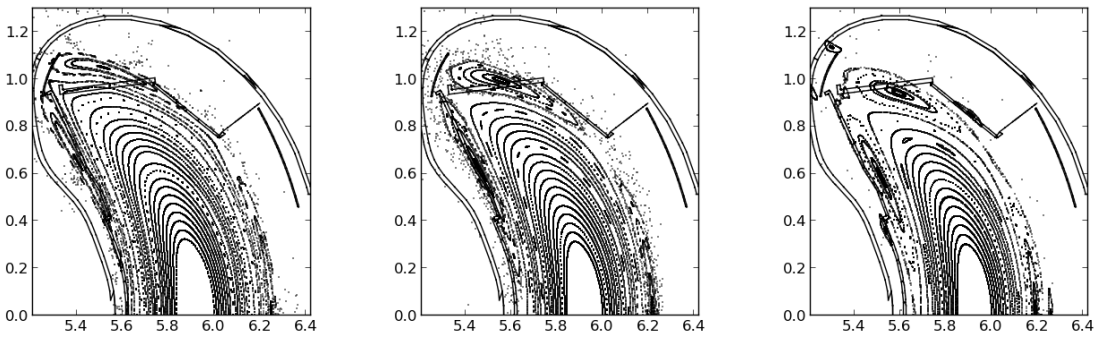

(a) mimic 0 kA (b) mimic 22 kA (c) mimic 43 kA

Figure 6.5: *Poincaré plots of vacuum fields of mimic configurations at* $\phi = 0°$. *Currents to mimic: (a) 0 kA. (b) 22 kA and (c) 43 kA. Images also used in [32].*

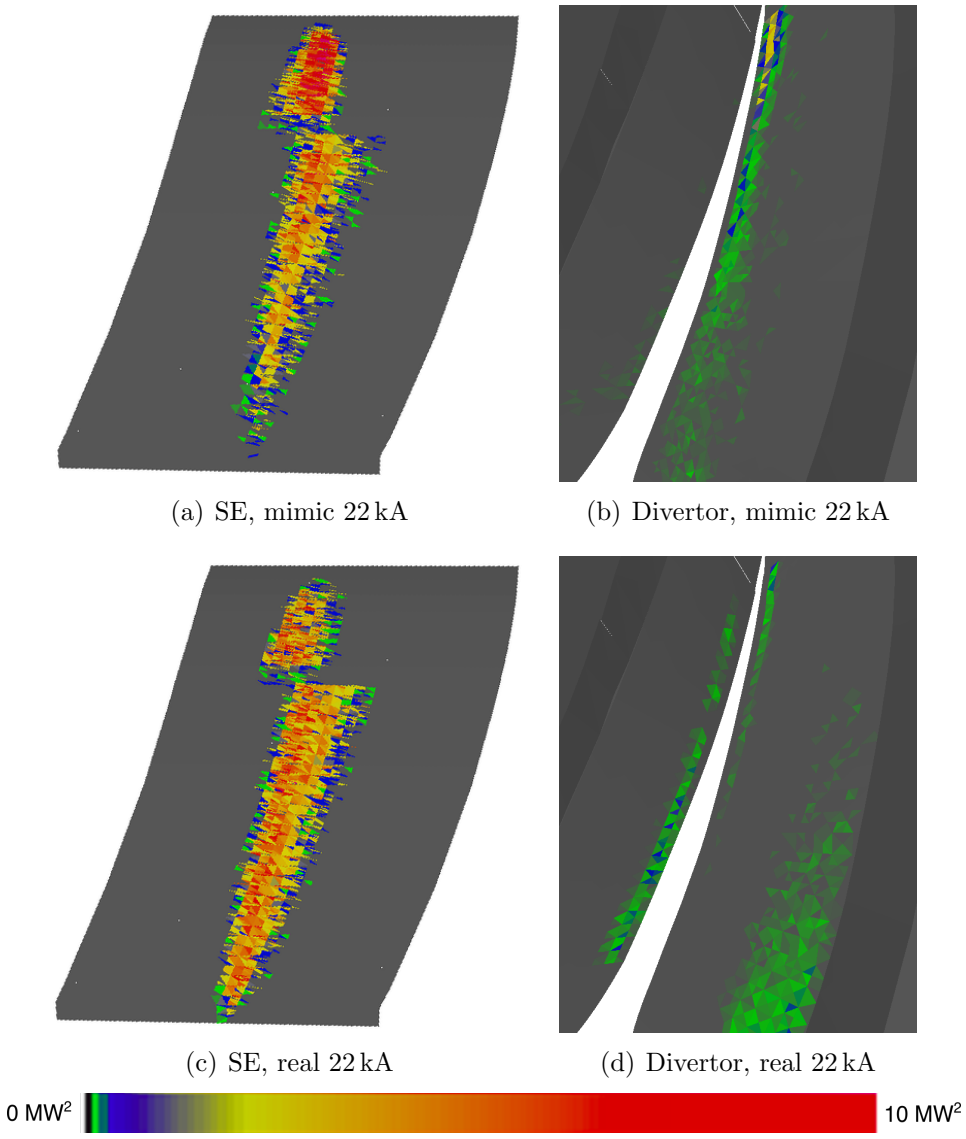

(a) SE, mimic 22 kA (b) Divertor, mimic 22 kA

(c) SE, real 22 kA (d) Divertor, real 22 kA

Figure 6.6: *Strike line patterns for the 22 kA configuration, as well as for the corresponding OP1 mimic configuration. (a) SE, mimic configuration/OP1, (b) Divertor, mimic configuration/OP1, (c) SE, SE-RS/OP2, (d) Divertor, SE-RS/OP2. Figures also used in [32].*

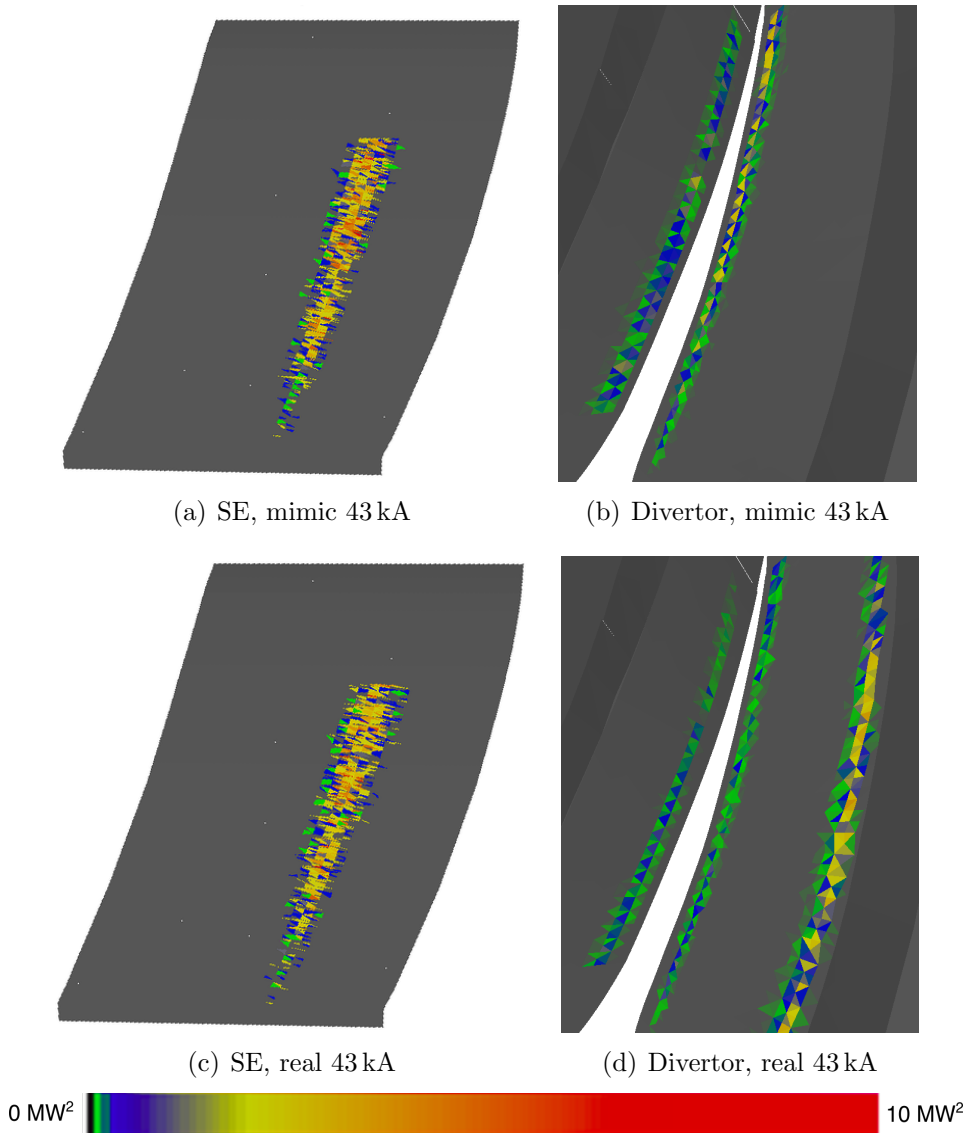

(a) SE, mimic 43 kA (b) Divertor, mimic 43 kA

(c) SE, real 43 kA (d) Divertor, real 43 kA

Figure 6.7: *Strike line patterns for the 43 kA steady state configuration, as well as for the corresponding OP1 mimic configuration. (a) SE, mimic configuration/OP1, (b) Divertor, mimic configuration/OP1, (c) SE, SE-RS/OP2, (d) Divertor, SE-RS/OP2. Figures also used in [32].*

the vacuum case, the hot-spot at the front (upper part in figure 6.6) is somewhat more intense. The heat-flux to the pumping gap is of the same level for the two configurations, but for the mimic vacuum field, the horizontal target plate (right part of TDU in 6.6) is loaded somewhat more.

The strike line pattern for the stationary configuration with 43 kA is shown in Figure 6.7 along with the corresponding mimic configuration. In this case as well, the heat flux to the SE is very similar for the two configurations. The heat load pattern of the full scenario calculation has one more strike line on the horizontal target plate than its corresponding vacuum configuration. This strike line is caused by the additional changes in the island shape due to the β-effects. With the available vacuum field coil set it was so far not possible to simultaneously provide a perfect match of the changes in the strike line patterns due to β and net-toroidal current everywhere. However, since the additional strike line is located far away from the pumping gap, its impact on the pumping efficiency is considered to be very small, so that investigations of the effect on the pumping efficiency should not be affected.

The previous shown heat load patterns are calculated with a high particle velocity to archive clean strike lines (see also 3.3). Figure 6.8 compares the resulting strike lines of a calculation with a velocity of 2000 km/s with the more physical velocity of 140 km/s. The strike line width of the calculation with 140 km/s agrees much better with the EMC3/Eirene calculations of the OP2 SE-RS (see figure 6.9. Also the small extra spot in the 43 kA case (visible in the EMC3/Eirene calculation) is visible in the 1400 km/s calculation.

6.3 Configuration flexibility

The approach described here opens up more possibilities for generating other test-configurations. Due to the limits that are set for OP1.2 with respect to the combination of discharge length and heating power, it might be useful to be able to further vary the heat load on the SE via adjustments of the magnetic configuration. This might, for example, be able to produce a heat load on the SE which or whose effects can be better assessed by the diagnostic systems. Just two examples, one for decreasing the heat load on the SE and the other with a changed magnetic mirror ratio as follows.

First, the use of the planar coils to vary the horizontal plasma position makes it possible to vary the heat load onto the SE without changing the input heating power. Figure 6.10a shows the heat loads on the different divertor parts for the mimic SE-

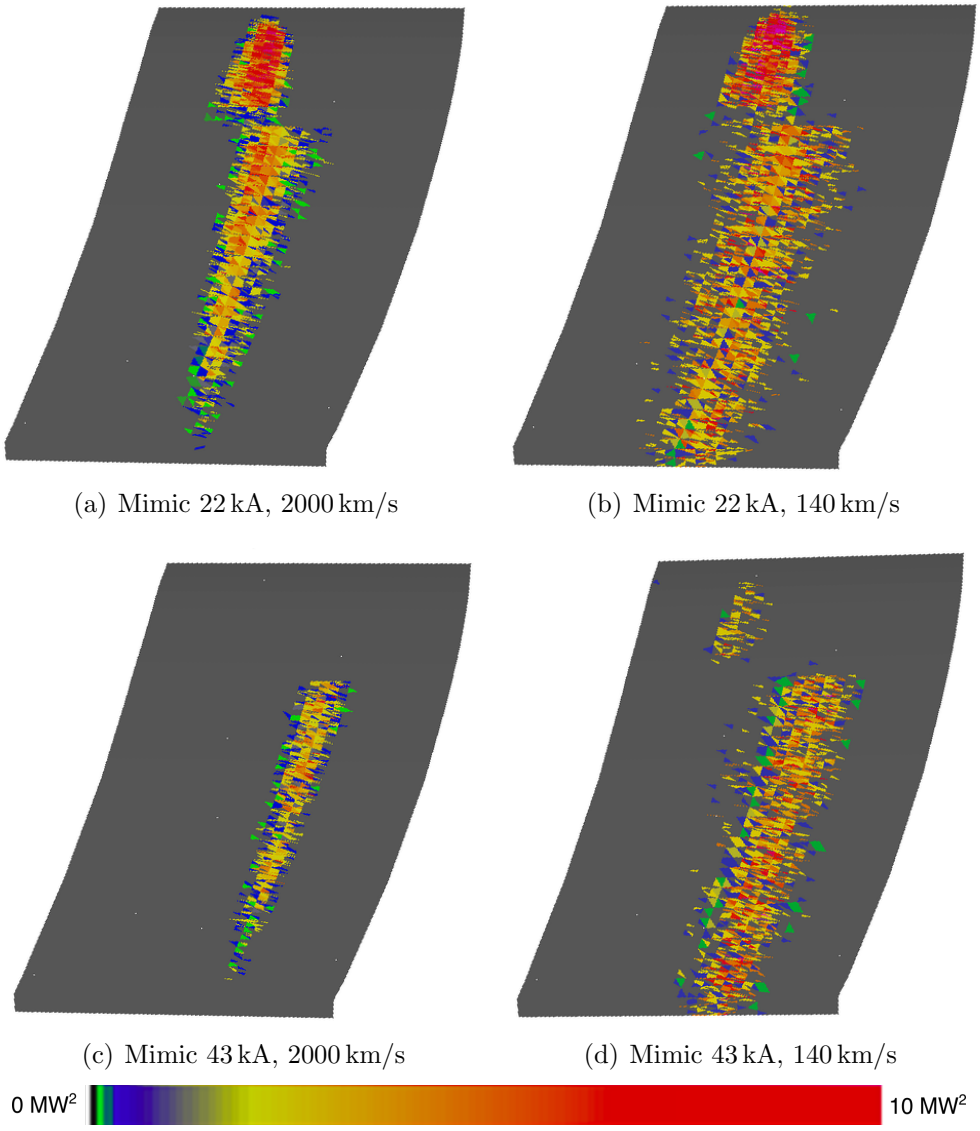

(a) Mimic 22 kA, 2000 km/s

(b) Mimic 22 kA, 140 km/s

(c) Mimic 43 kA, 2000 km/s

(d) Mimic 43 kA, 140 km/s

Figure 6.8: *Comparison of particle velocities of 2000 km/s with 140 km/s. For a heating power of 10 MW and ten SE installed. (a) SE, 22 kA, v=*$2 \cdot 10^6$ *m/s (b) SE, 22 kA, v=*$1.4 \cdot 10^5$ *m/s (c) SE, 43 kA, v=*$2 \cdot 10^6$ *m/s (d) SE, 43 kA, v=*$1.4 \cdot 10^5$ *m/s*

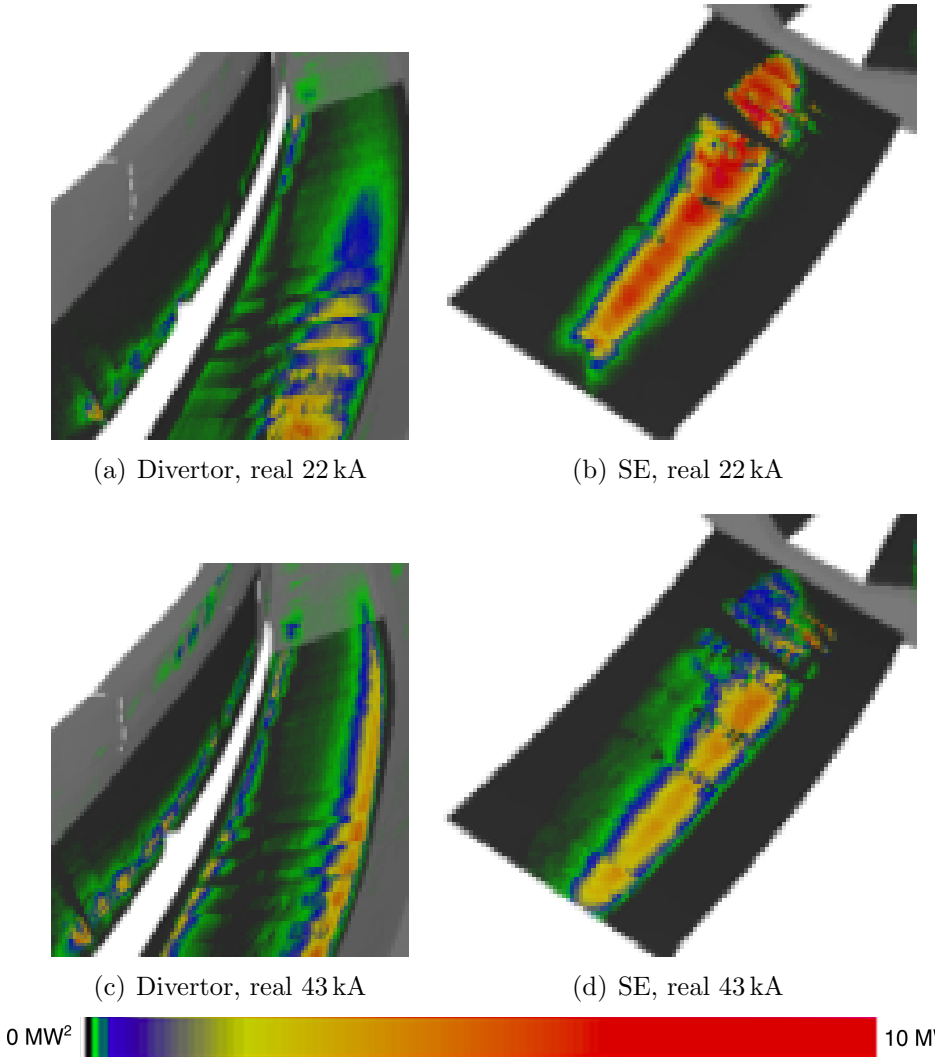

(a) Divertor, real 22 kA (b) SE, real 22 kA

(c) Divertor, real 43 kA (d) SE, real 43 kA

Figure 6.9: *EMC3-Eirene calculation of different stages of the evolution of the toroidal current. See chapter 5 for details. (a) Transit phase (22 kA), divertor gap. (b) Transit phase (22 kA), SE. (c) Final configuration (43 kA), divertor gap. (d) Final configuration (43 kA), SE.*

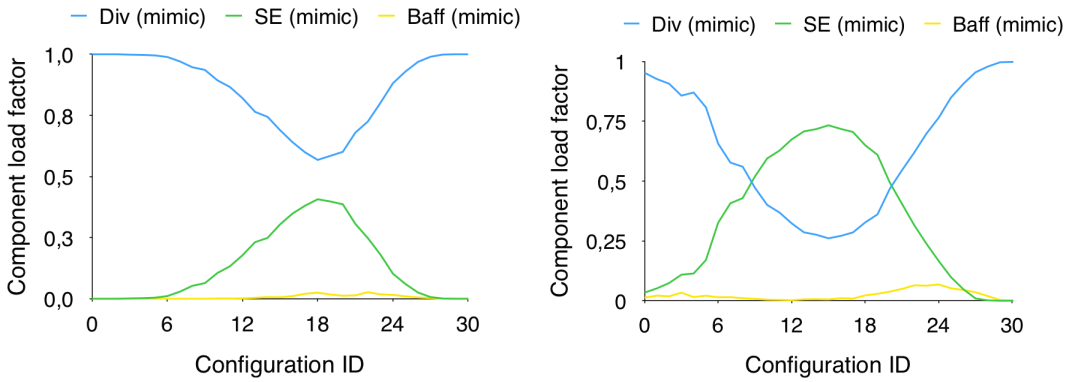

(a) reduced (b) mirror

Figure 6.10: *Alternative TDU-SE test scenarios. (a) Reduced heat flux at the SE in a less inward shifted configuration. (b) Increased heat flux at the SE for a configuration with increased mirror ratio. Images also used in [32].*

configuration being slightly shifted outward with the effect of reducing the load on the SE. This, on the other hand, means that there is a higher risk for overloading the baffle plates on the outboard side.

Second, the coil currents in the modular coils can be used to change the magnetic field strength along the axis which is usually larger at the bean-shaped planes and smaller in the planes in between. Figure 6.10b shows that by decreasing the field strength between the bean-shaped planes, i.e. increasing the mirror field, it is possible to increase the relative heat load on the SE in the same toroidal current scan as in Figure 6.10a.

6.4 Reduced number of Scraper Elements

As already pointed out, one or two TDU-SE elements will be installed after the first half of the experimental campaign OP1.2, i.e. after OP1.2a. The reduced number - the full set would require 10 SEs - is to limit the effort in manufacturing and in assembly for this first test. Although this introduces an asymmetry in the heat loads, it also offers opportunities for valuable comparisons. On the one hand, it will be possible to compare configurations and discharges without and with SEs installed (OP1.2a vs OP1.2b). On the other hand, the reduced set of SEs in OP1.2b allows a comparison of shielded and unshielded divertor units in the same discharge and configuration. However, for the latter symmetry and periodicity of the magnetic field and of the in-vessel components are crucial conditions, but this will and needs to be investigated in any case.

Later in this chapter it will be discussed how the heat load distribution changes when

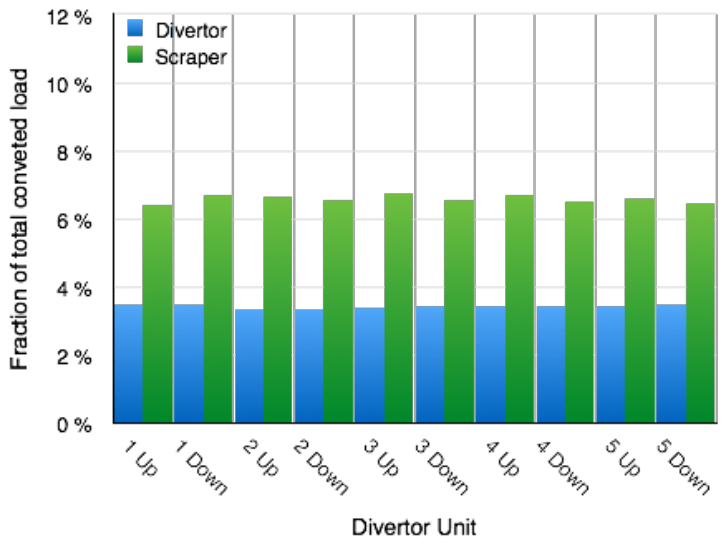

Figure 6.11: *Convective heat load distribution for ten SE installed. Mimic 22 kA configuration.*

only one or two SEs are installed. Therefore, for better understanding in figure 6.11 and figure 6.12 the convective heat load distribution is shown for ten SE installed. Both are for the mimic OP1.2b configurations and show the configurations of mimic 22 kA and mimic 43 kA of toroidal current. All SEs and all divertors receive the same amount of heat load; in the figures there are fluctuation in the order of $<1\,\%$ caused by limited statistic.

6.4.1 Two Scraper Elements

In case that two TDU-SE elements are installed, the boundary-ι value of 1 for the configurations we consider here and the argument of stellarator-symmetry suggests to install them 180° toroidally and poloidally separated from each other (one at the top, one at the bottom divertor). For configurations with a boundary-value of $\iota = 1$, these two locations are magnetically linked and will shadow each other (and their respective two divertor units). In a full installation there would be 5 (periodicity) such linked divertor and SE combinations. Thus, it is important to know how accurately such a partial installation (one or two SE) can be used to assess how the full system of ten scraper-elements will behave in later operation. This work will focus on two time points during the time evolution of the "SE reference scenario": i.e. when 22 kA of net toroidal current is reached (design point of the SE to avoid the overload of the divertor at the pumping gap) and when 43 kA of net toroidal current is reached - the steady state situation. To investigate the situation to be expected in OP1.2, the analysis is based on the two

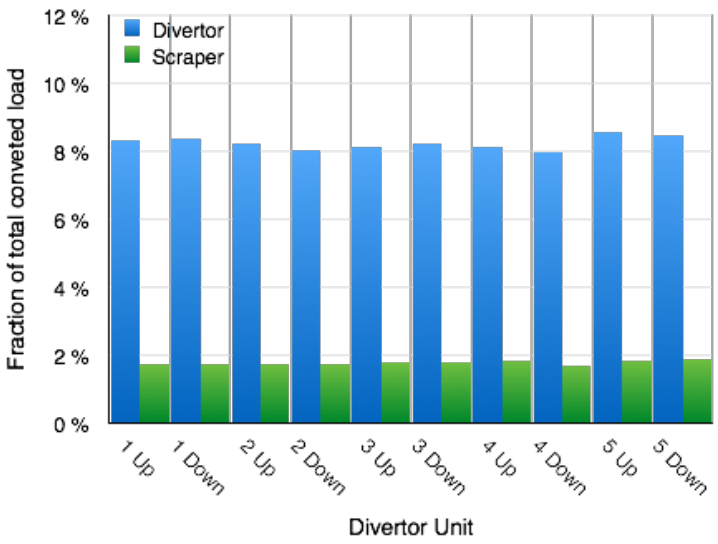

Figure 6.12: *Convective heat load distribution for ten SE installed. Mimic 43 kA configuration.*

corresponding mimic vacuum configurations. An extrapolation of the obtained results in this model to what is expected in OP2 with a full set may be nevertheless justified on the basis of the prior results, namely, that the heat load patterns and the expected pumping efficiency between the mimic configurations and their OP2 counterparts can be expected to be essentially similar. Because for the considered magnetic configurations the boundary structures have the same periodicity as the divertor units, the ones without a SE installed adjacent to them see only a negligible influence from scraper elements installed somewhere else. The heat load onto such units decreases by only 1.5 %. The two divertor units with adjacently installed SEs see a similar heat load reduction whether two or ten SEs are installed. The additional heat load reduction when going to the full set of SEs is only 10-12 % of the already reduced heat loads for the 22 kA-configuration and almost no effect is seen for the 43 kA-configuration. The results are shown in detail in Figure 6.15 and Figure 6.16.

The heat loads onto the TDU SEs themselves are, however, substantially different whether two or ten are installed. The heat load onto one of ten SE is about 35 % smaller compared with the heat load at one SE out of two. The reason for this is that the SEs do not only shield their adjacent TDU-module and their magnetically connected counterpart but also SEs in other periods. Also, the effect on the TDU-modules is always distributed onto ten modules (or eight if one considers the unshielded ones), while for the SEs the distribution of the load varies from two to ten. In addition,the strike line pattern on the SE is extended in the direction away from the divertor unit. See Figure

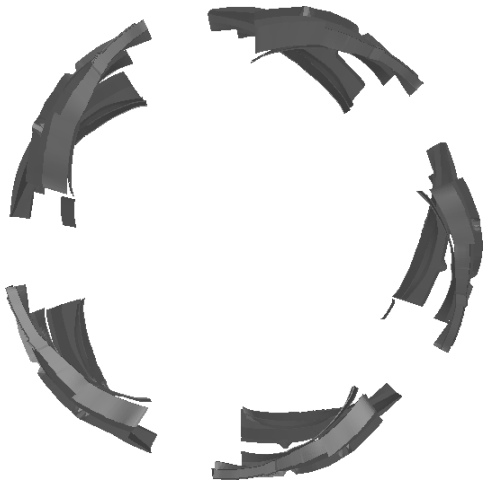

Figure 6.13: *Installation location of two SEs. Locations for the installation of two SEs. The one on the right side belongs to the bottom (lower) divertor unit, the one on the left side is attached to the upper divertor module.*

6.14.

Figure 6.9 shows a first estimation how the SE heat load could look like when only heating with 2 MW of heating power and with only two SE installed. This calculation used a particle velocity of 140 km/s and a perpendicular diffusion of $1\,m^2/s$. The calculation shows wide strike lines and a peak heat load of below $2\,\mathrm{MW/m^2}$.

6.4.2 One Scraper Element

The convective heat load distributions in case of when only one SE is installed are shown in figures 6.18 and 6.19. The SE gets the same convective heat load as with two SE installed (for example 10.05 % vs. 10.00 % for the 22 kA case). The load on the shielded divertor unit is also the same (3.86 % vs. 3.99 %). This shows that if two SEs are installed, there is no relevant interference between them. The lack of an influence can also be seen in section 6.5, in particular in figure 6.23. The maximum load fraction at the 1-down divertor unit is also unchained at $\sim 10\,\%$. In contrast, the heat load on the slightly shielded divertor units (3-down and 2-up) is changed visibly (from 7.2 % to 7.9 % and 7 % to 8.9 %, respectively).

In conclusion, the only advantage of two SEs is the higher symmetry. If two SEs are installed, each heat load situation appears twice: two identical SE heat loads, two shielded divertors, two slightly shielded and two unshielded divertor units. When considering the up/down asymmetries caused by drift effects in W7-AS, this could be a tremendous advantage when it comes to physics interpretation and diagnostic assessment.

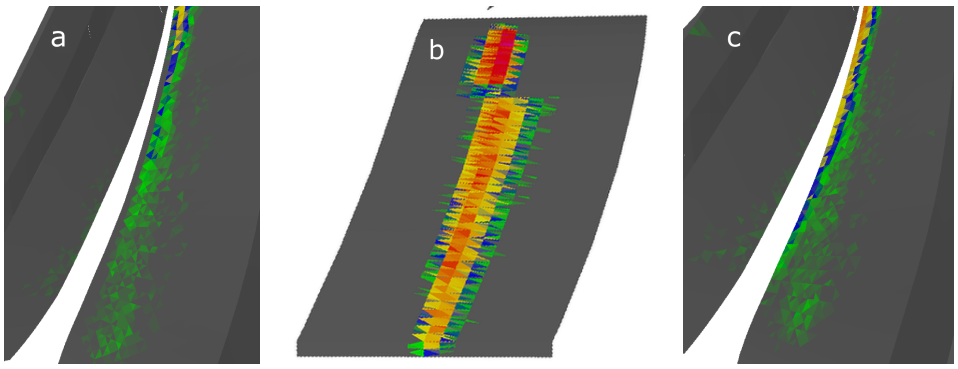

(a) gap with SE (b) SE (c) gap without SE

Figure 6.14: *22kA mimic configuration. Heat load patterns at different divertor parts with only two SE: (a) shielded pumping gap (divertor unit with adjacent SE), (b) SE, (c) unshielded pumping gap (divertor unit without adjacent SE).*

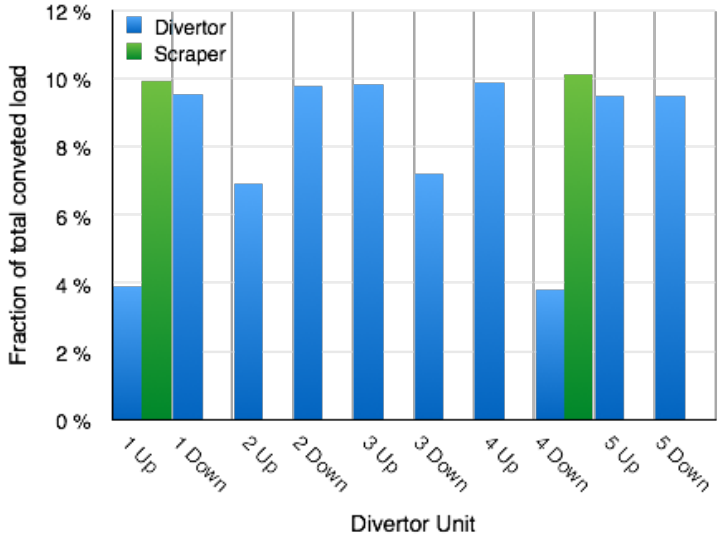

Figure 6.15: *Convective heat load distribution for only two SEs installed. Mimic 22 kA configuration.*

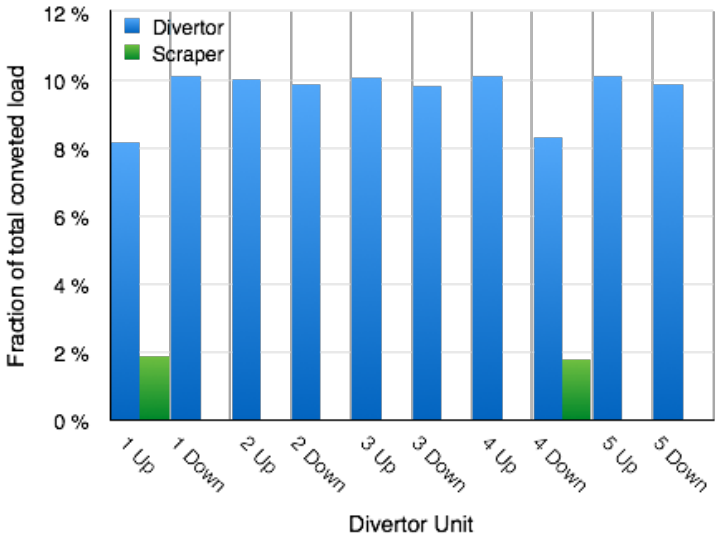

Figure 6.16: *Convective heat load distribution for only two SEs installed. Mimic 43 kA configuration.*

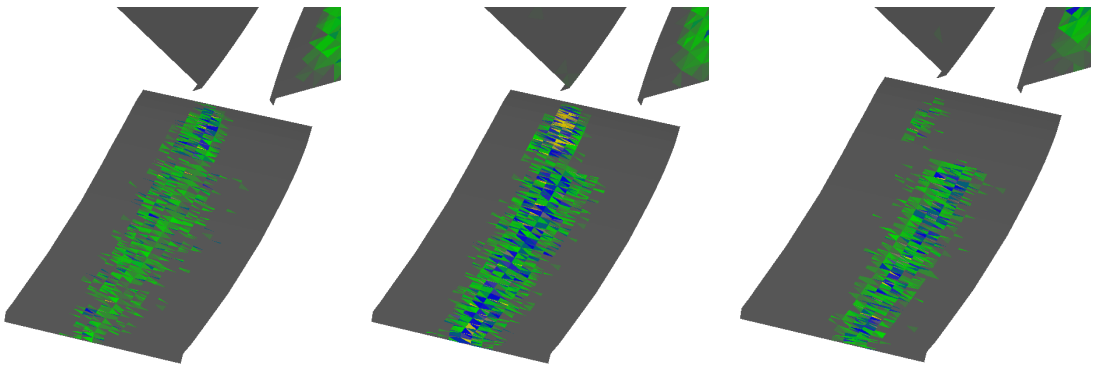

(a) SE, mimic 0 kA (b) SE, mimic 22 kA (c) SE, mimic 43 kA

Figure 6.17: *Estimation of expected heat loads in the OP1.2b test. Mimic scenario, two SE installed, heating power of 2 MW, particle velocity of 140 km/s. (a) 0 kA toroidal current. (a) 22 kA toroidal current. (a) 43 kA toroidal current.*

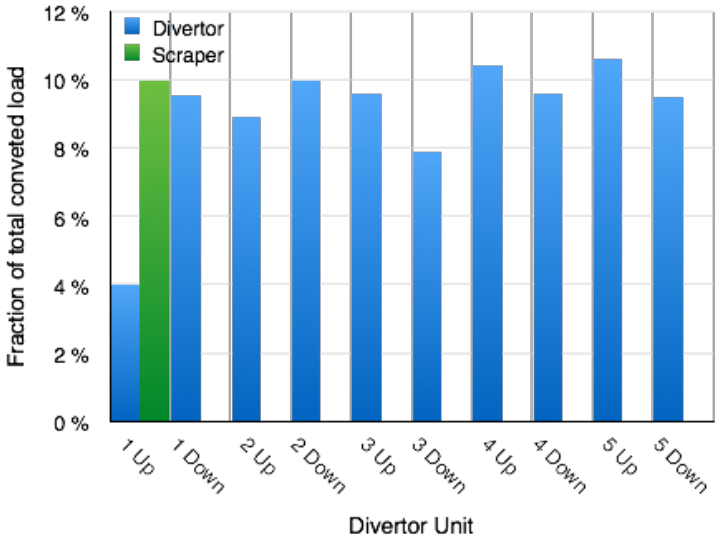

Figure 6.18: *Convective heat load distribution for only one SE installed. Mimic 22 kA configuration.*

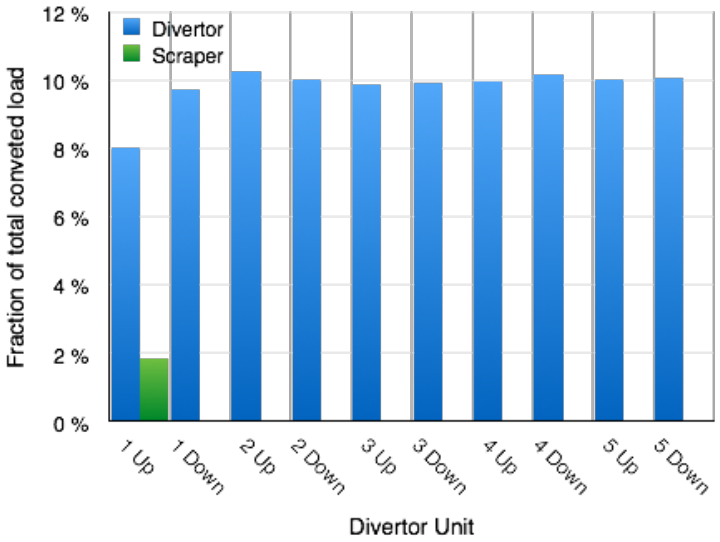

Figure 6.19: *Convective heat load distribution for only one SE installed. Mimic 43 kA configuration.*

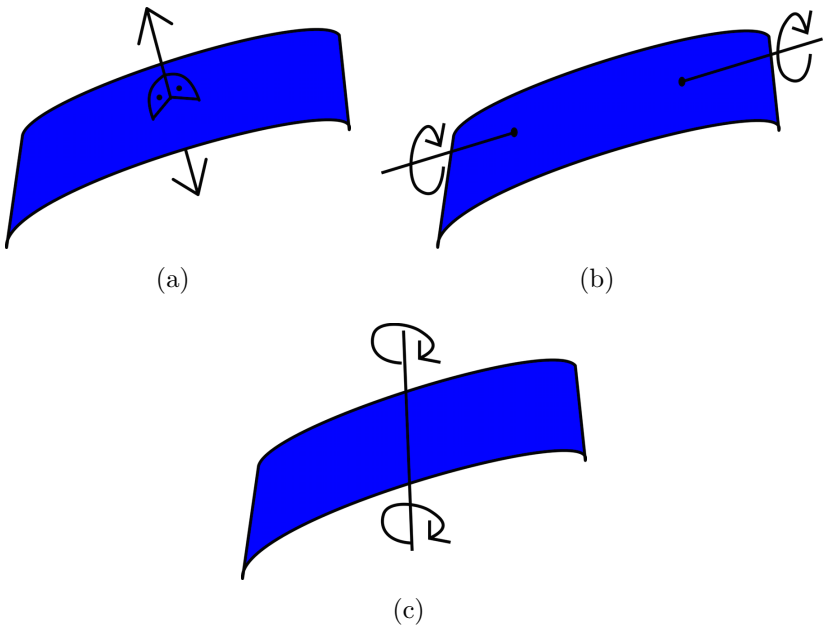

Figure 6.20: *Tested directions of TDU-SE displacement. (a) Displacement in direction of SE surface normal. (b) Rotation around long axis. (c) Rotation around short axis.*

6.5 Assembly tolerances

It was necessary to specify the installation tolerances for the TDU-SE. There are three critical possibilities for displacements, shown in figure 6.20. First a displacement in direction of the surface normal resulting in an installation closer or further away from the plasma. Second, a rotation of the SE which displaces one end closer to the plasma and the other further away. Third, a sideways tipping, bringing one side closer to the plasma than the other.

To determine a limit for the installation tolerances the OP1 mimic 22 kA configuration was used. A mimic configuration has been chosen because this configurations (not the SE-RS) will used together with the TDU-SE. The 22 kA case was selected because is shows the highest SE loading and is therefore expected to be affected most by assembly errors. In this calculation only one SE has been displaced at a time. The effect of the error at that SE, the TDU it shields (same module) and on the other SEs are evaluated.

The effect of a displacement in direction of the surface normal is shown in figure 6.21. When installing the SE closer to the plasma, the SE gets more heat load; when installing it further away it sees less load. This effect seems to be linear with a rate of change of about 3% per mm. The load at the shielded TDU is changed in the same rate anti proportional to the SE load. The SE on the other side of the torus is not significantly

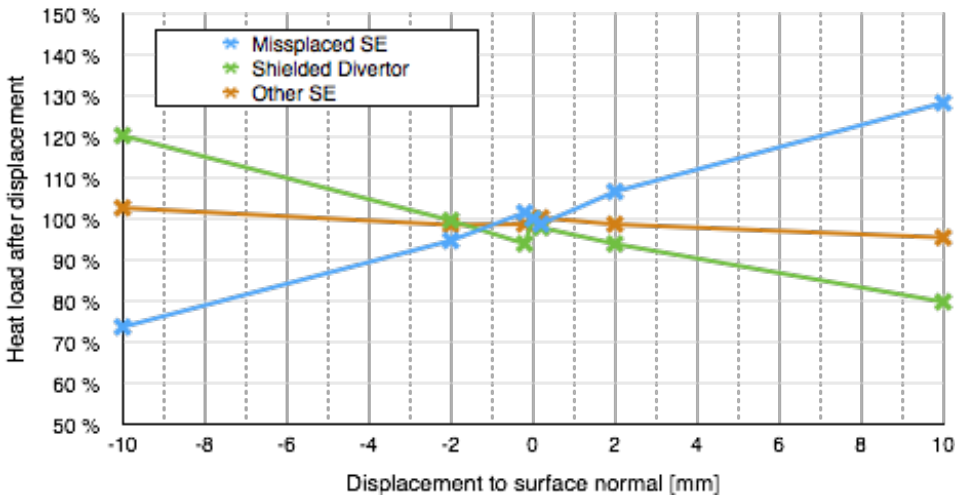

Figure 6.21: *Effect of one misplaced TDU-SE. Misplaced by an distance in direction of SE surface normal.*

affected.

The calculation of a rotation around the long axis of the SE is shown in figure 6.22. There is no clear effect visible for a maximum investigated rotation of up to 2 °.

In contrast, a rotation around the short axis has a considerable impact on the heat load distribution, shown in figure 6.23. When the front of the SE (the part closer to the TDU) is raised, the heat load on the SE increases while the heat load on the tail is decreased. The SE load is affected by roughly 15 % per 1 ° of rotation. Again, the heat load at the shielded TDU is changed in the opposite way than the SE load (10 % are missing at one calculation point and are probably distributed to the other divertor units). As before, the SE on the opposite side of the torus is not affected.

6.6 Conclusion regarding early Scraper Element tests

This work was able to show that topological changes in the edge region due to β and due to net toroidal currents can be mimicked remarkably accurately with near-zero β, near-zero bootstrap current configurations, using the existing coil set of W7-X. Specifically, effects caused by the MHD-equilibrium currents can be mimicked by adjusting the currents in the sweep coils, and effects caused by the net-toroidal current can be mimicked by adjusting the currents in the planar coils. Thus, it seems possible to experimentally investigate aspects of the interaction between plasma and divertor expected in some high-performance plasma scenarios accessible only in the later experimental phase

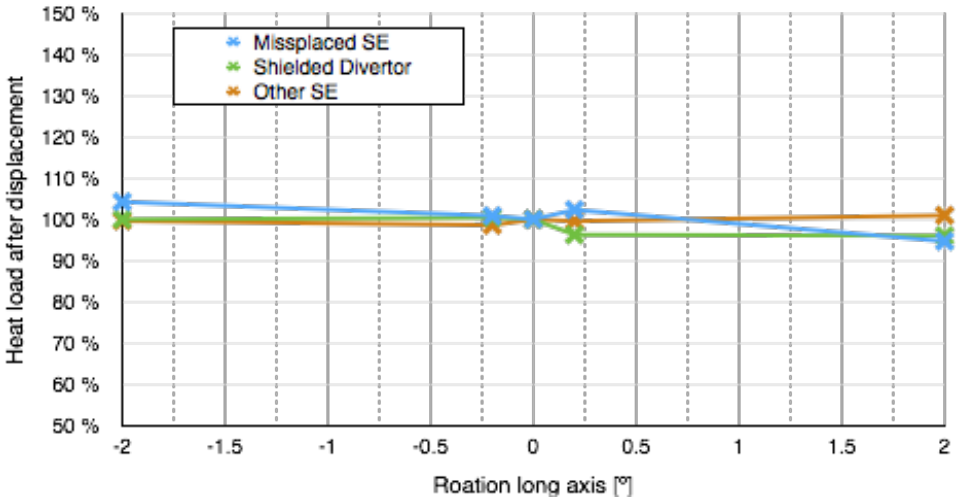

Figure 6.22: *Effect of one misplaced acTDU-SE. Displacement due to a rotation around long axis.*

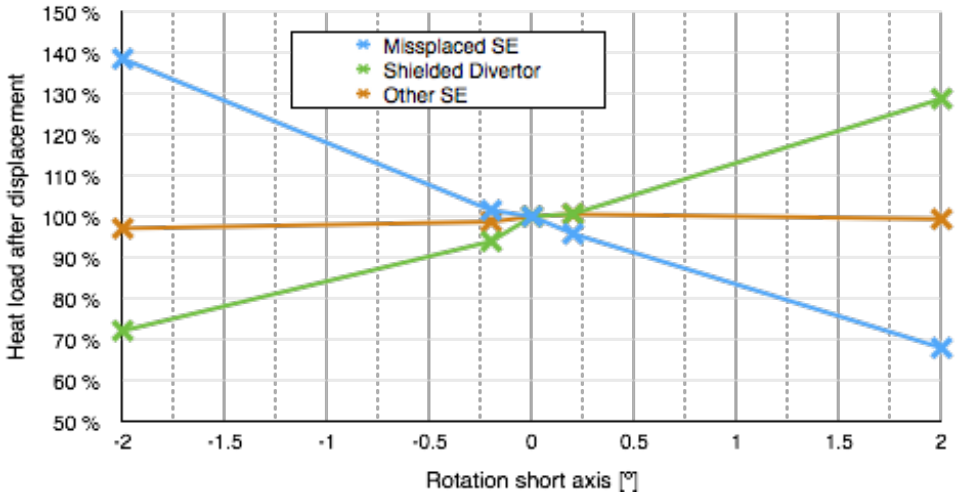

Figure 6.23: *Effect of one misplaced TDU-SE. Displacement due to a rotation around short axis.*

OP2 (2019 and beyond) already in the earlier experimental phase OP1.2 (2016/17). Moreover, this allows for an OP1.2 test program for the SEs to assess their potential advantages and disadvantages, despite them being designed to mitigate a possible divertor overload scenario that would only be interesting for quasi-steady-state operation, i.e. for very long discharges, in OP2. Most notable is that for a physics assessment of the effects of the full set of 10 SEs only a subset of two is sufficient to evaluate their effectiveness in configurations with $\iota = 1$, thus allowing for significant resource savings. Additionally, the results of such a program can broaden the basis on which a final decision on whether to manufacture and install a fully cooled SE-set during OP2. It should be noted, however, that the details of the heat load patterns will be somewhat different between a situation with ten or with two SEs. Nevertheless, their shielding effect can be assessed accurately enough experimentally and their impact on the pumping-efficiency is expected to be similar enough to be applicable for the other cases. Finally, it should be recalled that additional efforts in the scenario development are performed to explore alternatives for the SE-reference scenario avoiding the need of protective measures for the pumping gap.

These mimic configurations also enable to test alternatives to an SE already in OP1.2a, before a decision of building or not building SEs for OP2 will be made.

7 Alternatives to a Scraper Element

With test configurations for OP1.2 available (described in chapter 6) it is now also possible to test alternatives to an SE in this phase before actual needing a solution in OP2.

As one option time-depending fields are suggested as an replacing for an SE, this option is discussed in this chapter. These time-depending field scenarios use the flexibility of the coil system to produce an external magnetic field which together with the field created by the plasma currents guides the plasma on a safe path. The most promising strategy is not to work against the edge iota changes caused by the I_{BC} but instead use evolution together with a slightly radially shift of the plasma, to keep the plasma divertor interaction at the right place.

This strategy seems promising, but further investigation is necessary before experiments can be performed to answer the SE question completely.

As a sub topic section 7.2 shows how a small change in the divertor geometry could enlarge the configuration space of W7-X.

7.1 Time-dependent fields

In the design specification of the power supplies of W7-X, only slow coil current changes were intended for adjusting the magnetic field configuration, such as a iota-adjustment during a discharge. Because the planar coils (see chapter 2.2.2), which can be used for iota control, are superconducting coils, their current ramp rate is thereby limited. However, it turns out that the more immediate limit is the power supply of the planar coils (see section 7.1.3). Nevertheless, it is possible to change the coil current slowly during the discharge. This provides the opportunity to neutralize a part of the edge iota change caused by the I_{BC}. Another use of the planar coils is to shift the magnetic axis radially inwards or outwards.

To simplify matters, no plasma effects (such as plasma currents) are considered in this section. The vacuum configurations used are given in table 7.1. These configurations

Table 7.1: *Vacuum configuration sequence to mimic a divertor edge overload. Configuration is similar to the standard configuration with about 3 % beta and an evolving BSC of 40 kA.*

number	I_A	I_B	I_{S1}	I_{S2}	I_1	I_2	I_3	I_4	I_5
0	0.20	0.04	-0.015	0.015	1.0	1.0	1.0	1.0	1.0
1	0.16	0.00	-0.015	0.015	1.0	1.0	1.0	1.0	1.0
2	0.12	-0.04	-0.015	0.015	1.0	1.0	1.0	1.0	1.0
3	0.08	-0.08	-0.015	0.015	1.0	1.0	1.0	1.0	1.0
4	0.04	-0.12	-0.015	0.015	1.0	1.0	1.0	1.0	1.0

Table 7.2: *Coil currents to keep edge iota constant using the planar coils.*

	correction		currents OP1	
Number	I_A	I_B	I_A	I_B
0	-0.16	-0.16	0.04	-0.12
1	-0.12	-0.12	0.04	-0.12
2	-0.08	-0.08	0.04	-0.12
3	-0.04	-0.04	0.04	-0.12
4	0.00	0.00	0.04	-0.12

mimic an edge iota evolution using the planar coils. This evolution leads to an overload of the edge of the divertor target plate or, to a significant load on the SE (if installed). The heat load distribution caused by these configurations is shown in figure 7.1. For more details on these configurations see section 6.

7.1.1 Iota adjustment

In principle, it is possible to keep the edge iota constant during the evolution of a plasma discharge by adjusting the planar coils dynamically. This means that the coil currents must change at the speed with which the toroidal current changes. This approach leads to a constant edge iota and, therefore, to constant heat loads. This means that a configuration point can be found where the divertor load is optimized. Using the currents in table 7.2 it is possible to keep the whole load at the divertor target plate, as shown in figure 7.2a.

The rate of change for the coil currents to achieve is quite large. This will be discussed with respect to the technical limits in 7.1.3.

Table 7.3: *Dynamical magnetic field. The idea is to shift the plasma axis inwards during toroidal current evolution to protect both baffle plates and pumping gap.*

Number	I_{tor} [kA]	correction		currents OP1	
		I_A	I_B	I_A	I_B
0	0	-0.080	0.080	0.120	0.120
1	11	-0.080	0.080	0.080	0.080
2	22	-0.080	0.080	0.040	0.040
3	32	-0.063	0.063	0.017	-0.017
4	43	0.000	0.000	0.040	-0.120

7.1.2 Plasma shift

Apart from controlling the iota value, the planar coil system can be used for plasma axis positioning. This could be applied during a discharge to keep the configuration on a safe "path".

The SE-RS (described in section 4.2.1) has three stages: the safe starting point (limiter configuration) at 0 kA toroidal current, the transit phase where the SE is heavily loaded and the final stage where the divertor is properly loaded but the island structure is rather close to the baffle.

To avoid all these problems, one solution might be to start with a configuration with an outwardly shifted axis, which is not problematic at the point of zero toroidal current. In the transit phase, the strike line is far away from the pumping gap, so there should be no problem there. After the x-point has passed the critical position around the pumping gap, the planar coils would then be used to shift the plasma axis inward to avoid an overload at the baffle plate.

Using the vacuum field configuration, this strategy works well, as shown in figure 7.2b. The sequence uses static coil currents for the configuration steps 0-3 and then increases the planar coil currents to shift the plasma inwards during steps 3 to 4. The coil currents are given in table 7.3.

7.1.3 Technical limits

As mentioned earlier, the current ramp rate in the planar coils is limited. Below, an estimation of necessary coil current change for the iota control and plasma shift strategy is given.

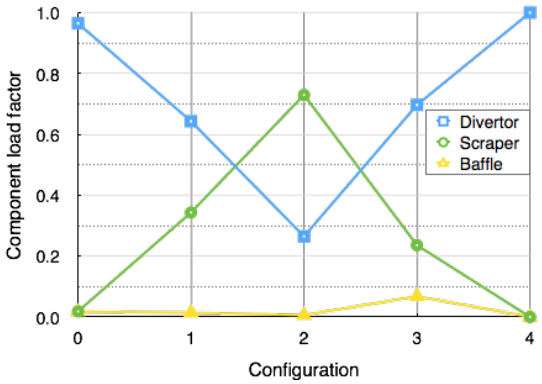

Figure 7.1: *Overload scenario. Vacuum configurations for mimic a edge iota change.*

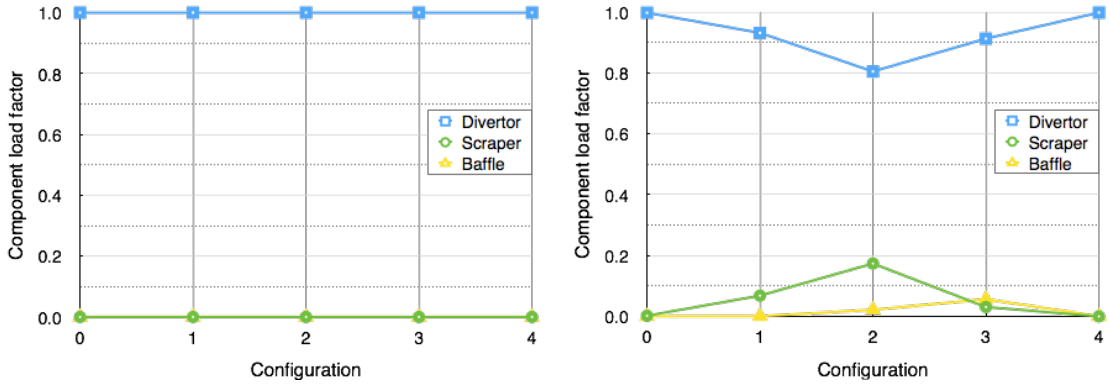

(a) Iota control (b) Plasma shift

Figure 7.2: *Protection of the divertor edge with a dynamic magnetic field configuration. SE load shows the fraction of load which load the critical divertor region. (a) Dynamic iota control. (b) Dynamic plasma shift.*

Table 7.4: *Time for evolution of toroidal current*

Number	I_{tor} [kA]	time [s]
0	0	0.00
1	11	11.82
2	22	28.67
3	32	54.53
4	42	150.44

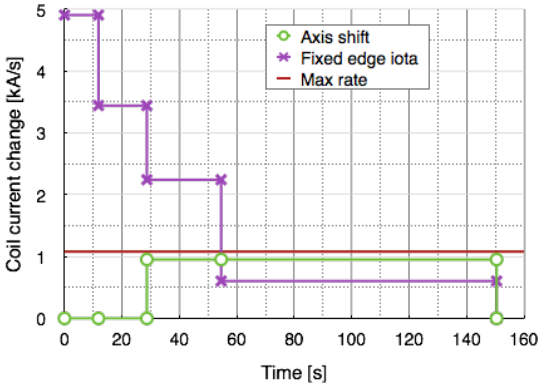

Figure 7.3: *Necessary ramp up current of the planar coils for different dynamic field configurations.*

A toroidal current (I_{tor}) evolution caused by a BSC can be estimated with:

$$I_{tor} = I_{BSC} \cdot (1 - e^{-t/\tau_{L/R})}. \tag{7.1}$$

Solving for t yields:

$$t = -\tau_{L/R} \cdot ln(1 - I_{tor}/I_{BSC}). \tag{7.2}$$

For the SE-RS the expected parameters are $I_{BSC} = 43\,\text{kA}$ and $\tau_{L/R} = 40\,\text{s}$. The times for the toroidal current evolution are given in table 7.4. To estimate the time period for the full toroidal current (which theoretically takes infinite time), the value 42 kA ($\sim$ 98 % of the full current) is used instead.

Combining the time information from table 7.4 with the coil currents from table 7.2 and 7.3 provides the rate of change of the currents necessary for the two approaches. The nominal coil current for a magnetic field of 2.5 T for this configuration is about 1.45 MA. The planar coil current change is given in figure 7.3.

In the experimental operation of W7-X, there are three things that limit the current

Table 7.5: *Coil currents for dynamic (axis shift) OP1.2 mimic scenario (scenario development is described in chapter 6)*

ID	**mimic** I_{tor}	I_A	I_B	I_{S1}	I_{S2}	I_1	I_2	I_3	I_4	I_5
0	0 kA	0.140	0.00	-0.015	0.015	0.96	0.95	0.97	1.07	1.08
1	11 kA	0.115	-0.025	-0.015	0.015	0.96	0.95	0.97	1.07	1.08
2	22 kA	0.090	-0.050	-0.015	0.015	0.96	0.95	0.97	1.07	1.08
3	32 kA	0.082	-0.092	-0.015	0.015	0.96	0.95	0.97	1.07	1.08
4	43 kA	0.120	-0.180	-0.015	0.015	0.96	0.95	0.97	1.07	1.08

change: mechanical strain, magnetic quench and the power supply. The power supply limit for the planar coils is 30 A/s per winding [39]. The planar coils have 36 windings (see section 2.2), so the maximum change per coil is 1.08 kA/s. In the end it turns out that these power supply constraint is the limiting factor and not the risk of a quench or the mechanical stability for these scenarios [40].

The plasma shift strategy remains below this limit, but the iota control strategy exceeds it by a factor of five. To reduce the correction currents by a factor of five is not an option, as it would not be enough to avoid the critical transit phase. The only possibility for using the iota control strategy is in combination with other solutions like current drive, or for long evolution times. In principle, it is possible to enlarge the toroidal current evolution time. This result in current evolution times of the order of 10 minutes.

7.1.4 Plasma shift tests

The BSC mimic configuration described in section 6 can be used to perform early tests of the dynamic field approach. The resulting coil currents, after adding the currents of the plasma shift, are shown in table 7.5. The heat load calculations seem promising for this configuration, as shown in figure 7.4. During the critical transit phase, the load is reduced by a factor of three. The maximum baffle load remains the same, because it occurs at the 43 kA configuration which is unchanged.

In summary, the strategy of shifting the plasma during operation might be a promising approach. Only small current changes are necessary to achieve a major improvement. In comparison to a SE the advantages would be: no costs, no reduced pumping, robustness (requiring only rough estimation of L/R-Time and total I_{BC}) and reactor relevance (small and simple divertor).

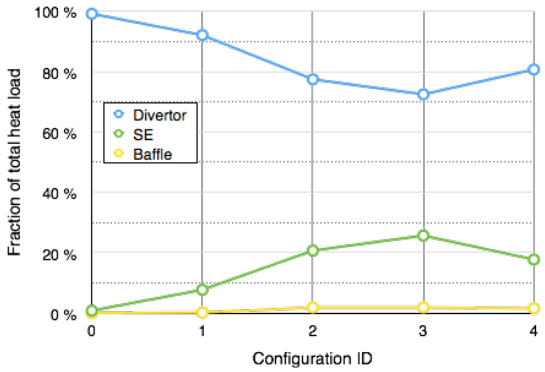

Figure 7.4: *Dynamic field test for OP1.2. Apply of plasma axis shift on BSC mimic scenario.*

Table 7.6: *Coil currents of corrected SE-RS.*

I_{tor} [kA]	I_A	I_B	I_{S1}	I_{S2}	I_1	I_2	I_3	I_4	I_5
0	0.167	0.000	0.0	0.0	1.0	0.989	1.010	1.114	1.124
11	0.167	0.000	0.0	0.0	1.0	0.989	1.010	1.114	1.124
22	0.167	0.167	0.0	0.0	1.0	0.989	1.010	1.114	1.124
32	0.184	-0.017	0.0	0.0	1.0	0.989	1.010	1.114	1.124
43	0.247	-0.080	0.0	0.0	1.0	0.989	1.010	1.114	1.124

7.1.5 Equilibrium calculations for the plasma shift approach

The first attempt to the plasma shift approach (using the dynamic coil currents calculated previously) with an equilibrium calculation (VMEC/EXTENDER) is shown in figure 7.5. Unfortunately, in this preliminary studies the baffle plates are overloaded in the 22 kA case. Further work beyond the scope of this thesis is needed to solve this.

7.2 Divertor geometry

Another option to solve the edge overload might be to adjust the divertor geometry to the plasma. This could be done either by adding one or more additional target plates to reduce the load on the vulnerable areas or by moving the vulnerable areas further away from the plasma. For non-shifted configurations (like the standard configuration), the baffle plates are the most vulnerable parts. When the plasma is shifted away from these parts, the pumping gap is left as critical area. Thus, four options can be outlined: an additional target plate in front of the baffle plates, a plate in front of the pumping gap (SE), moving the baffle plates backwards or rounding off the edges of the divertor target plates at the pumping gap.

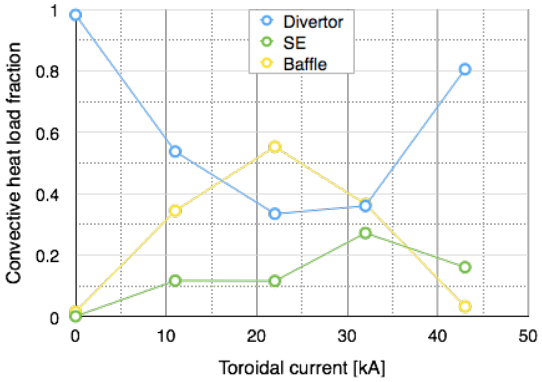

(a) Plasma shift SE-RS

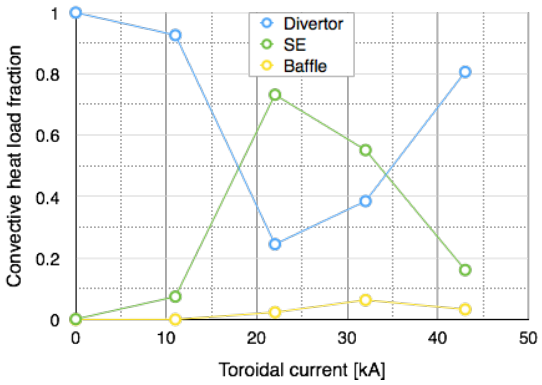

(b) SE-RS

Figure 7.5: *(a): SE-RS load distribution for comparison. (b): SE-RS with applied plasma shift correction. VMEC calculation testing dynamic coil currents. SE load shows fraction of load which load the critical divertor region. Coil currents are shown in table 7.6.*

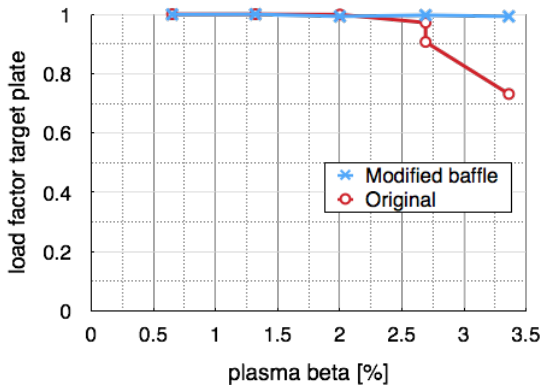

Figure 7.6: *Beta scan of standard configuration. Effect of moving baffles backwards.*

Because of the advanced stage of the SE project and the cost of target plate modification, only the option of moving the baffle plates is discussed here. All simulations regarding the SE are collected in chapter 5.

7.2.1 Baffle modification

One important divertor part is the baffle plate at the outboard side of the divertor. Relocating this part outwards (further away from the plasma) would increase the number of possible configurations. Compared to an additional target plate, this solution has two advantages. First, it does not reduce the particle flux at the horizontal and vertical target plates and thus does not reduce the pumping efficiency; this therefore helps with controlling the density. Second, the modification of the baffle would remove the necessity of a horizontal plasma position to protect the baffle from heat overload.

Figure 7.6 demonstrates the success of this idea. After moving the baffle backwards the heat load goes onto the target plate instead.

7.3 Conclusion about other protection strategies

The plasma shift approach could be an alternative to an SE but further investigation is necessary. Section 7.2.1 shows that if a new divertor is ever designed in the further, slightly more space at the outward side of the vessel position would rather be helpful to enlarge the possible configurations and protect the baffle from being overloaded.

8 Limiter plasma (OP1.1)

This chapter is concerend with investigations in connection with the development of the first operational phase, called OP1.1. Prototype-projects like Wendelstein 7-X usually have to go through reschedulings of their project plans due to various reasons. One of such revisions of the plannings led to a splitting of the operational phase OP1 into two phases OP1.1 and OP1.2. One of the arguments for the revison was to have an early plasma operation during the integral commissioning of W7-X, which is mainly concerned with measuring the precision of the magnetic system and testing and qualifying all technical systems (cryo-system, control- and data acquisition systems etc.) [41], [42].

This chapter presents two topics of this OP1.1 phase. The first topic was to find a simplified divertor geometry which was fast to realize. So different options and their pros and cons with respect to expected heat loads had been considered in the process of decision making: installation of only one half of the TDU but periodic; no TDU but use of the heat shield; and last the option of an additional temporary limiter. These questions were processed by designing adapted 3D divertor components, adapted magnetic configurations and by the prediction of the heat load distribution. In the end the limiter option was chosen.

The second topic of this chapter is the measurement of the magnetic field, in particular the 1/1 field error. To help doing so, several parameters of this field error are investigated here. The investigation shows that it is possible to detect a 1/1 field error even if the island chain is close to the magnetic axis.

8.1 In-vessel options for early plasma operation

8.1.1 Reduced number of divertor modules

One of the first ideas to shorten the preparation time so as to reduce the assembly time was a smaller number of divertor installations. Thus, the first test was to determine where the heat would go if only five divertors were installed.

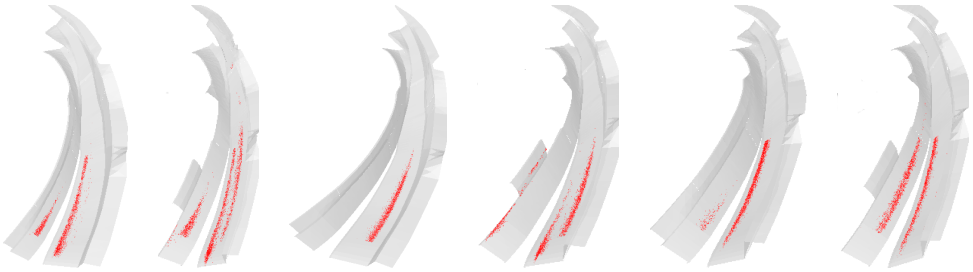

(a) 10 (b) 5 (c) 10 (d) 5 (e) 10 (f) 5

Figure 8.1: *Strike line patterns, comparing five divertors with full set of ten divertors. For reduced divertor units all 5 divertors are located at the bottom side of W7-X. Strike line positions of: (a) inward shifted (10 divertors), (b) inward shifted (5 divertors), (c) low iota (10 divertors), (d) low iota (5 divertors), (e) standard (10 divertors). (f) standard (5 divertors).*

The Simulation shows that, no other components would receive convective load, so, five divertors would be enough for reduced heating power.

The strike line positions for three of the reference configurations are shown in figure 8.1. With only five divertors, additional strike lines appear. For the inward shifted configuration, for example, there is an additional strike line in the middle of the horizontal divertor. For the low iota configuration, there are two additional strike lines: one is located near the pumping gap and the other is close to the baffle plates.

The reason for the additional strike lines originates in the fact that the islands rotate poloidally during a toroidal turn. Focusing on the standard configuration, an additional strike line appears at the vertical divertor plate (8.1(f)) Figure 2.6 shows the islands positions in the different modules. With 10 divertors, at $\phi = 0$ only the horizontal divertor is hit. Therefore, the green and the cyan colored islands are in contact with the divertor. The blue and the red ones are not in contact, because no heat goes to the vertical plate. With only 5 divertors, the green island can not be in contact because there is no plate; the first location where the green island is close to a target plate is in module 3, and there it produces the additional strike line. Therefore, the additional strike line in module 3 is caused by the missing divertor in module 1. The strike lines in module 4, 5 and 1 are caused by the missing divertor in module 2, 3 and 4.

In summary, it seems to be possible to run W7-X with a reduced number of divertors. Despite this result, it was decided that the installation of five divertors was still to time-consuming.

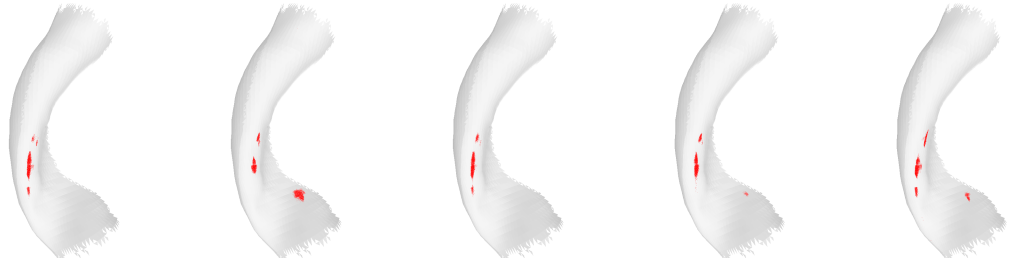

(a) (b) (c) (d) (e)

Figure 8.2: *Strike line location with an empty plasma vessel. Wall from -36to 36, z ¿ 0. Result of field line diffusion calculation without divertor units. Whole energy is distributed to the wall. Position of energy deposition depends on configuration. Configurations a-e are similar (5/5). Small hot spots; no configuration spreads energy on a wide area. (a) Standard. (b) low iota. (c) outward shifted. (d) inward shifted. (e) high mirror.*

8.1.2 Heat shield as limiter

The next idea was to spread the heat load over the plasma vessel. Figure 8.2 shows where the strike lines would be located when no divertor modules were installed inside the machine. None of the VRCs enables a wide enough spreading as to avoid an overload.

The most resistant wall area is the heat shield, which can even resist a peak heat load of $0.5\,\mathrm{MW/m^2}$ in steady state (see section 2.3.1 for details) with active water cooling. The W7-X heat shield is shown in figure 8.3. The heat shield has its widest extent in the triangular region. The plasma is thick in this region and thin in the area of the bean plate. This means that the magnetic field must be strong at the area where the divertor is located and weak at the triangular plane where the heat should go when the divertor is absent. This type of configuration is a high mirror configuration (see section 2.5).

The divertor frames (where the target plates will be located) are still part of the OP1.1 installation. These frames are sensitive to heat flux; to protect them the configuration would need to be shifted radially to connect to the heat shield and not to the divertor frame.

The configuration must also not have islands at the edge; it has to be a limiter configuration to protect the components. The best configuration found was the following: $I_{1-3} = 1.0$, $I_4 = 0.9$, $I_5 = 0.8$, $I_A = 0.25$, $I_B = 0.05$. With this, 77 % of the heat load would be directed to the heat shield, with the other 23 % going to the divertor frame cover plates. The strike point locations are shown in figure 8.4.

Ultimately, the amount of the heat load on the frame cover plates is too high.

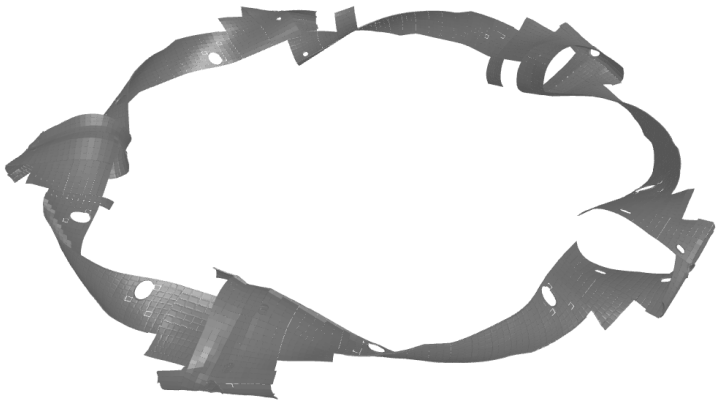

Figure 8.3: *CAD image of W7-X heat shield. Heat shield is small in bean plane (here, the divertor is located) and wide at the triangular plane.*

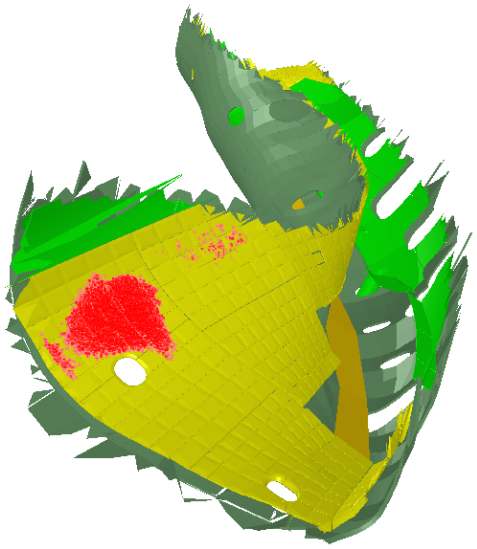

Figure 8.4: *Study of heat shield use as a limiter in OP1.1. Hit points of field line diffusion with heat shield configuration.*

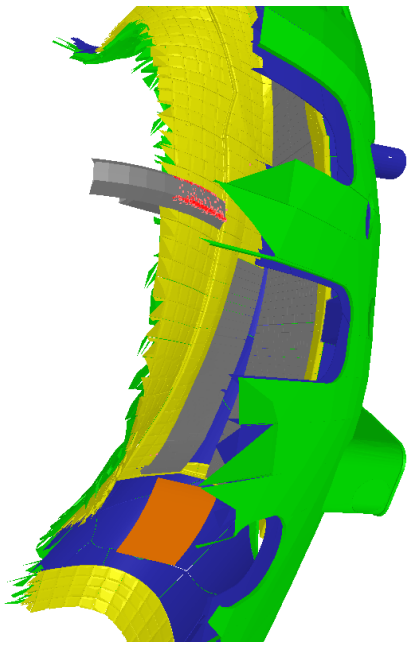

Figure 8.5: *One row of thicker heat shield tiles creates an inboard limiter. This limiter is enough to catch the whole heat load. Divertor geometry (target plates, baffles, SE) is included, showing that these areas stay unloaded.*

8.1.3 Bean plane limiter

The next possibility was to install a row of thicker heat shield tiles in one area. For geometrical reasons, $\phi = 0$ was used. This means that only 5 limiters are necessary to maintain the stellarator symmetry.

The extra heat shield tiles thickness must be in the order of 6 cm. A configuration like $I_{1-5} = 1, I_{A,B} = 0.15$ can then distribute 99 % of the total energy onto the limiter. In the end, this was the selected solution, but only preliminary work for the limiter phase was done as part of this work. The final shaping of the limiter was done by S. Bozhenkov and is described in [43].

8.2 Error field investigations

The flux surface measurement will be performed during the OP1.1 phase. One of the key points to be checked is the existence of a 1/1 field error. Such an error is caused by an asymmetrical field component and would lead to an asymmetrical heat load distribution on the divertor. Thus, there would be more heat load on two divertor module than on the other ones, and this would produce a high risk of overloading divertor or limiter

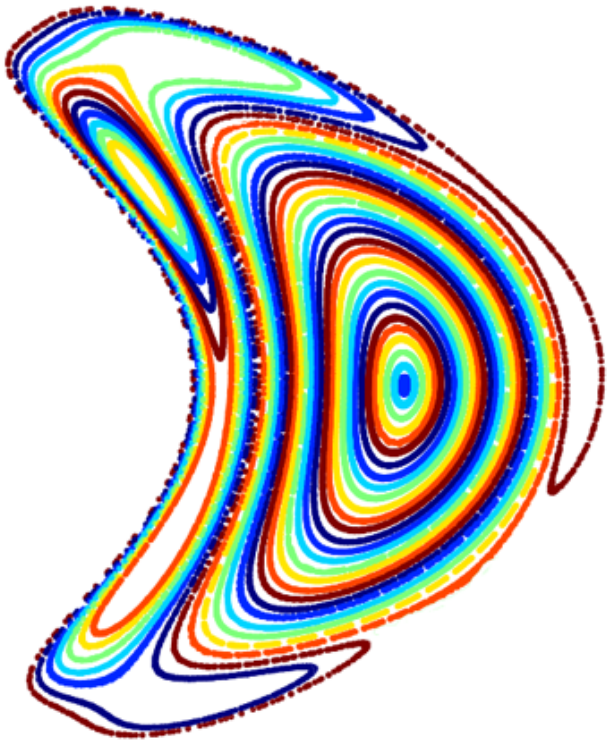

Figure 8.6: *Poincaré plot of magnetic field configuration with strong 1/1 field error. One flux tube connects the two islands on the left (orange). The second flux tube connects to an additional island and wraps up 3 in total (dark violet). The next flux tube connects to the fourth island (light green). The last one (brown) wraps up all 5 islands. Coil currents:* $I_{1-5} = 1.0, I_{A,B} = -0.12, I_T = 20\%$.

components. A Poincaré plot of the standard configuration with a strong field error is shown in figure 8.6. The islands are nested into each other.

In this section, some calculations related to the measurement of the field error in OP1.1 are described.

To speed up the analysis, a program was written within this work to measure some parameters like the island width. It was necessary to identify specific areas of interest like the center of the islands or the plasma axis in order to measure those parameters. Figure 8.7 shows the details.

The trim coils are designed to suppress (or create) such an 1/1 field error. Figure 8.8 shows the linear dependence of trim coil current on field error width.

Because of the installations inside the vessel, it is not possible to look at the whole island structure with the standard configuration. Therefore, the iota value must be

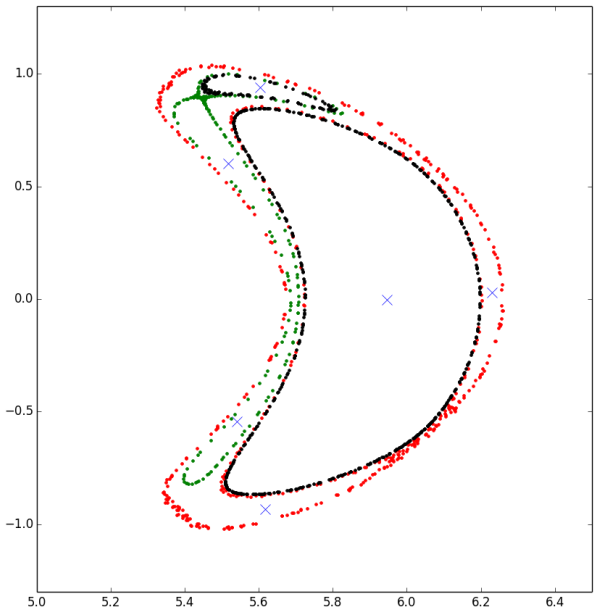

Figure 8.7: *Areas of interest located by the island finder program. Black (inner part): last closed flux surface. Red: island wrapping surface. Black: island. Green: first surface outside island. Blue crosses: Plasma axis, center of the five islands.*

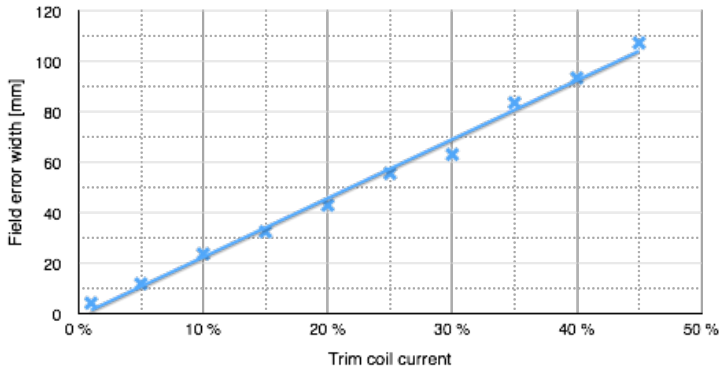

Figure 8.8: *Width of error region vs trim coil currents. The error region in question lies between the center of the island on the top left and the plasma axis. The error region width is defined as distance between the last closed flux surface and the last closed island flux surface. Trim coil current:* $I_{Ti} = c \cdot 0.0468 \cdot cos(2 \cdot \pi \cdot i/5)$*, where c is the range [0,1] and represents the % of max trim coil current.*

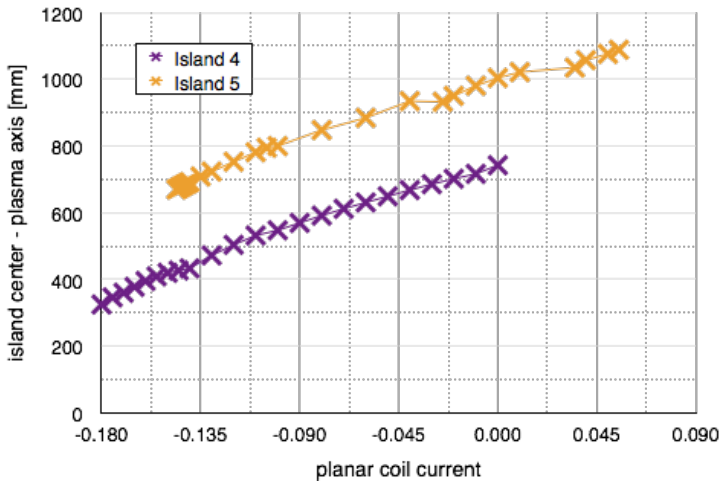

Figure 8.9: *Distance of island center to plasma axis.*

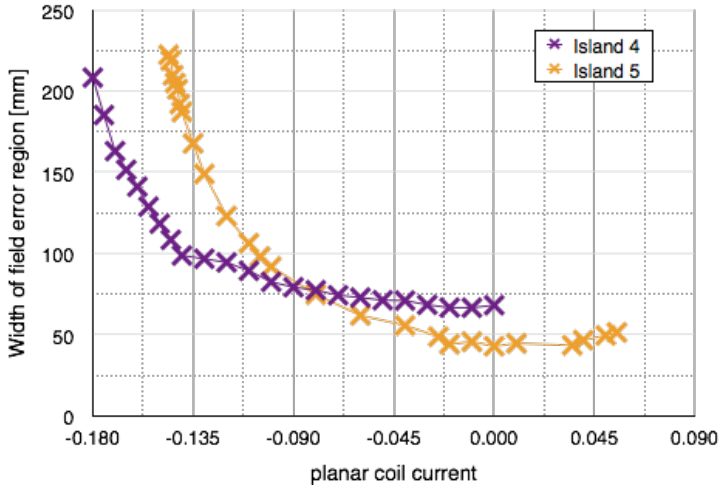

Figure 8.10: *Width of error region vs iota.*

increased for the measurement so that the islands are located further inward. This can be done using the planar coils. The radial movement of the islands using the planar coils is shown in figure 8.9. The distance from the island center to the plasma axis change is more or less a linear function of the planar coil current.

This raises the question whether it is more or less difficult to detect such a field error for a configuration with a slightly increased iota. Figure 8.10 shows the iota dependency of the error region. The error width increases exponentially for a higher iota. Therefore, error detection is easier at higher iota.

When increasing the iota further, the old error field region will become the new plasma axis, as shown in figure 8.11.

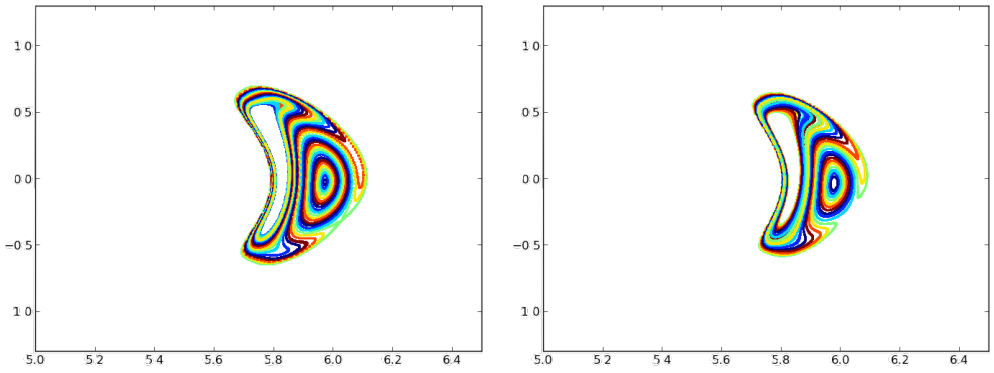

(a) -0.16

(b) -0.17

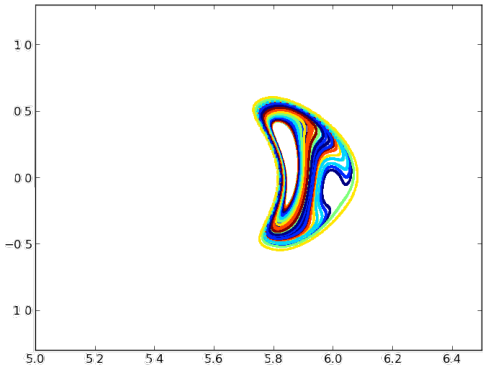

(c) -0.18

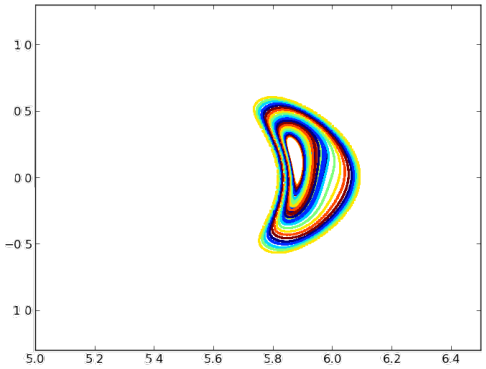

(d) -0.19

Figure 8.11: *Behavior of the error field region for islands near the plasma axis. Error field produced by the trim coils. Modular coils:* $I_{1-5} = 1.0$*, Sweep coils: zero. (a)* $I_{A,B} = -0.16$*, (b)* $I_{A,B} = -0.17$*, (c)* $I_{A,B} = -0.18$*, (d)* $I_{A,B} = -0.19$*.*

8.3 Conclusion regarding the limiter phase

From the set of reviewed options the inboard limiter shows the best results. This was then also the selected solution for the OP1.1 limiter phase [42], [43].

9 Conclusion

The effect of the SE was analyzed using the 3D SOL simulation code EMC3-Eirene (chapter 5). This was the first EMC3-Eirene calculation for the SE and one of the first EMC3 calculations using an equilibrium magnetic field. The main results are:

First, the investigation was able to confirm the protective capability of the SE. As mentioned, this study is the first fluid model approach used for the SE. That the SE will protect the pumping gap is its main requirement, so this validation is very positive.

Second, it turned out that the SE strongly affects the pumping efficiency. This is caused by the different locations for creation neutral particles. The reduction is $\sim$50 % in the transit phase. This reduction is very high but this phase will only last for several tens of seconds. Of more importance is the reduction at the final stage, because this will last for the rest of the discharge. In this final stage, the reduction is still $\sim$30 %, which is a lot considering that the SE is not even needed in this phase. This means that after reaching the final toroidal current, there is a loss of 1/3 of the pumping efficiency for the whole length of the discharge without any benefit. The pumping efficiency reduction raises the question of whether the SE is the best possible solution to protect the pumping gap.

First, the decision was made that the SE should be tested with a prototype before building a set of ten fully cooled HHF-SEs. This prototype test will take place in OP1.2b with an uncooled SE.

Unfortunately, the SE-RS is not accessible in the first operation phase, due to decreased discharge length, plasma density and heating power.

Therefore, specific SE testing configurations are necessary. In chapter 6, a method was developed which is able to mimic SE-RS even in OP1.2. This will enable early testing of the effect of an SE on the plasma performance. The mimic configurations are able to reproduce the heat load distribution to the components with a remarkably good accuracy; a sufficient agreement of the strike line patterns, in particular the patterns on the SE. This will allow performance of the desired TDU-SE tests even in OP1.2 with high confidence. In addition, these mimic configurations make it possible to test

alternatives for the SE in this early operation phase.

Some ideas for an alternative protection concept to the SE were presented in chapter 7. Of these, dynamically adjusting the magnetic field seems to be the most promising. With this approach, there are different option for keeping the plasma on a safe "path". The most promising options is the plasma shift approach. With this procedure, it could be possible to enable a safe start-up (even with the SE-RS configuration) without any new installation requirements. The required current ramp is within operational limits and it is not necessary to slow down the configuration evolution.

The fourth and last topic was the support of the first plasma phase. In this chapter different limiter and divertor configurations were tested with the goal to enable an early plasma phase. The final setup used with an inboard limiter at $\phi = 0$ was firstly analyzed here. These inboard limiter is now already installed in W7-X. In addition this work was able to show that it will be possible to detect a 1/1 field error with a already installed limiter or even with a installed divertor.

As all answers bear new questions, the results of this work also point to new areas of investigation. For the OP1.2 mimic configurations, the next steps should be VMEC/EXTENDER studies to estimate the β-effect and an estimate of the I_{BC} of these configurations (both effects will be small but nevertheless helpful). The results could be used to determine the number of configurations needed to mimic the whole range of the SE-RS evolution. In addition, EMC3-Eirene calculations will be necessary for comparison to the experimental results. Moreover, the testing of the mimic configurations in W7-X will improve the knowledge on which a final decision with respect to the HHF-SE will have to be based on.

Finally, the alternative options to the SE deserve additional attention. The control of the horizontal plasma position should be extended with VMEC/EXTENDER calculations in order to understand the implications of using MHD-equilibrium fields; the potential problems have been discussed in 7.1.4. The method to use a slower plasma evolution needs to be investigated further to explore its feasibility and identify critical issues. This will also require VMEC/EXTENDER calculations and possible transport simulations of the core plasma to test how the bootstrap current responds when using external coils for magnetic configuration adjustments.

List of acronyms

SE Scraper Element

TDU-SE Test Divertor Unit Scraper Element

HHF-DU High Heat Flux Divertor Unit

HHF-SE High Heat Flux Scraper Element

SE-RS Scraper Element Reference Scenario

TDU Test Divertor Unit

I_{BC} Bootstrap current

VRC Vacuum Reference Configuration

Bibliography

[1] Lyman Spitzer Jr. The stellarator concept. *Physics of Fluids (1958-1988)*, 1(4):253–264, 1958.

[2] A Peacock, J Kisslinger, J Boscary, J Geiger, F Hurd, R Koenig, M Krychowiak, R Stadler, M Smirnow, J Tretter, et al. A proposed scraper element to protect the end of the w7-x divertor target elements. In *Fusion Engineering (SOFE), 2011 IEEE/NPSS 24th Symposium on*, pages 1–5. IEEE, 2011.

[3] G Grieger and I Milch. Das fusionsexperiment wendelstein 7-x. *Physikalische Blätter*, 49(11):1001–1005, 1993.

[4] Hans-Stephan Bosch. Wendelstein 7-x, overview and status of construction. In *21st IEEE/NPS Symposium on Fusion Engineering SOFE 05*, 2005.

[5] RL Dewar and SR Hudson. Stellarator symmetry. *Physica D: Nonlinear Phenomena*, 112(1):275–280, 1998.

[6] R Heller. Superconductor for the coils of the modular stellarator wendelstein 7-x. *Magnetics, IEEE Transactions on*, 30(4):2383–2386, 1994.

[7] J Nührenberg, W Lotz, P Merkel, C Nührenberg, U Schwenn, E Strumberger, and T Hayashi. Overview on wendelstein 7-x theory. *Fusion Technology*, 27(CONF-941182–), 1995.

[8] Tamara Andreeva. Vacuum magnetic configurations of wendelstein 7-x. Technical report, Max-Planck-Institut fuer Plasmaphysik, Garching (Germany), 2002.

[9] *Transport-Simulationen für Wendelstein 7-X*, 2010. Forschungsbericht 2010 - Max-Planck-Institut fr Plasmaphysik, Teilinstitut Greifswald.

[10] Hermann Renner, Devendra Sharma, Johann Kisslinger, Jean Boscary, Heinz Grote, and Ralf Schneider. Physical aspects and design of the wendelstein 7-x divertor. *Fusion science and technology*, 46(2):318–326, 2004.

[11] R Brakel, M Köppen, A Peacock, A Werner, and M Jakubowsk. Specification of design loads for in-vessel components of w7-x. Technical report.

[12] J Boscary, A Peacock, T Friedrich, H Greuner, B Böswirth, H Tittes, W Schulmeyer, and F Hurd. Design improvement of the target elements of wendelstein 7-x divertor. *Fusion Engineering and Design*, 87(7):1453–1456, 2012.

[13] R. Wolf, 2015. Presentation at IPP-Programmtage (Greifswald).

[14] W3C-World Wide Web Consortium et al. Web services architecture, w3c working group. Technical report, Note 11, February, 2004.

[15] Peter C Stangeby et al. *The plasma boundary of magnetic fusion devices*, volume 224. Institute of Physics Publishing Bristol, 2000.

[16] *3-dimensionale Plasmarandschicht-Simulationen in unvollständig ergodisierten Magnetfeldern*, 2008. Heinrich-Heine-Universitäet Düesseldorf.

[17] J. Geiger. Private communications.

[18] Steven P Hirshman and JC Whitson. Steepest-descent moment method for three-dimensional magnetohydrodynamic equilibria. *Physics of Fluids (1958-1988)*, 26(12):3553–3568, 1983.

[19] SP Hirshman, P Merkel, et al. Three-dimensional free boundary calculations using a spectral green's function method. *Computer Physics Communications*, 43(1):143–155, 1986.

[20] Michael Drevlak, D Monticello, and A Reiman. Pies free boundary stellarator equilibria with improved initial conditions. *Nuclear fusion*, 45(7):731, 2005.

[21] J.A. Bittencourt. *Fundamentals of Plasma Physics*. Springer, 2004. ISBN 0 387 2097 1.

[22] VD Shafranov. Equilibrium of a toroidal pinch in a magnetic field. *Soviet Atomic Energy*, 13(6):1149–1158, 1963.

[23] J. Geiger, 2015. Private communication.

[24] J. Geiger, 2013. Private communication.

[25] J Geiger, CD Beidler, M Drevlak, H Maassberg, C Nührenberg, Y Suzuki, and Yu Turkin. Effects of net currents on the magnetic configuration of w7-x. *Contributions to Plasma Physics*, 50(8):770–774, 2010.

[26] Jeremy D Lore, Tamara Andreeva, Jean Boscary, Sergey Bozhenkov, Joachim Geiger, Jeffrey H Harris, Hauke Hoelbe, Arnold Lumsdaine, Dean McGinnis, Andrew Peacock, et al. Design and analysis of divertor scraper elements for the w7-x stellarator. *Plasma Science, IEEE Transactions on*, 42(3):539–544, 2014.

[27] Arnold Lumsdaine, Jean Boscary, Eppie Clark, Kivanc Ekici, Jeffrey Harris, Dean McGinnis, Jeremy D Lore, Andrew Peacock, Joseph Tipton, and Jörg Tretter. Modeling and analysis of the w7-x high heat-flux divertor scraper element. *Plasma Science, IEEE Transactions on*, 42(3):545–551, 2014.

[28] Y Feng, F Sardei, and J Kisslinger. 3d fluid modelling of the edge plasma by means of a monte carlo technique. *Journal of nuclear materials*, 266:812–818, 1999.

[29] Yühe Feng, F Sardei, J Kisslinger, and P Grigull. A 3d monte carlo code for plasma transport in island divertors. *Journal of nuclear materials*, 241:930–934, 1997.

[30] J Lore, T Andreeva, J Boscary, JM Canik, J Geiger, Jeffrey H Harris, Arnold Lumsdaine, D McGinnis, A Peacock, and J Tipton. Heat flux and design calculations for the w7-x divertor scraper element. In *Proceedings of the 24th International Atomic Energy Agency Fusion Energy Conference*, 2012.

[31] Arnold Lumsdaine, Jean Boscary, Joris Fellinger, Jeff Harris, Hauke Hölbe, Ralf König, Jeremy Lore, Dean McGinnis, Hutch Neilson, Peter Titus, et al. Design of the wendelstein 7-x inertially cooled test divertor unit scraper element. *Fusion Engineering and Design*, 2015.

[32] *Access to long-pulse relevant edge scenarios in Wendelstein 7-X in its early phases of operation*, 2015. Submitted to Nuclear Fusion.

[33] *Physics in the configuration space of W7-X*, 2015. Plasma Phys. Control. Fusion 57 014004.

[34] Per Helander. Theory of plasma confinement in non-axisymmetric magnetic fields. *Reports on Progress in Physics*, 77(8):087001, 2014.

[35] J Geiger, CD Beidler, M Drevlak, H Maassberg, C Nührenberg, Y Suzuki, and Yu Turkin. Effects of net currents on the magnetic configuration of w7-x. *Contributions to Plasma Physics*, 50(8):770–774, 2010.

[36] E Strumberger. Finite-β magnetic field line tracing for helias configurations. *Nuclear Fusion*, 37(1):19, 1997.

[37] H Renner, J Boscary, H Greuner, H Grote, FW Hoffmann, J Kisslinger, E Strumberger, and B Mendelevitch. Divertor concept for the w7-x stellarator and mode of operation. *Plasma physics and controlled fusion*, 44(6):1005, 2002.

[38] SA Bozhenkov, J Geiger, M Grahl, J Kißlinger, A Werner, and RC Wolf. Service oriented architecture for scientific analysis at w7-x. an example of a field line tracer. *Fusion Engineering and Design*, 88(11):2997–3006, 2013.

[39] J. Fellinger T. Rummel. Private communication, 2013.

[40] *Magnetic flux densities at coil surfaces due to individual influences from coil groups*, 2014. IPP doc: 1-GXA10E-T0007_0.doc.

[41] H-S Bosch, Rudolf Brakel, Maurizio Gasparotto, Heinz Grote, D Hartmann, Rene Herrmann, Michael Nagel, Dirk Naujoks, Matthias Otte, Konrad Risse, et al. Transition from construction to operation phase of the wendelstein 7-x stellarator. In *25th Symposium on Fusion Engineering (SOFE 2013)*, pages 432–438. IEEE, 2014.

[42] Thomas Sunn Pedersen. Plans for first plasma operation on wendelstein 7-x. *Bulletin of the American Physical Society*, 59, 2014.

[43] SA Bozhenkov, F Effenberg, Y Feng, J Geiger, DA Hartmann, H Hölbe, TS Pedersen, and RC Wolf. Limiter for the early operation phase of w7-x. In *41st EPS Conference on Plasma Physics*, 2014.

List of Figures

Acknowledgments

This work was not possible without the help of many other people.

My biggest thanks go to Thomas Sunn Pedersen, he is the best doctoral advisor imaginable. He enabled me to contribute to such an interesting topic, gave me all the scientific freedom I needed and supported me always with constructive, positive and ever helpful feedback.

Joachim Geiger I like to thank for contributing to this work with extensive equilibrium calculations (VMEC/EXTENDER). I especially want to thank him for reading my thesis during his holidays. Also, I like to thank for many interesting conversations about the magnetic field structure of W7-X, its history and alternatives to the SE.

Many thanks go to Yühe Feng for explaining me the characteristics of the W7-X divertor geometry and for his instructions of how to use his EMC3 code.

Sergey Bozhenkov I like to thank for explaining me the IPP-Web-services and in particular how to perform a field line diffusion with these computer codes.

The SE-working group I like to thank for helpful discussions and regular meetings concerning updates on the calculations and the SE design. In this connection, I like to thank Joris Fellinger for leading the collaboration group. His direct approach often helped to save a lot of time.

Matthias Köppen I like to thank for his calculations on the limits of the current ramp rate of the superconducting coils. His work was very helpful for me.

Jörg Tretter I like to thank for his explanations of how to use the CAD program CATIA and his work for designing divertor parts in order to find the optimal strategy for OP1.1.

Kathrin Konrad and Eve Stenson I like to thank for helping me with the English grammar and spelling.

At last, I want say “thank you” to the whole W7-X Team for the opportunity to take part in such a wonderful experiment.